

Integration of Nanostructures and Quantum Dots into Spherical Silicon Solar Cells

By

Behzad Esfandiarpour

A thesis
presented to the University of Waterloo
in fulfillment of the
thesis requirement for the degree of
Doctor of Philosophy
in
Electrical and Computer Engineering

Waterloo, Ontario, Canada, 2013

© Behzad Esfandiarpour 2013

Author's Declaration

I hereby declare that I am the sole author of this thesis. This is a true copy of the thesis, including any required final revisions, as accepted by my examiners.

I understand that my thesis may be made electronically available to the public.

Abstract

In order to improve the optical losses of spherical silicon solar cells, new fabrication designs were presented. The new device structures are fabricated based on integration of nanostructures into spherical silicon solar cells. These new device structures include: spherical silicon solar cells integrated with nanostructured antireflection coating layers, spherical silicon solar cells with hemispherical nanopit texturing, and cells integrated with colloidal quantum dots.

Silicon spheres were characterized by means of transmission electron microscopy (TEM), single-crystal x-ray diffraction and x-ray powder diffraction to establish the crystallinity nature of the silicon spheres. Furthermore, the material properties of silicon spheres including surface morphology, microwave photoconductivity decay lifetime, and impurity elemental distributions were studied.

Silicon nitride antireflection coating layers were developed and deposited onto the spherical silicon solar cells, using a PECVD system. A low temperature hydrogenation plasma technique was developed to improve the passivation quality of the spherical silicon solar cells. The spectral response of silicon spheres with and without a silicon nitride antireflection coating was studied.

We have successfully developed and integrated a nanostructured antireflection coating layer into spherical silicon solar cells. The nanostructured porous layer consists of graded-size silicon nanocrystals and quantum-size Si nanoparticles embedded in an oxide matrix. This layer has been characterized by means of scanning electron microscopy (SEM), transmission electron microscopy (TEM), Scanning tunneling TEM, energy filtered TEM, transmission electron diffraction (TED), electron energy loss spectroscopy (EELS), energy dispersive x-ray (EDX), Raman spectroscopy and photoluminescence spectroscopy (PL).

We developed a novel technique of electrochemical etching for silicon surface texturing using a liquid-phase deposition of oxide mask. Using a focus ion-beam (FIB) technique, cross-sectional TEM samples were prepared to investigate the nature of texturing and the composition of the deposited mask. The hemispherical nanopit texturing was successfully integrated into spherical silicon solar cells and the etching mechanisms and the chemical reactions were discussed.

CdSe colloidal quantum dots with diameter of about 2.8nm were integrated into a graded-density nanoporous layer. This structure was implemented on the emitter of the spherical silicon solar cells and the spectral response with and without incorporation of QDs was studied.

Acknowledgments

I am truly grateful:

To my supervisor, Professor Siva Sivoththaman, for constant guidance and excellent academic and scientific support throughout my PhD studies.

To all my PhD defense committee members, Professor Raafat R. Mansour, Professor Dayan Ban, and Professor Eric Prouzet, for their time and effort to improve the quality of this thesis.

To my external examiner, Professor Ray LaPierre, for reviewing my thesis and providing valuable comments and suggestions.

To the CAPDS lab manager, Mr. Joseph Street, for his valuable technical assistance and sharing his knowledgeable advice. Also, I would like to thank Mr. Richard Barber and Mr. Bill Jolley, G2N and CIRFE lab managers, for their precious cooperation and useful discussions.

To my wonderful colleagues in CAPDS group who have always supported me and been there to lend me a hand during rough days of my PhD study.

To all my friends in Waterloo who made my PhD enjoyable experience and full of unforgettable memories.

I have the utmost gratitude and appreciation for my parents who unconditionally love me and patiently guide me. I will never be able to return that or to be thankful enough for their sacrifices.

Table of Contents

| | |
|---|----------|
| Chapter 1..... | 1 |
| 1.1 Introduction..... | 1 |
| 1.2 Solar energy | 1 |
| 1.3 Motivation of this research..... | 2 |
| 1.4 Objectives of this research..... | 4 |
| 1.5 Thesis outline..... | 5 |
| Chapter 2 Literature Survey..... | 7 |
| 2.1 Spherical solar cell technology..... | 8 |
| 2.1.1 Dropping method..... | 8 |
| 2.1.2 Spheroidization by surface tension..... | 9 |
| 2.1.3 Fabrication process of spherical silicon solar cells..... | 11 |
| 2.2 Porous Si (on silicon wafers)..... | 12 |
| 2.2.1 Electrochemical etching of silicon wafers..... | 12 |
| 2.2.1.1 Current-voltage characteristics..... | 13 |
| 2.2.1.2 Silicon dissolution chemistry..... | 15 |
| 2.2.1.3 Formation of macropores..... | 17 |
| 2.2.1.4 Morphology of porous silicon: effect of etching parameters..... | 18 |
| 2.2.1.5 Pore Orientation..... | 21 |
| 2.2.2 Stain etching of silicon..... | 22 |
| 2.2.3 Metal-assisted etching of silicon..... | 23 |
| 2.2.4 Visible luminescence from porous silicon..... | 24 |
| 2.2.5 Porous Si in solar cells: PS as an AR coating..... | 25 |
| 2.3 Semiconductor quantum dots..... | 27 |
| 2.3.1 Quantum confinement effect..... | 28 |
| 2.3.2 Solution-processed quantum dots..... | 29 |
| 2.3.3 Application of QDs in solar cells..... | 29 |
| 2.3.3.1 Down-shifting layer..... | 29 |
| 2.3.3.2 QDs-sensitized solar cells..... | 30 |

| | |
|---|-----------|
| Chapter 3 Experimental results of material properties and characterization studies of silicon spheres..... | 31 |
| 3.1 Introduction..... | 31 |
| 3.2 Scanning electron microscopy study..... | 32 |
| 3.3 Investigation of the crystallinity of silicon spheres by X-ray diffraction..... | 34 |
| 3.3.1 X-ray powder diffraction..... | 34 |
| 3.3.2 Single-crystal x-ray diffraction..... | 36 |
| 3.4 Transmission electron microscopy study of silicon spheres..... | 40 |
| 3.5 Secondary ion mass spectroscopy imaging of elemental distribution in the bulk of silicon spheres..... | 41 |
| 3.6 Minority carrier lifetime in silicon spheres..... | 44 |
| 3.7 Conclusion..... | 45 |
| Chapter 4 Baseline fabrication process and fabrication of new designs with integration of nanostructures into silicon spheres..... | 46 |
| 4.1 Introduction..... | 46 |
| 4.1 Baseline fabrication process..... | 47 |
| 4.2 Development of SiN _x passivation/ARC layers for silicon spheres (chapter 5)..... | 49 |
| 4.3 Integration of a graded-density nanoporous Si layer with quantum-size Si nanoparticles (Chapter 6)..... | 49 |
| 4.4 Integration of hemispherical nanopit texturing into silicon spheres (Chapter 7)..... | 51 |
| 4.4 Integration of colloidal CdSe-QDs into silicon spheres (Chapter 8)..... | 52 |
| Chapter 5 Development of SiN_x passivation/ARC layers for spherical solar cells..... | 53 |
| 5.1 Introduction..... | 53 |
| 5.2 Experimental results..... | 54 |
| 5.3 Development of a hydrogenation plasma process to improve the surface passivation quality..... | 55 |
| 5.4 Reflectance and spectral response of spherical solar cells with SiN _x ARC layer..... | 57 |
| 5.5 Conclusion..... | 59 |

| | |
|---|------------|
| Chapter 6 Integration of a graded-density nanoporous Si layer with quantum-size Si nanoparticles..... | 60 |
| 6.1 Introduction..... | 60 |
| 6.2 Experimental details..... | 61 |
| 6.3 Scanning electron microscopy: Surface morphology of the graded-density n-PS layer..... | 62 |
| 6.4 Cross-sectional TEM study of graded-density n-PS layer..... | 64 |
| 6.5 EDX and EELS line scan analyses: linear graded-density PS..... | 73 |
| 6.6 EELS investigation of Si quantum dots embedded in nanoporous oxide: stability properties of oxide matrix..... | 78 |
| 6.7 Energy filtered TEM study of Si nanocrystals in n-PS layer..... | 79 |
| 6.8 Raman spectroscopy..... | 79 |
| 6.9 Luminescence properties of graded-density nanoporous..... | 81 |
| 6.10 Light trapping and external quantum efficiency of spherical silicon solar cells..... | 83 |
| 6.11 Conclusion..... | 87 |
| Chapter 7 Hemispherical nanopit silicon texturing: a novel method of texturing based on etching through a liquid-phase deposited mask..... | 88 |
| 7.1 Introduction..... | 88 |
| 7.2 Surface morphology of nanotextured silicon spheres and elemental study of LPD mask..... | 89 |
| 7.3 Transmission electron microscopy study..... | 94 |
| 7.4 Etching mechanism and chemical reactions..... | 100 |
| 7.5 Reflectance characteristics and external quantum efficiency of silicon spheres with hemispherical nanopit texturing..... | 101 |
| 7.6 Conclusion..... | 103 |
| Chapter 8 Integration of colloidal quantum dots into spherical silicon solar cells..... | 104 |
| 8.1 Introduction..... | 104 |

| | |
|--|------------|
| 8.2 Characterization of colloidal QDs and deposition of closed-packed QDs monolayer encapsulated by metal oxide layers | 105 |
| 8.3 External quantum efficiency of spherical silicon solar cells integrated with colloidal CdSe-QDs..... | 110 |
| 8.4 Conclusion..... | 112 |
| Chapter 9 Conclusion..... | 113 |
| Conclusion..... | 113 |
| References..... | 116 |

Chapter 1

1.1 Introduction

Among renewable energy resources, photovoltaics (PV) are an attractive technology since it can directly convert solar energy into electrical energy without involving any moving parts such as a turbine. As a long-term, environment-friendly, and reliable energy source, solar photovoltaic is a promising technology for the future. According to Photovoltaic Technology Status and Prospects Canadian Annual Report (2006), growth in the Canadian sector has been more than 20% annually between 1993 and 2006. However, with a price of about 20 cents/kWh, photovoltaic power is still an expensive source of energy. Therefore, cost reduction and conversion efficiency improvement through technological advances is required to make PV a major energy source.

1.2 Solar energy

Crystalline Si solar cells have remained a dominant technology in the photovoltaic (PV) industry due to their high reliability and high conversion efficiency.^{1,2} Although the single-crystal cells offer high efficiencies, due to the high cost of solar-grade Si wafers, cost reduction through technological advances is required to make PV a major energy source. During past decades, various alternatives such as thin film solar cells,³⁻⁵ organic PV devices,⁶ solar cells based on nanostructured material⁷⁻¹⁰, etc., have been widely considered to develop less expensive

technologies. Thin film technologies mainly amorphous silicon (a-Si), cadmium telluride (CdTe) and copper indium gallium selenide (CIS/CIGS) have been industrialized and are produced by many companies. These technologies, as compared to crystalline silicon, require less expensive material and fewer steps to fabricate. However, the main drawback is lower efficiency and lack of stability. Organic solar cells can be processed from solution and have shown conversion efficiency improvement in recent years (close to 9%). However, due to the lack of stability, they are still far from PV market.

In spite of all attempts to increase the conversion efficiency and to decrease the production cost of solar cells, the price per watt of solar energy is still several times higher than the electricity produced by other resources such as natural gas, oil, hydroelectric, coal, and nuclear.

1.3 Motivation of this research

The spherical Si solar cell is relatively new technology based on crystalline silicon spheres with a diameter of about 1mm. This technology has been a research goal due to the low-cost fabrication process, high performance, and mechanical flexibility when embedded into flexible aluminum foils.¹¹⁻¹⁴ In this technology, small single-crystal Si spheres with different qualities from metallurgical to semiconductor grade are produced by the melting and recrystallization of Si feedstock. Therefore, silicon spheres can be obtained directly from molten Si without a cutting or polishing process, which makes them a promising candidate for low-cost PV modules. Furthermore, Si spheres can be embedded in transparent substrates to manufacture semi-transparent silicon solar cells.

Optimization of the optical losses of spherical silicon solar cells is one of the most important techniques for improving the short-circuit current density and hence the efficiency of these cells. However, due to the shape of the silicon spheres embedded in aluminum foil, conventional deposition methods cannot easily be applied to make a uniform antireflection coating (ARC) layer on spherical silicon solar cells. Furthermore, texturing of silicon spheres embedded in aluminum foil is not feasible using established texturing methods.

Nanoporous Si layers have been successfully used as an effective anti-reflecting coating in crystalline silicon solar cells. Furthermore, nanoporous layers can be fabricated by an electrochemical etching process and can be uniformly coated over the silicon spheres. We could

successfully develop and integrate a nanoporous layer into spherical silicon solar cells. This layer in initial studies showed incredible properties such as significantly high luminescence and suppression of reflectivity at a wide range of spectral response. By development of this layer, a nanostructured porous layer consisting of graded-size silicon nanocrystals and quantum-size Si nanoparticles were obtained. The graded-size structure explains the suppression of reflectivity at wide range of spectral response (black silicon) and quantum-size silicon nanoparticles with dimensions less than 2nm justify the significantly high luminescence. This layer, due to the quantum confinement effects, shows incredible properties such as enhanced luminescence, light trapping, photon shifting and band-gap opening. Band-gap opening in the emitter structure minimizes the absorption of photons in the dead layer and improves the short circuit current. This layer has been extensively characterized and the solar cell characteristics, integrated with this nanostructured anti-reflecting coating, were studied.

In a different design, we also pursue the nanotexturing of sphere silicon solar cell. Texturing is a basic and a fundamental step in the fabrication of silicon solar cells which improves the light trapping and hence the short circuit current. However, conventional texturing methods cannot be applied to silicon spheres. We have developed a hemispherical nanopit texturing based on electrochemical etching of silicon spheres in a solution of hydrofluorosilicic acid (H_2SiF_6). Since H_2SiF_6 is a byproduct of etching of silicon in hydrofluoric acid (HF), this solution is normally not used for etching of silicon. However, using electrochemical etching without any lithography step, a uniform surface nanotexturing with etch pits of about 300-700nm depth is performed. This novel method of texturing was extensively studied and the characteristics of spherical silicon solar cells textured by this method were investigated.

Next generation photovoltaic technology based on quantum dots and concepts such as down-conversion and down-shifting is promising a significant increase in the conversion efficiency of solar cells. Therefore, investigation and development of methods for the integration of quantum dots (QDs) to silicon solar cells may lead to photovoltaic devices which can harvest the solar energy more efficiently. We have studied different methods of arrangement, assembly and integration of QDs into spherical silicon solar cells. We successfully fabricated a QDs-embedded layer by processing colloidal QDs into a graded-density nanoporous silicon layer. This structure is implemented on top of the emitter of spherical silicon solar cells and the spectral response with and without QDs incorporation was studied. However, the promising efficiency improvement

that the theory of quantum dots predicted was not observed but absorption of optically active quantum dots, along with the enhancement of high-energy photons conversion efficiency was observed.

1.4 Objectives of this research

- Characterization of silicon spheres to establish the crystallinity nature of silicon spheres. Furthermore, material properties of silicon spheres including surface morphology, microwave photoconductivity decay lifetime, and impurity elemental distributions will be studied.
- Development of silicon nitride layers using PECVD technique, to improve passivation/ARC layers for silicon spheres.
- Process development to fabricate spherical silicon solar cells with selective emitter structure. The depth of junction in spherical silicon solar cells is higher than conventional solar cells which are fabricated on flat silicon wafers. In order to reduce the shunt problem across the p-n junction where aluminum foil is thermally bonded to the silicon spheres, the depth of junction is kept above 0.7 μ m.
- Integration of nanostructured antireflection coating layers to suppress the reflection in a wide range of spectral response.
- Integration of QD-embedded thin films into spherical silicon solar cells with high luminescence in the range of optimum quantum efficiency of the device.
- Development of novel nanotexturing techniques that can be applied as a post-process method to spherical silicon solar cells. Texturing of silicon spheres embedded in aluminum foil is not feasible using established texturing methods.
- To study and develop different methods of processing and embedment of semiconductor QDs
- Integration of the CdSe colloidal QDs into silicon spheres and study of the effect of CdSe QDs on the spectral response of spherical silicon solar cells.

1.5 Thesis outline

The following chapters of this thesis are dedicated to brief literature review (Chapter 2), experimental results of material characterization of silicon spheres (Chapter 3), baseline fabrication process and fabrication of new designs (Chapter 4), development of SiN_x passivation/ARC layers for spherical silicon solar cells (chapter 5). The new device structures are fabricated based on integration of nanostructured layers into spherical silicon solar cells. Spherical silicon solar cells integrated with nanostructured antireflection coating layers are investigated in Chapter 6. Hemispherical nano-pit texturing structure and integration of colloidal QDs into spherical silicon solar cells will be discussed in Chapter 7 and Chapter 8, respectively.

In Chapter 2 (literature review), the methods of formation of silicon spheres are reviewed and the fabrication process of spherical solar cells is explained. Furthermore, the advantages of Spherical silicon technology, as compared to other technologies are discussed. Since the developed nanostructured layers and nanotexturing are based on electrochemical etching techniques, the electrochemical etching of silicon and formation of nanoporous silicon has been reviewed. However, there is no previous study of porous silicon on spherical silicon solar cells. Also, there is no literature review on the texturing of silicon in H₂SiF₆ solution. In this chapter we also briefly review the quantum confinement effects in semiconductor nanocrystals.

Chapter 3 discusses the experimental results of material properties and characterization studies performed on silicon spheres. The scanning electron microscopy was used to study the shape and surface morphology of the silicon spheres as well as surface defects. Crystallinity of silicon spheres was investigated by means of single-crystal x-ray diffraction (XRD), x-ray powder diffraction, and transmission electron microscopy. Elemental distribution on the polished surface of silicon spheres was studied using the secondary ion mass spectroscopy (SIMS) imaging technique. The microwave Photoconductivity decay technique was used to obtain the minority carrier recombination lifetime in silicon spheres.

Chapter 4 covers the baseline fabrication process of silicon spheres and fabrication of new designs. These new device structures include: spherical silicon solar cell integrated with nanostructured porous layer, sphere silicon solar cells with hemispherical nano-pit texturing, and cells integrated with colloidal quantum dots.

In Chapter 5, silicon nitride passivation/ARC layers are developed and deposited onto spherical silicon solar cells. Furthermore, a low temperature hydrogenation plasma technique was

developed to improve the passivation quality of spherical silicon solar cells. The cell characteristics were studied.

In Chapter 6, the result of characterization studies of graded-density nanoporous layer with Si-QDs embedded layer is presented. This layer has been characterized by the means of scanning electron microscopy (SEM), transmission electron microscopy (TEM), Scanning tunneling TEM, energy filtered TEM, dark-field TEM, transmission electron diffraction (TED), electron energy loss spectroscopy (EELS), energy dispersive x-ray (EDX), Raman spectroscopy and photoluminescence spectroscopy (PL). Furthermore, we have successfully integrated this layer into silicon spheres, and the solar cell characteristics were studied.

Chapter 7 covers the integration of hemispherical nanopit texturing to spherical silicon solar cells. The etching simultaneously occurs during liquid-phase deposition (LPD) of a mask on the surface of the silicon, without requiring any lithography process. Using a focus ion-beam (FIB) technique, cross-sectional TEM samples were prepared to investigate the nature of texturing and the composition of the deposited mask. The related chemical reactions responsible for LPD SiO_x deposition and electrochemical etching of silicon were studied. The cell characterizations including external quantum efficiency were presented.

In Chapter 8, we discuss different methods of processing and embedment of semiconductor QDs. These methods are mainly based on embedment of colloidal quantum dots in metal oxide layers. We also successfully fabricated a QDs-embedded layer by processing colloidal QDs into a graded-density nanoporous silicon layer. The spectral response measurements with and without QDs incorporation was studied.

The whole work is concluded in Chapter 9 of the thesis.

Chapter 2

Literature Survey

Among silicon solar cell technologies, spherical Si solar cells have been a research goal due to their low-cost fabrication process, high performance, and mechanical flexibility when embedded into flexible aluminum foils.¹¹⁻¹⁴ In this technology, small single-crystal Si spheres with different qualities from metallurgical to semiconductor grade are produced by melting and recrystallization of Si feedstock. Therefore, silicon spheres can be obtained directly from molten Si without a cutting or polishing process, which makes them a promising candidate for low-cost PV modules. Furthermore, Si spheres can be embedded in transparent substrates to manufacture semi-transparent silicon solar cells.

In this chapter the methods of formation of silicon spheres are reviewed and the fabrication process of spherical solar cells is discussed. Due to the shape of the silicon spheres and embedment of spheres in a perforated aluminum foil (non-planar), conventional methods cannot easily be applied in the fabrication process of silicon solar cells. For instance, texturing of silicon spheres and also deposition of a uniform ARC layer onto the spherical silicon solar cells are challenging steps. We have developed a novel method of texturing based on the electrochemical etching of silicon which has been applied to silicon spheres to create a uniform hemispherical

nanopit texturing. Also, for the first time, we have applied nano-porous Si layers to silicon spheres. Since these methods are based on the electrochemical etching of silicon, in this chapter we also review the electrochemical etching process including its application in solar cells.

In section 2.1, the formation methods of silicon spheres including dropping method and spheroidization by surface tension, are explained and the fabrication process of solar cells is discussed. In section 2.2, the electrochemical etching of silicon and formation of porous silicon reviewed. Alternative methods to produce porous Si are also discussed briefly.

In section 2.3, semiconductor QDs and their application in solar cells as a down-shifting layer are discussed.

2.1. Spherical solar cell technology

Compared to other methods such as FZ technology¹⁵, CZ technology¹⁶ or the cast silicon method, spherical silicon is relatively new technology. In ingot technologies, the silicon wafer is obtained through cutting and polishing processes which produce waste material. Although ingot technologies produce high quality silicon, due to the waste, further cost reduction is difficult. In this technology, silicon spheres can be produced in different sizes (1-2mm) directly from molten silicon at high speeds. Also, different silicon qualities, from metallurgical grade to solar grade, can be used as a source material.

2.1.1 Dropping method

In the dropping method¹⁷⁻²¹, p-type silicon is melted in a quartz boat and the molten silicon is instilled from the top of the tower. By traveling in an inert gas, the droplets are solidified into silicon spheres. The schematic in Fig. 2.1 shows the formation process of silicon spheres by the dropping method. Spheres obtained by this method are multicrystalline and they may contain defects and impurities, affecting solar cell efficiency. The correlation between the crystallinity of spheres and solar cell performance was studied by Omea et. al¹⁷. Hydrogen plasma treatment has been reported as an effective method to passivate the bulk defects and to improve the solar cell performance²².

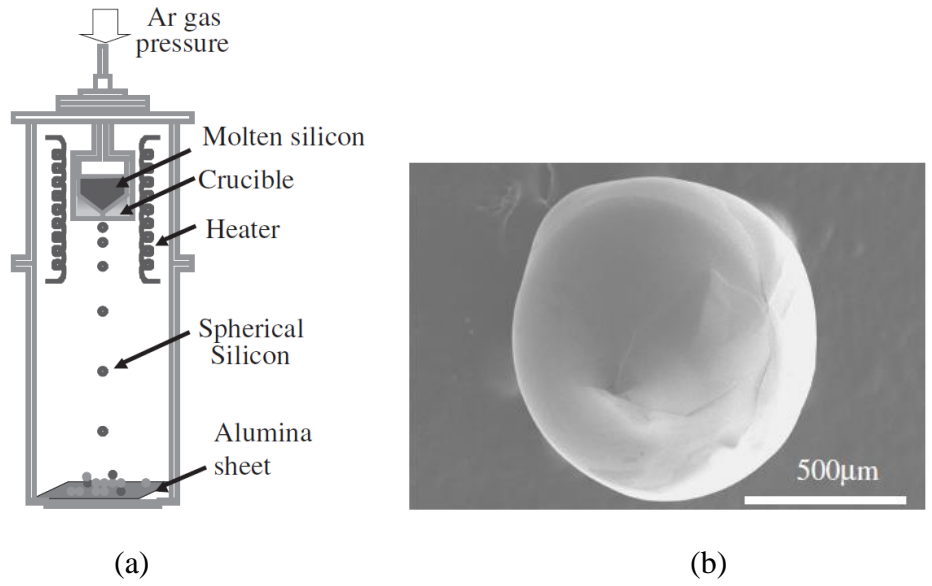


Figure 2.1: (a) Fabrication process of silicon spheres by dropping method. (b) SEM image of obtained silicon sphere.¹⁷

Fig. 2.2 shows the cell characteristics before and after hydrogen plasma treatment. Furthermore, other methods have been suggested to improve the crystalline quality of silicon spheres²³.

2.1.2 Spheroidization by surface tension

This technique invented and developed by Texas Instruments (TI), is based on spheroidization of molten silicon by surface tension²⁴⁻²⁷. In this technique, a very small amount of silicon powder is heated above the melting point and moved towards a lower temperature zone using a high power arc lamp. Due to the surface tension of molten silicon, the silicon powder agglomerates and turns into a spherical shape.

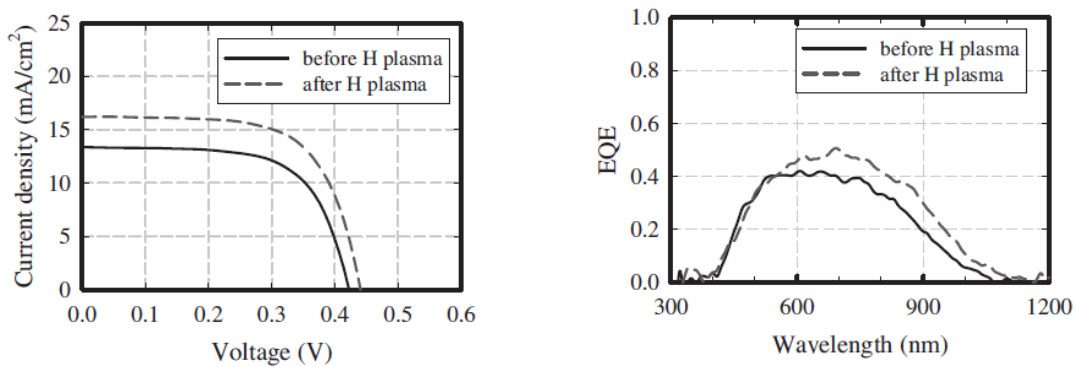


Figure 2.2: I-V characteristic and spectral response of spherical cells before and after hydrogen plasma treatment²².

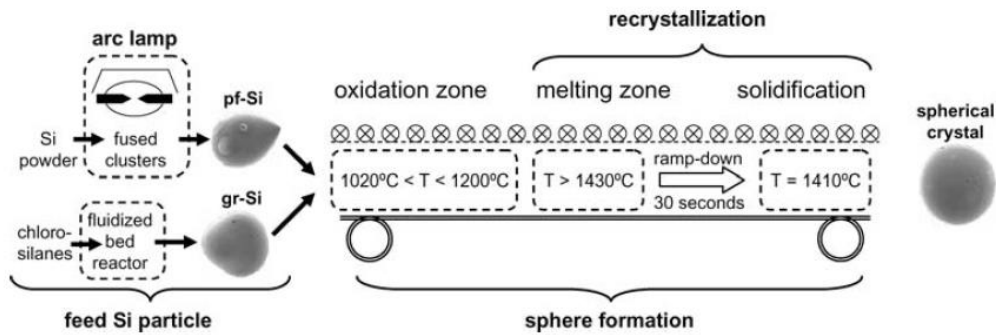


Figure 2.3: Schematic showing the melting and recrystallization steps to improve the crystalline quality and purity of silicon sphere. Gr-Si (granular silicon) is obtained from metallurgical grade silicon and pf-Si (piriform Si) is obtained from optically fused powder silicon.²⁸

Crystalline silicon spheres with a size of 1mm or smaller can be obtained by this method. The crystalline quality and purity of the spheres can be improved by sequential melting and recrystallization steps (Fig. 2.3). In this process, spheres (optically fused or granular beads) are covered with a layer of thermal oxide and during the melting step, due to the segregation between solid and liquid, impurities move towards the surface layer. This oxide layer is etched away by chemical etching and the process is repeated until the desired quality is obtained²⁹. Surface morphology of Silicon spheres after Dash etch (mixture of 1:3:10 hydrofluoric, nitric, and acetic acids) is shown in Fig. 2.4.

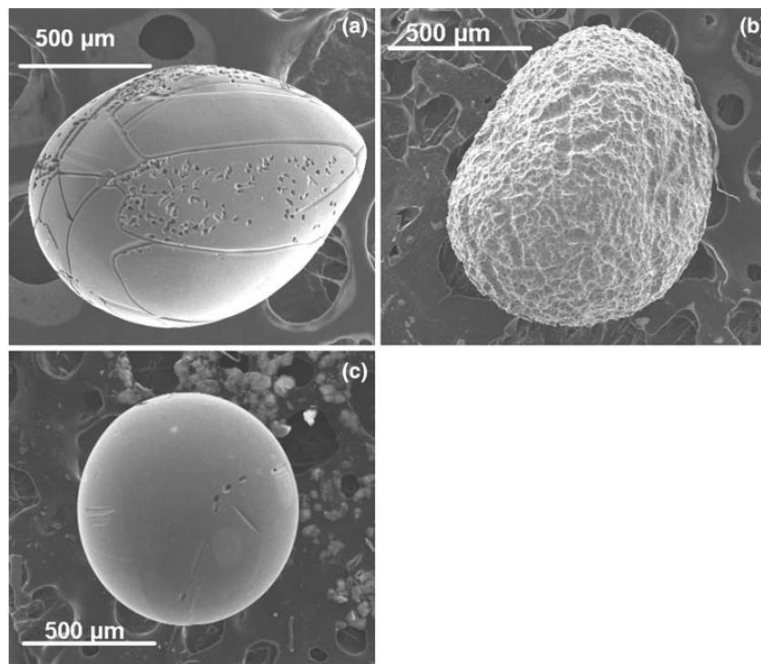


Figure 2.4: SEM images showing surface morphology of Silicon spheres after Dash etch of (a) piriform-Si sphere (optically fused clusters), (b) granular Si, and (c) recrystallized sphere.²⁸

2.1.3 Fabrication process of spherical silicon solar cells

Fig. 2.5 shows fabrication process steps of spherical silicon solar cells. This technique was developed by Texas Instruments with the trade mark of Spheral SolarTM. In this technology, Si spheres with diameter of about 1mm are embedded and thermally bonded into an aluminum foil. Each sphere is p-type in the bulk with n-type diffusion over the surface. The emitter is formed all over the sphere surface using a high temperature (above 900°C) diffusion step from an infinite phosphorus doping source. After junction formation, the silicon spheres are pressed on an aluminum (Al) foil and bonded by a thermo-mechanical process at a temperature around 500°C. Once this emitter (cathode) contact is formed, the n⁺ layer from the portion of the sphere below the Al-foil bonding is chemically etched away to expose the p-type bulk for base (anode) contact. In order to provide a contact to the p-type sphere, a thin layer of polyimide as an insulating layer has been deposited to separate the front and back foils. Subsequently, the polyamide layer is cured to a solid form and patterned to open a via to access p-Si. A front side thin (FST) process can be used to remove the heavily doped region. A selective dissolution (SED) process was used to form an insulator layer on shunted spheres. The SED process anodizes the shunted or shorted spheres to isolate them from the circuit. This process doesn't affect the other spheres. Finally, back aluminum foil is bonded to the spheres and an anti-reflection coating of TiO₂ is deposited.

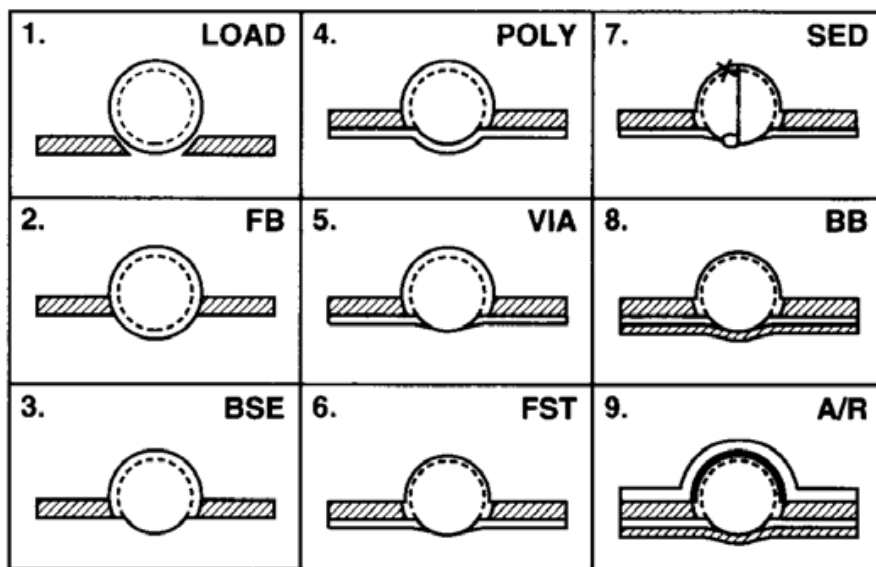


Figure 2:5. Fabrication process of spherical silicon solar cells³⁰

2.2 Porous Si (on silicon wafers)

Since the efficient luminescence of porous silicon (PS) was reported by Canham,³¹ PS has been widely studied by many researchers resulting in the publication of various extended review articles and books. In spite of extensive studies, the mechanisms of the etching process as well as parameters involved in the chemical reactions are still not fully understood. Under controlled conditions, porous silicon layers consisting of disordered micro-pores and network of silicon interconnections can be formed.³²⁻³⁴ Nanoporous layers with quantum confinement effects can show properties such as enhanced luminescence, light trapping, and photon shifting (light transformation from ultraviolet to longer wavelengths).³³⁻⁴¹ It has therefore been a potential candidate for applications in optoelectronics, micro-electronics and photonics.^{38,42,43} It is well known that porous Si layers can successfully be used as an effective antireflecting coating (ARC) in crystalline silicon solar cells.⁴⁴⁻⁴⁸

Generally nanoporous layers have been formed and studied using three different etching techniques: electrochemical etching of Si in an HF-based solution (anodic etching);^{37-39, 45} chemical etching of Si in an HF/HNO₃ aqueous solution without applying any bias (stain etching);^{36,38} and introducing metal nanoparticles, such as Au, Pt, Ag, etc. to the Si surface prior to immersion in an HF solution.⁴⁹⁻⁵³ The latter known as metal-assisted chemical etching of silicon results in the formation of very long pores (nanoholes) with high aspect ratios.

2.2.1 Electrochemical etching of silicon wafers

Porous layers have mostly been formed by electrochemical etching of c-Si in an aqueous solution of HF. The anodization process is performed in a single tank with an aluminum plate as back contact or double cell with electrolytic backside contact. Circulation of the HF solution helps to obtain good depth uniformity by keeping the HF concentration constant. This might become more important during the growth of thick PS layers. The structure of PS layer, pore size, branching and porosity can be controlled by etching parameters. The condition for PS formation is determined by HF concentration, type of doping (p, n, n⁺, and p⁺), current density, anodization time and illumination. However, the current is generally kept constant during the etching process to have better control of thickness and structure of the PS layer as well as reproducibility of the process.

2.2.1.1 Current-voltage characteristics

By applying potential to cell electrodes, current flows through the Si/interface changing from electronic to ionic current. Fig. 2.6 shows the typical I-V curves for p- and n- type silicon in an HF solution. The I-V curves show similar behaviour as the Schottky diode which is expected at the interface of Semiconductor/electrolyte. However, in contrast, it can be seen that by changing the sign of majority carriers between n- and p-type silicon, the chemical reactions occurring at the interface remain the same. In the anodic region, the first current peak corresponds to the formation of a surface anodic oxide which results in the electropolishing of Si. At currents lower than the electropolishing current, pore formation occurs. Therefore, in order to form porous silicon, the current must be kept below the electropolishing threshold and must be carried by the injection of holes from Si substrate toward the interface. In the cathodic region, for both n and p-type substrate, Si does not dissolve in the HF solution and no specific reaction occurs. However, at high cathodic overpotentials, due to the reduction of water content of the solution at the Si/HF interface, hydrogen gas is formed. Fig. 2.7 shows the three different dissolution regions. Scale units are arbitrarily chosen and depend on the etching parameters as well as Si substrate doping. In region A, at lower currents, silicon pores are formed. In region C, at anodic over-potentials, Si electropolishing takes place resulting in complete removal of the silicon. The transition zone between pore formation and electropolishing is labeled B, in which these two mechanisms compete to determine the morphology of the PS layer.

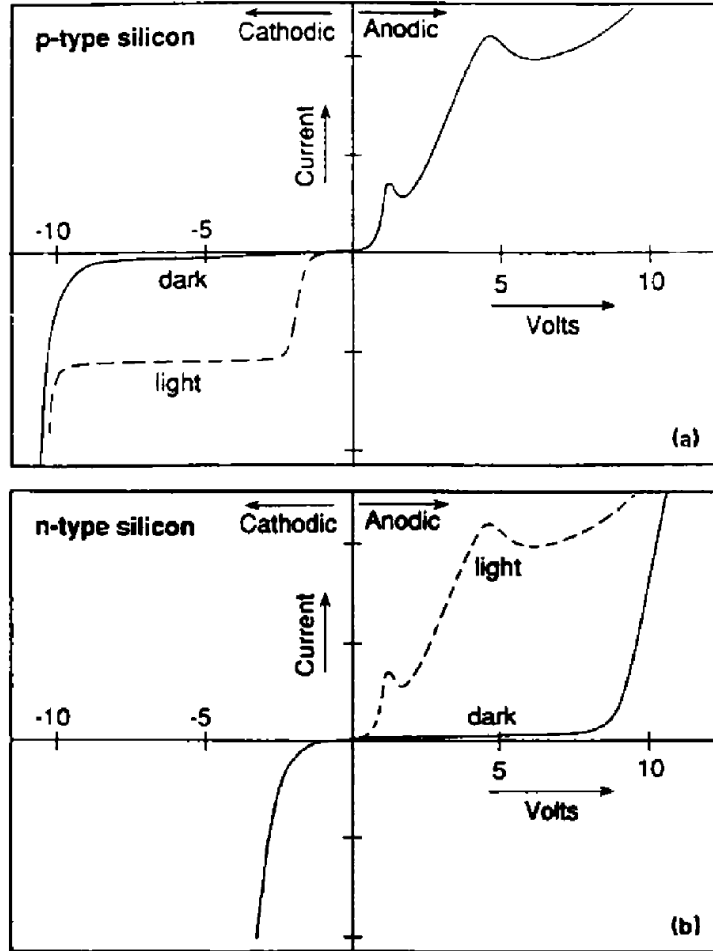


Figure 2.6: I-V characteristics for n- and p-type silicon. The solid line represents the dark response and the dashed line shows the response under illumination.⁵⁴

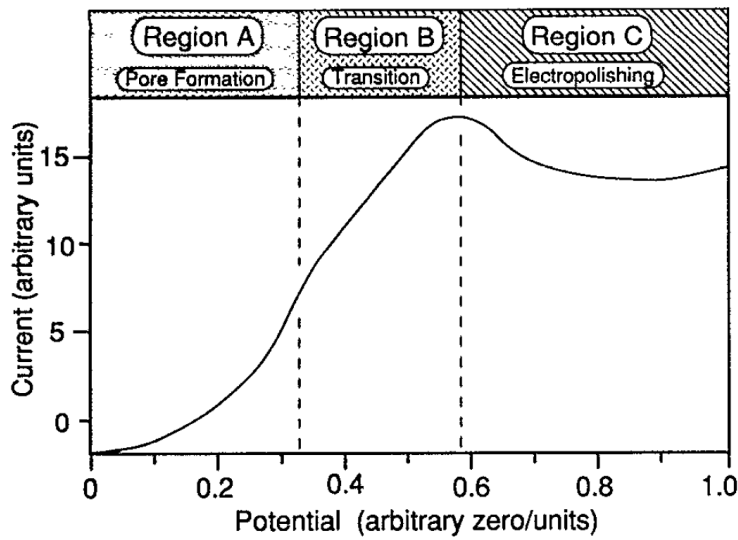
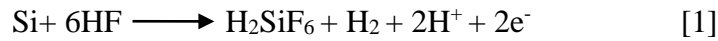


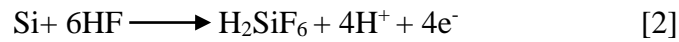
Figure 2.7: Anodic I-V characteristic of silicon in aqueous solution of HF showing different dissolution regions: pore formation, transition zone, and electropolishing.⁵⁴

2.2.1.2 Silicon dissolution chemistry

Although the exact chemical reactions of Si dissolution in the electrochemical etching process are still not well understood, given that Si does not dissolve in HF, charge carriers (holes) are required for both electropolishing and porous layer formation. Lehmann and Gösele⁵⁵ have proposed that injected holes from the anode attack the Si–H bonds on the Si surface, resulting in the substitution of hydrogen by fluorine atom. The silicon dissolution scheme is shown in Fig. 2.8. After substitution of hydrogen by fluorine atom, another fluoride ion attacks the second Si-H bond resulting in electron injection to the bulk Si and evolution of hydrogen gas which can be visibly observed during the etching process. Finally, the HF attack to the Si-Si back bonds results in the formation of a silicon tetrafluoride molecule. The chemical reactions for pore formation can be written as⁵⁶⁻⁶⁰:



In the pore formation process only two electrons are involved in the charge transfer process; while during electropolishing, all four available Si electrons are electrochemically active and the chemical reaction can be written as:



Therefore, by increasing the current density and approaching the electropolishing regime, production of hydrogen gas is reduced and smoothing of the Si surface begins.

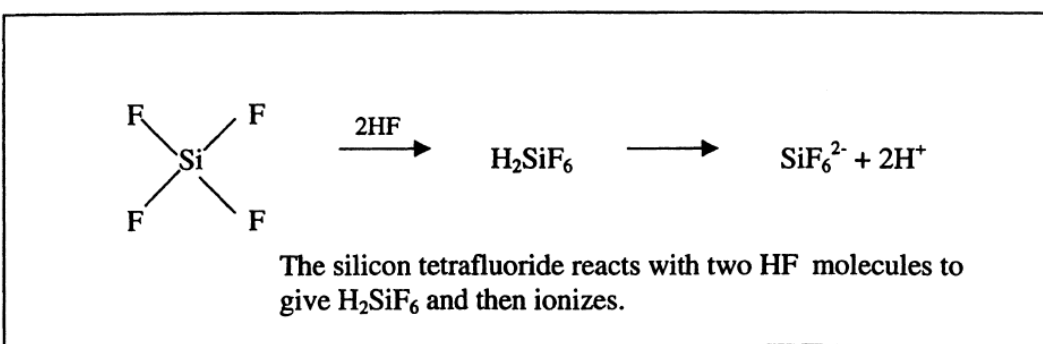
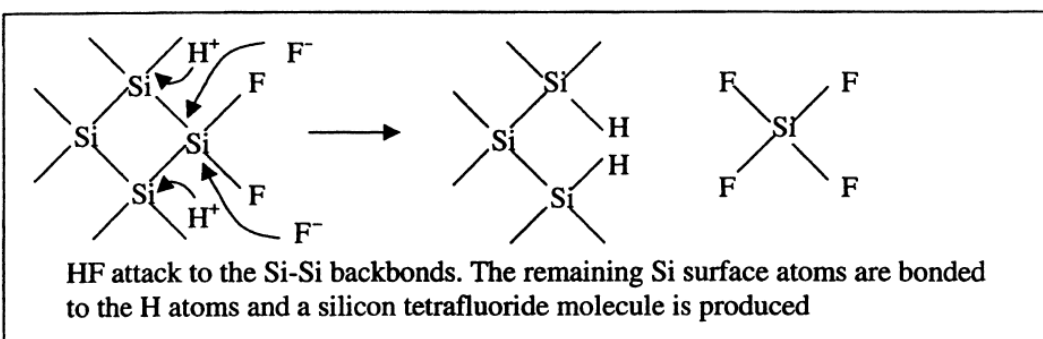
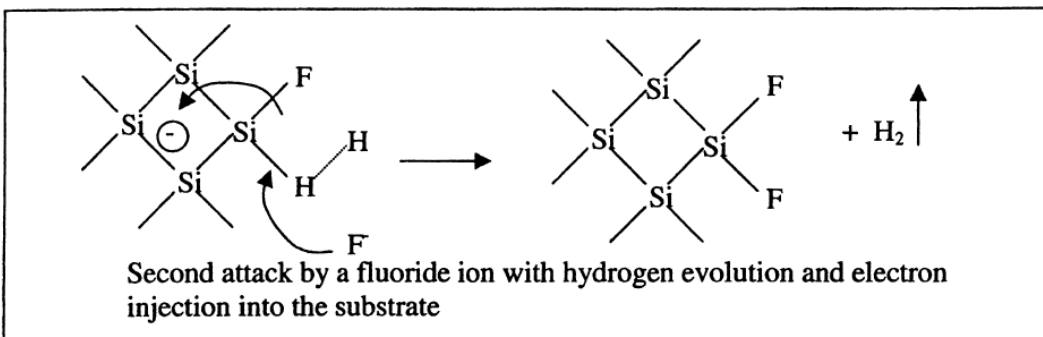
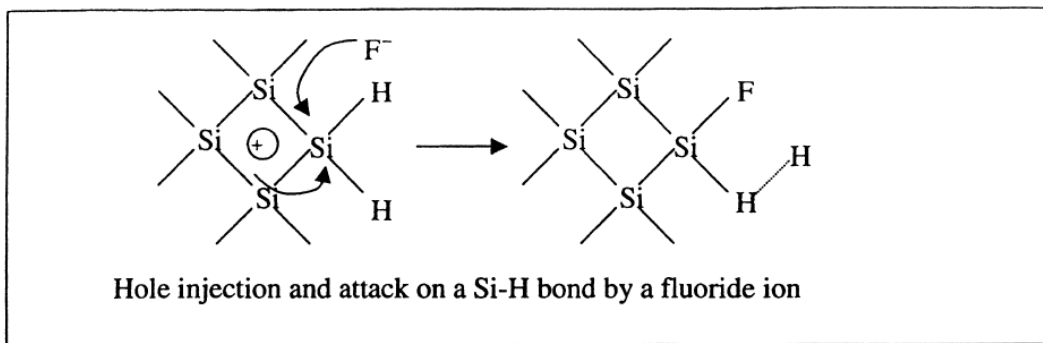


Figure 2.8: Silicon dissolution mechanism in HF solution resulting in pore formation.³⁸

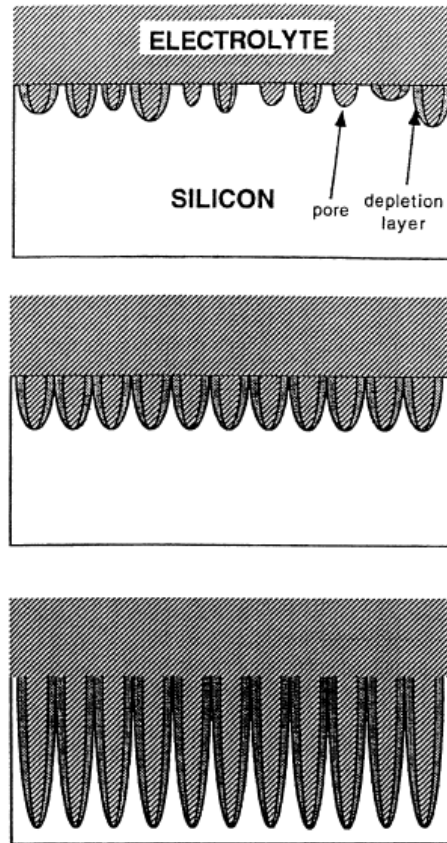


Figure 2.9: mechanism of porous layer formation. Random pores are formed on the surface of silicon by dissolution of Si atoms in HF solution. Formation of depletion region around pores results in directional growth of pores.⁸

2.2.1.3 Formation of macropores

Several models have been proposed to describe pore formation during the electrochemical etching process.^{38,56,61} Fig. 2.9 shows the mechanism of macropore formation in the PS layer. Assuming that the current density is less than the electropolishing threshold and holes are supplied (photogenerated), random pores are formed on the surface of silicon by dissolution of Si atoms in an HF solution. The depletion region formed around the pores, restricts the hole injection process from bulk Si. However, the etching process continues from the pore tips resulting in the directional growth of pores. As a result, these macropores can grow with constant diameters towards the deeper region in bulk Si.

The pore diameters and the size of nanocrystals are related to the depletion layer and the charge transfer mechanism. While the chemical reactions during the pore formation are not limited by mass transfer in the solution, in the electropolishing regime, reactions are under mass transfer control.

2.2.1.4 Morphology of porous silicon: effect of etching parameters

The structure and morphology of the PS layer strongly depends on the etching conditions and conductivity of the Si wafer and Si type. Among the morphological features of porous Si, such as orientation, branching, pore size, spacing, interconnections, etc., pore diameter of the PS is quantifiable and easily measurable. Direct study of the PS structure and the pore size as well as the nano-crystallites of the layer can be performed by transmission electron microscopy (TEM). However, the TEM preparation techniques used for PS samples may affect the final result. Different methods, such as cleavage, ion milling, and focus ion beam (FIB) assisted technique, have been used for preparation of PS samples. Among these preparation techniques, cleavage or scraping of the substrate might be more reliable and less destructive.^{37,60} In order to minimize the FIB-induced damage and to remove the introduced amorphous Si during sample preparation, the thinning process should be completed by ion bombardment having energies down to 50eV. Fig. 2.10 shows the transmission electron microscopy images of a mesoporous structure formed by the electrochemical etching of p⁻ Si with different porosities from 31% to 79%. As can be seen in this figure, pores were formed and extended along the [001] direction perpendicular to the Si substrate surface.

In highly doped n-type Si wafers, charge transfer is dominated by tunneling and therefore, the size of the pores is determined by the width of the depletion region which is typically about 10nm. While, PS layers formed on p-type Si contain very small pores less than 5nm with a uniform branching and interconnections. In lightly doped n-type Si wafers (without illumination), the carrier generation occurs at breakdown (Fig. 2.6) and a PS layer with pore diameter in the range of 10-100nm is formed. However, macropores with large diameters can be obtained under illumination. In general, in n-type Si compared to p-doped wafers, pore size and crystallites are larger. However, the size of pores and crystals decreases by increasing the doping concentration.

Fig. 2.11 shows the bright-field TEM micrograph of the non-luminescent PS layer with rod-like branching with diameters less than 10nm. In spite of high porosity, only very weak light emissions were observed.⁷ In comparison to Fig. 2.11(a), the porous layers in Fig. 2.11 (b-d) exhibited a strong photoluminescence (PL) emission. As can be seen in this Figure, the network of luminescent Si is composed of a nanostructure with Si columns of less than 3nm. As revealed

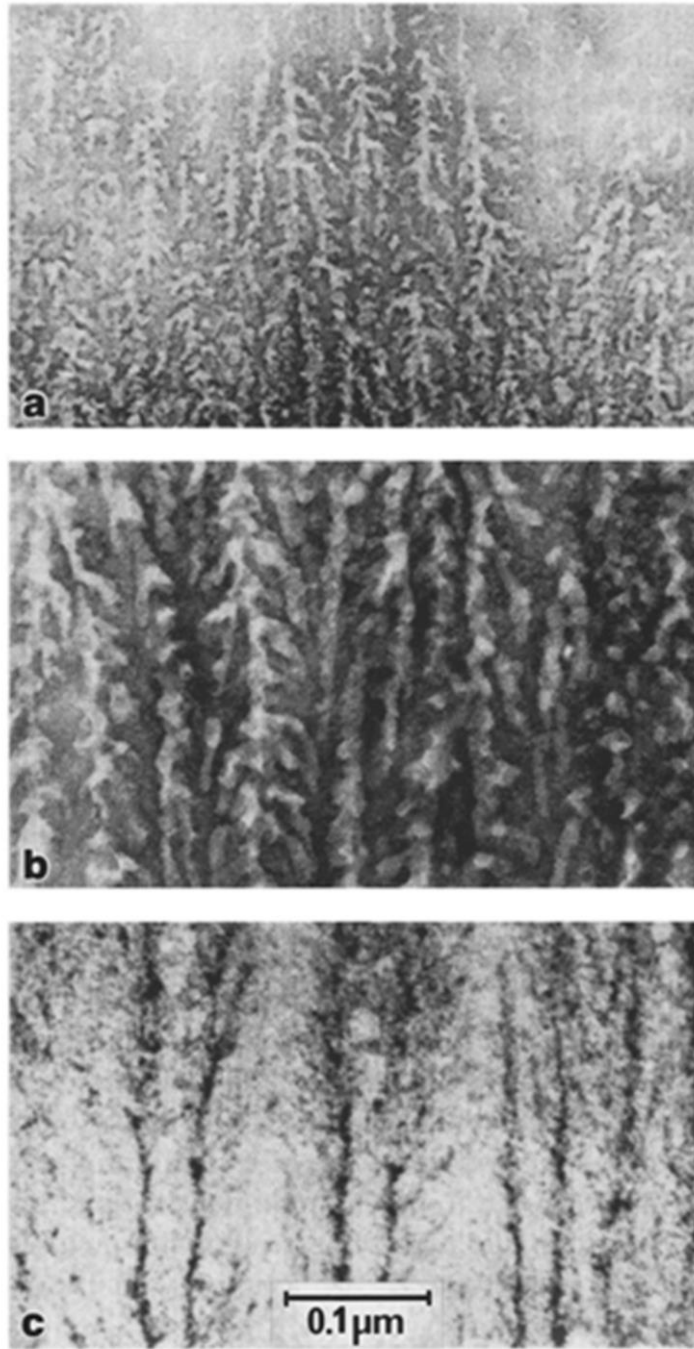


Figure 2.10: Transmission electron microscopy images of PS layer formed by electrochemical etching of p -Si showing a mesoporous structure with: (a) 31% porosity, (b) 51% porosity and (c) 79% porosity.⁵⁶

by transmission electron diffraction patterns (DP), the PS layer in Fig. 2.11(a) has a perfect crystal structure and misoriented nanocrystallites were not observed in DPs. A strong arcing of the main spots were observed in the DPs of the PS layers in Fig. 2.11(b-d), indicating the formation of very small isolated nanocrystallites. The latter leads to the conclusion that there is a correlation between Si nanocrystallites in the PS layer and strong photoluminescence.⁷

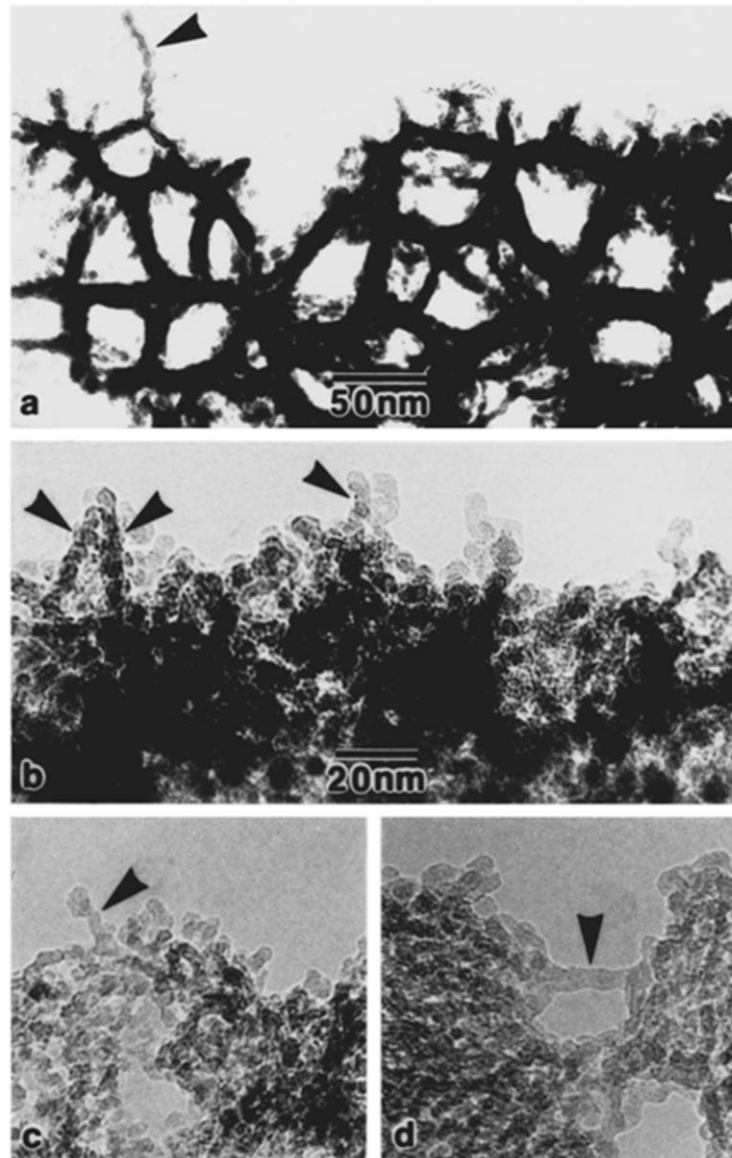


Figure 2.11: TEM images of nonluminescent (a) and luminescent (b-d) PS layers— nanometer scale, columnar Si structures arrowed.³⁷

2.2.1.5 Pore Orientation

Growth of pores is generally anisotropic and depends on the substrate orientation and direction of the carrier source (current flow). Typically, in a (100) Si substrate regardless of type, pores grow in $\langle 100 \rangle$ direction perpendicular to the surface of the substrate. It has been shown that the pores in the n-type Si substrate only grow in $\langle 100 \rangle$ and $\langle 113 \rangle$ directions.^{62,63} This has been attributed to the slow rate of H-passivation on the surfaces of $\{100\}$ and $\{113\}$ planes.⁶³ Fig. 2.12 shows the preferential crystallographic pore propagation, at the pore tips, in n-type Si substrate (Etching and substrate orientations are shown by arrows). As can be seen in this image, the main pores propagate straight in the preferred orientation, most likely due to the tendency of the anisotropic etching along the $\langle 100 \rangle$ direction.

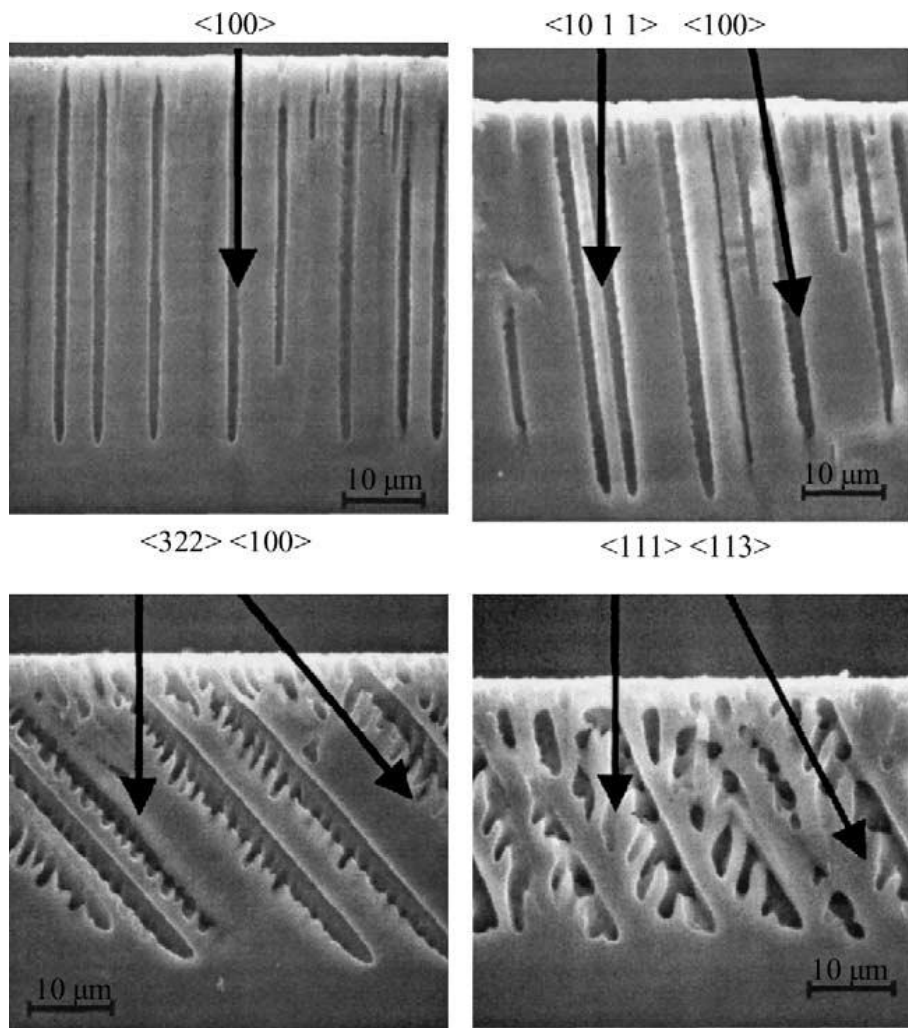
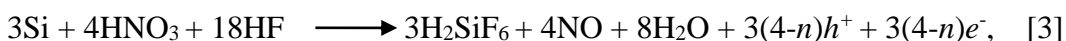


Figure 2.12: Orientation dependence of macropores in n-type Si substrate. Etching and substrate orientations have been shown by arrows.⁶³

2.2.2 Stain etching of silicon

Porous silicon layers can be produced by immersing of Si wafers in an HF/HNO₃ aqueous solution without applying any bias.⁶⁴⁻⁶⁸ Fathauer et al.⁶⁴ reported the luminescent silicon formed by “stain etching” in 1992. Although the method is useful for formation of PS layers on silicon with high resistivity or Si structures implemented on electrically insulating substrate; PS layers obtained by stain etching show lower photoluminescence emission as compared to electrochemically-etched porous silicon.⁶⁹ In the stain etch process, the same as electrochemical etching, holes are needed for the initiation of reactions. The surface of the silicon is oxidized by hole injection from HNO₃ followed by HF-etching similar to the anodization process. The reactions during pore formation can be written as:⁷⁰



Where n is the average number of holes which is required for dissolution of one Si atom. Fig. 2.13 shows the cross-section, TEM image of the Si/PS interface illustrating the transition between Si and the PS layer. As can be seen in this Figure, smooth transition from bulk Si to the high porosity PS layer can be obtained by control of the HNO₃ concentration. This becomes very important when PS layer formation is applied as a post-processing technique to solar cells and control of emitter thickness is crucial.

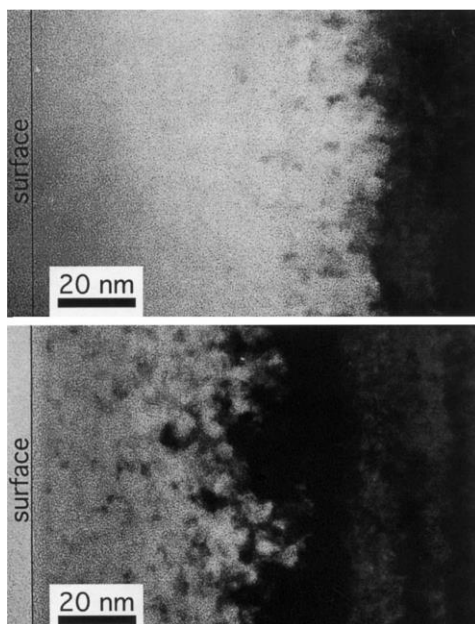


Figure 2.13: Cross sectional TEM image of PS layers prepared by stain etching of Si with different HNO₃ concentrations. Top - 17s, HNO₃=0.024 mol/l; bottom-55 s, HNO₃=0.006 mol/l.⁴⁴

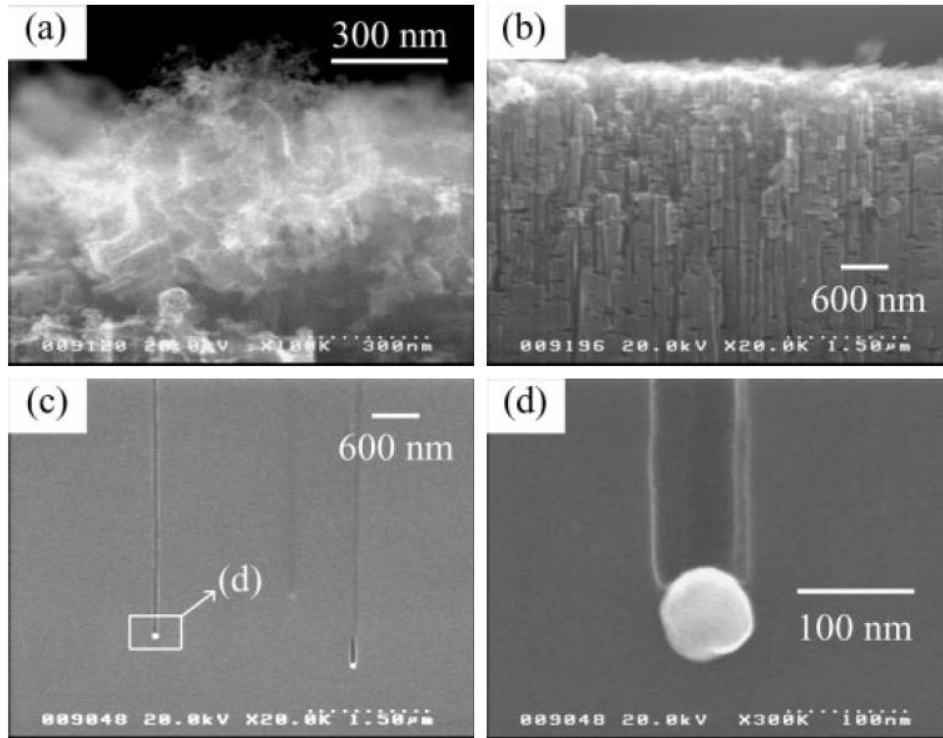


Figure 2.14: Shows cross-sections of PS layer formed on p-type Si wafer using Ag nanoparticles as the catalyst (After 30 min etching in a mix solution of HF and H₂O₂). (a) near the surface, (b) in a region about 3 μm from the surface, (c) in a region about 40 μm from the surface, and (d) magnified image in (c).⁵³

2.2.3 Metal-assisted etching of silicon

Long pores with high aspect ratios can be obtained by introducing metal nanoparticles, such as Au, Pt, Ag, etc. to the Si surface prior to immersion in an HF solution.⁴⁹⁻⁵³ This technique, known as metal-assisted chemical etching of silicon, can be used to produce nanoporous silicon utilizing metal particles to catalyze Si etching. Introducing nanoparticles to the surface of Si (by physical deposition techniques such as e-beam, sputtering, etc. or by using chemical solutions such as H₂AuCl₄) and immersion of the sample in HF:H₂O₂:H₂O solution, results in catalytic decomposition of H₂O₂ at the metal nanoparticle surface and local oxidation of the Si. This oxide layer is subsequently removed by HF content of the solution resulting in pore formation.

Fig. 2.14 shows the SEM image of a PS layer formed on p-type Si(100) using a metal assisted etching technique.⁵³ After the deposition of Ag nanoparticles on the surface of Si, samples were etched for 30 min in a mix solution of 10% HF and 30% H₂O₂ in the dark at room temperature. Fig. 2.14(a) shows the distribution of micropores close to the surface. Fig. 2.14(b) and (c) show cylindrical nanoholes with high aspect ratios extended to a deeper region of the substrate.

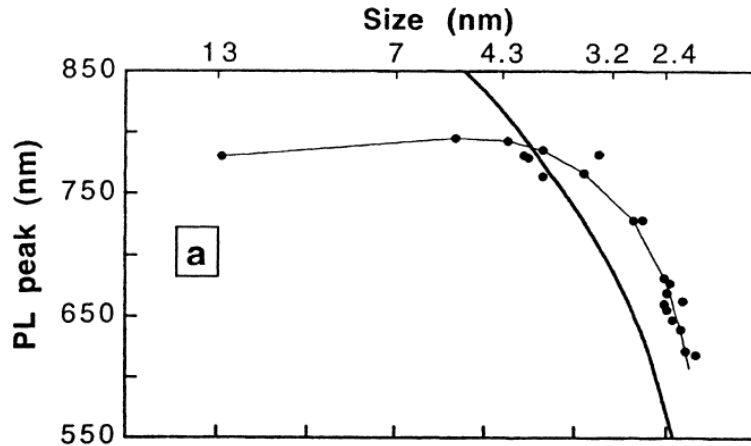


Figure 2.15: Photoluminescence peak wavelength versus crystal size for PS layer obtained by anodization of p-Si wafers. The thick line is obtained from first-principle calculations.⁷²

The density of these holes is reduced by moving toward the bulk Si. The latter can be employed for fabrication of graded-density structures for solar cell applications.

2.2.4 Visible luminescence from porous silicon

Since the discovery of visible luminescence from porous Si,³¹ the optical properties of the PS layer have been extensively studied by many researchers. In spite of these efforts, the exact mechanism of PL emission in nano-structured porous layers has not yet been determined. Different luminescence mechanisms have been considered and proposed to be responsible for visible emission of nanoporous silicon. Mainly three different models have been discussed: 1) luminescence due to native oxide formed in the PS layer or defects in the SiO_x; 2) Visible photoluminescence based on recombination of carriers confined in Si nano-crystallites or nanoscale interconnections (quantum confinement effect);^{31,37} 3) surface effect of Si nano-crystallites.⁷¹

Fig. 2.15 shows the correlation between the photoluminescence peak wavelength and size of nanocrystallites (PS layers have been obtained by electrochemical etching of p-type Si). As can be seen in this figure, a considerable blueshift in the PL peak occurs by decreasing the size of crystallites to less than 4.5nm. It has also been reported that the position of the visible peak depends on the porosity and the applied current density during the etching. Fauchet et al.⁷² reported that not only the spectral position, but also the PL peak intensity is related to the layer

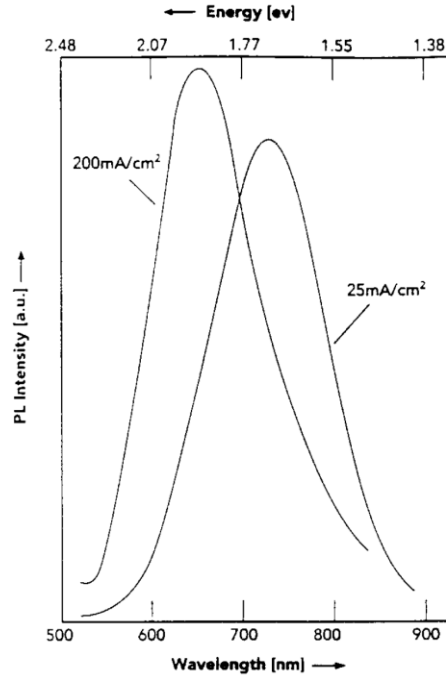


Figure 2.16: Photoluminescence spectra of PS layers formed by applying current densities of 25 and 200 mA/cm² during electrochemical etching process.⁷³

porosity and generally improves for high porosity layers. Fig. 2.16 shows the PL spectra of porous Si for two different current densities during electrochemical etching. By increasing the current density, a blue shift of the PL peak as well as increased intensity were observed. However, according to the quantum confinement model the blueshift can also be attributed to the bandgap opening.

2.2.5 Porous Si in solar cells: PS as an AR coating

Applications of porous silicon fabricated by both electrochemical and chemical etching methods have been extensively studied in solar cell structures.⁴⁴⁻⁴⁷ An optimized PS layer formed on a diffused emitter of solar cells particularly multicrystalline Si solar cells can efficiently reduce the total reflectivity to less than 5%. A PS layer, as an antireflection coating of solar cells, can be considered based on three different aspects: 1) using a graded-density PS layer results in the efficient suppression of reflectivity in the broad spectral range (less than 2% in the wavelength region from 400 to 1100nm) which can be a potential candidate for replacing the conventional antireflection coatings based on interference in silicon solar cells; 2) bandgap opening due to the quantum confinement effect in nano-PS layer with nanometer-scale network (crystallites and interconnections). The latter results in highly transparent porous Si minimizing the absorption of

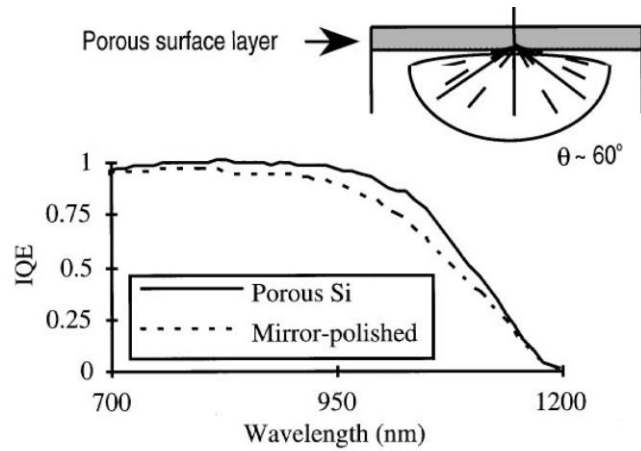


Figure 2.17: Internal quantum efficiency spectra for conventional cell structures with a mirror-polished surface and a porous Si layer.⁴⁴

incident photons inside the PS layer; 3) due to the visible luminescence from nano-structured PS, the PS antireflection coating can be employed as a down shifting layer to optimize the high energy photon absorption. Furthermore, the light-diffusing behavior and surface passivating capabilities of PS layers have been considered as an advantage for application in solar cells. Surface passivation of p-Si rear contact solar cells by a thin layer of porous silicon can effectively improve the efficiency of these cells.⁷⁴ Fig. 2.17 shows a significant improvement of long-wavelength internal quantum efficiencies (IQE) by applying a PS layer to the conventional silicon solar cells (light diffusing effect).

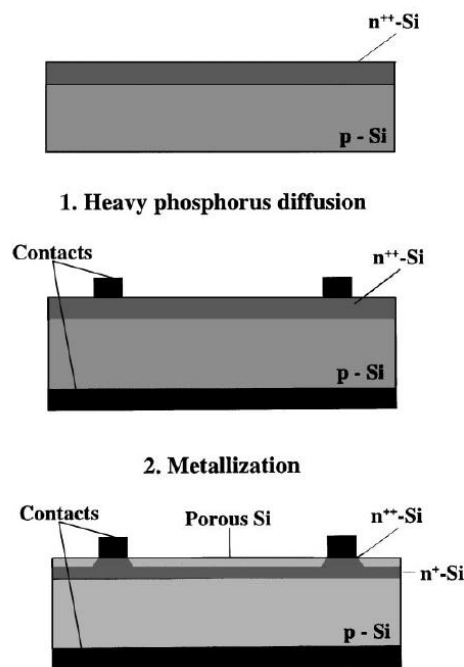


Figure 2.18: Process sequence for fabrication of selective emitter with porous layer.⁴⁴

One of the advantages of the PS layer formation on a diffused emitter is simultaneous achievement of an efficient antireflection coating and a selective emitter structure. Fig. 2.18 shows a simple, low-cost process sequence for fabrication of a solar cell with a PS selective emitter. Since the selective emitter is formed after the front-side metallization step, the etching process in HF solution should be relatively limited to less than a minute or fabricated contacts must be protected.

2.3 Semiconductor quantum dots

Semiconductor nanocrystals are crystalline particles with a diameter ranging from 2 to 10nm. Due to the quantum confinement effect in these nano-particles, when the dimensions are smaller than Bohr radii, they are also referred to as “quantum dots”. At these dimensions, energy levels are no longer continuous and they are strongly size dependent. UV-VIS absorption spectra of CdSe QDs with different sizes are depicted in Fig. 2.19. Due to the size-tunable emission and absorption properties of QDs, these zero dimensional semiconductors have become a potential candidate for applications in optoelectronic and photonic devices. QDs have been successfully

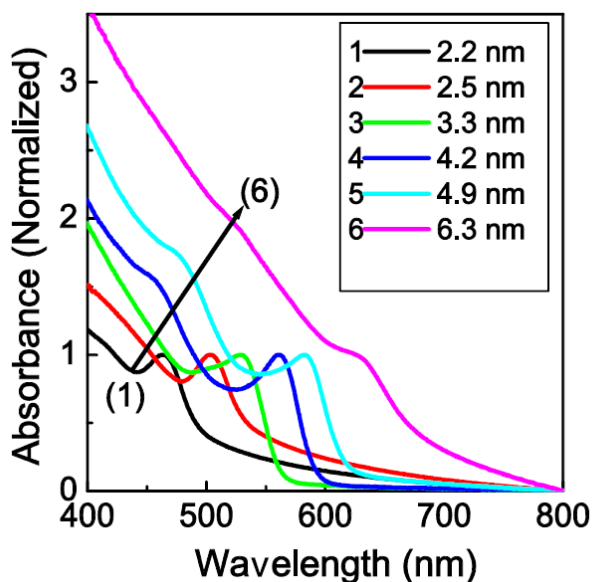


Figure 2.19: Absorption spectra of CdSe QDs with different sizes.⁷⁵

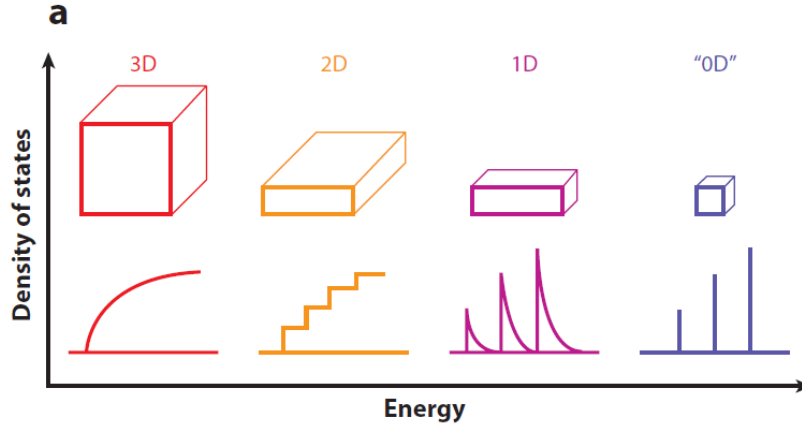


Figure 2.20: Density of states in one band of a semiconductor as a function of dimension. Energy levels become discrete for zero dimensional semiconductors (smaller than Bohr radii).⁷⁶

applied to different optoelectronic devices, working in visible and infrared regions, such as lasers,⁷⁷ light-emitting diodes,⁷⁸ photodetectors,⁷⁹ and solar cells.⁸⁰⁻⁸²

2.3.1 Quantum confinement effect

When the dimension of QDs is reduced to less than several nanometers, in the range of the Bohr radii (an average distance of electron and hole during exciton formation), the quantum dots exhibit a discrete and tuneable structure, in their optical and electrical characteristics. Fig. 2.20 shows the density states of semiconductors as a function of dimension indicating that energy levels become discrete for zero dimensional semiconductors. Due to the quantum confinement effects, QDs exhibit remarkable size-dependent physical properties.

Brus⁸³ has derived an analytical expression that describes the size-dependence of the effective bandgap energy:

$$E_g^{\text{QD}} = E_g + \frac{\hbar^2 \pi^2}{2R^2} \left[\frac{1}{m_h} + \frac{1}{m_e} \right] - \frac{1.8e^2}{\epsilon R} \quad [4]$$

Where, R and ϵ are the radius and the dielectric constant of the semiconductor QD. Therefore, the bandgap of QDs and hence the emission peaks can be tuned by adjusting the radius of nanoparticles.

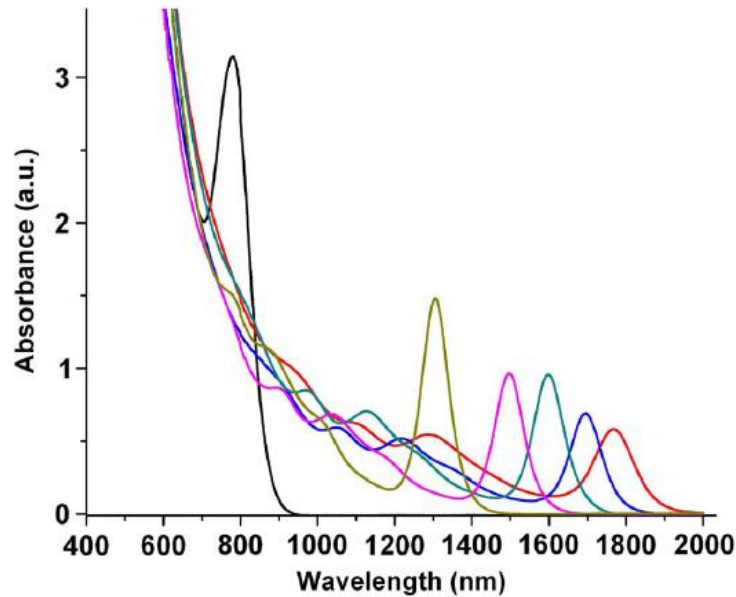


Figure 2.21: Size-dependence tunability of the absorption spectrum in PbS colloidal quantum dots.⁸⁷

2.3.2 Solution-processed quantum dots

Due to their simplicity and stability, colloidal quantum dots have been considered as a potential candidate for applications in various organic and inorganic optoelectronic devices, such as light-emitting diodes, optical modulators, photodetectors, and solar cells.⁸⁴⁻⁸⁶ Fig. 2.21 shows the correlation between the absorption peak and size of PbS colloidal nanocrystals. By reducing the QDs diameter to 3nm, the corresponding wavelength of absorption peak decreases to about 800nm. Solution-based QDs can be easily transferred and integrated to any type of substrates or can be applied as a post-processing step to fabricated devices. Colloidal quantum dots can be deposited by various methods, such as dip-coating, spin-coating, or inkjet printing on silicon, glass or flexible substrates.⁸⁷

2.3.3 Application of QDs in solar cells

2.3.3.1 Down-shifting layer

The absorption spectrum of colloidal quantum dots integrated into functional oxides, dielectric matrix, etc. can be matched to the spectrum of the sun's energy reaching the earth. Colloidal

quantum dots can be deposited by various methods, such as dip-coating, spin-coating, or inkjet printing on silicon, glass or flexible substrates. Next generation photovoltaic technology based on quantum dots and concepts such as down-conversion and down-shifting is promising significant increases in conversion efficiency. The concept of down-conversion is based on utilization of high energy photons to produce two or more low-energy photons (ideally above the band gap) and down-shifting improves the performance of the solar cells by shifting the short wavelength photons to lower energy photons for which the quantum efficiency is higher.

Furthermore, ability to develop and deploy QD layers, embedded in wide-bandgap matrices such as SnO₂, ZnO, etc., is key to the realization of high efficiency third generation solar cell architectures, such as multiple exciton devices, intermediate bandgap structures, hot carrier devices etc.

2.3.3.2 QDs-sensitized solar cells

Dye-sensitized solar cells (DSSCs) based on nanostructured metal oxides have been considered as a potential candidate for the next generation of solar cells.^{88,89} Dye molecules, deposited onto a high porosity metal oxide structure, absorb optical photons and inject electrons into the metal oxide conduction band upon excitation. Although conversion efficiencies of about 11% have been obtained, further improvement of DSSCs efficiency is possible by employing inorganic quantum dots (QDs) such as CdS, CdSe, PbS, etc., which optimize the photon absorption in the entire spectral range. These photovoltaic devices, which are based on the sensitization of nanostructured metal oxide films using quantum dots, are called QD-sensitized solar cells (QDSSCs).⁹⁰⁻⁹²

Chapter 3

Experimental results of material properties and characterization studies of silicon spheres

3.1 Introduction

Spherical silicon technology as compared to other methods such as FZ technology, CZ technology or the cast silicon method, is relatively new technology. In ingot technologies, the silicon wafer is obtained through cutting and polishing processes which produce waste material. Although the ingot technologies produce high quality silicon, due to the waste, further cost reduction is difficult. In spherical silicon technology, silicon spheres can be produced in different sizes (1-2mm) directly from the molten silicon at high speeds. The crystalline quality and impurity level of fabricated spheres are important and affect the electronic properties of the silicon and hence the cell performance. In this chapter we discuss the material properties and results of characterization studies performed on silicon spheres. Section 3.2 covers the scanning electron microscopy (SEM) study of the silicon spheres distributed on a carbon tape. The SEM images reveal the shape and surface morphology of the silicon spheres as well as surface defects. In section 3.3 we investigate the crystallinity of silicon spheres by means of a single-crystal X-ray diffractometer and an X-ray powder diffraction (XRD) machine. Single-crystal X-ray diffraction analysis can provide detailed information about the crystallinity, lattice of crystalline

structure and also defects in a single sphere. However, in the powder XRD method a small portion of the sample (few spheres) is irradiated. Crystallinity of the spheres was also investigated by transmission electron microscopy (TEM) and it is discussed in section 3.4. Bright-field TEM images and transmission electron diffraction (TED) measurements can provide direct images of morphology and crystallinity of the samples. In section 3.5 and 3.6, the result of secondary ion mass spectroscopy (SIMS) studies and lifetime measurements is presented. In order to access the bulk of the spheres for SIMS analyses and lifetime measurements, silicon spheres are embedded in a clear epoxy and polished to the mid-section.

3.2 Scanning electron microscopy study

Silicon spheres used in this research are fabricated by spheroidization of molten silicon. This technique initially developed by Texas Instruments (TI), is based on spheroidization of molten silicon by surface tension. The starting material is in poly silicon form and can be powder silicon or granular silicon. Powder silicon can be obtained from various sources with different quality levels, such as kerf loss from wafer cutting which has a higher quality and metallurgical grade silicon which has a lower quality level. Using a high power arc lamp, a small amount of silicon powder is optically fused and melted to form a spherical shape of about 1mm size. This process including the melting and solidification is done in a very short time, less than a second. Therefore, the spheres obtained initially are not single crystal and they are expected more to have a poly-crystalline structure. Further annealing process at high temperatures (above 1400°C) is performed to obtain higher crystalline quality and elevated impurity levels. Prior to each annealing process, spheres are covered by a layer of thermal oxide and this layer of oxide prevents the spheres from sticking together. During the annealing process and recrystallization, impurities are moving towards the surface oxide layer and are segregated at the surface of the spheres. This oxide layer along with segregated impurities is etched away using a chemical etch process.

Fig. 3.1 shows scanning electron microscopy images of the spheres obtained by the optical fusing of silicon powder. Size of these spheres is about 600um in diameter. As can be seen in this image, the shape of these spheres is not perfectly spherical and they tend to adopt piriform shape. SEM images obtained from surface of crystalline spheres revealed microscopic defects on the

surface. During chemical etching processes, due to the higher rate of etching, these defects appear on the surface of the crystalline spheres. Defects on the surface of silicon sphere, mostly in the form of point defects, may originate from impurity sites such as oxygen or lattice defects in the crystalline structure of spheres. It is reported that the density of point defects is higher at the surface of the silicon sphere than central regions.⁹³

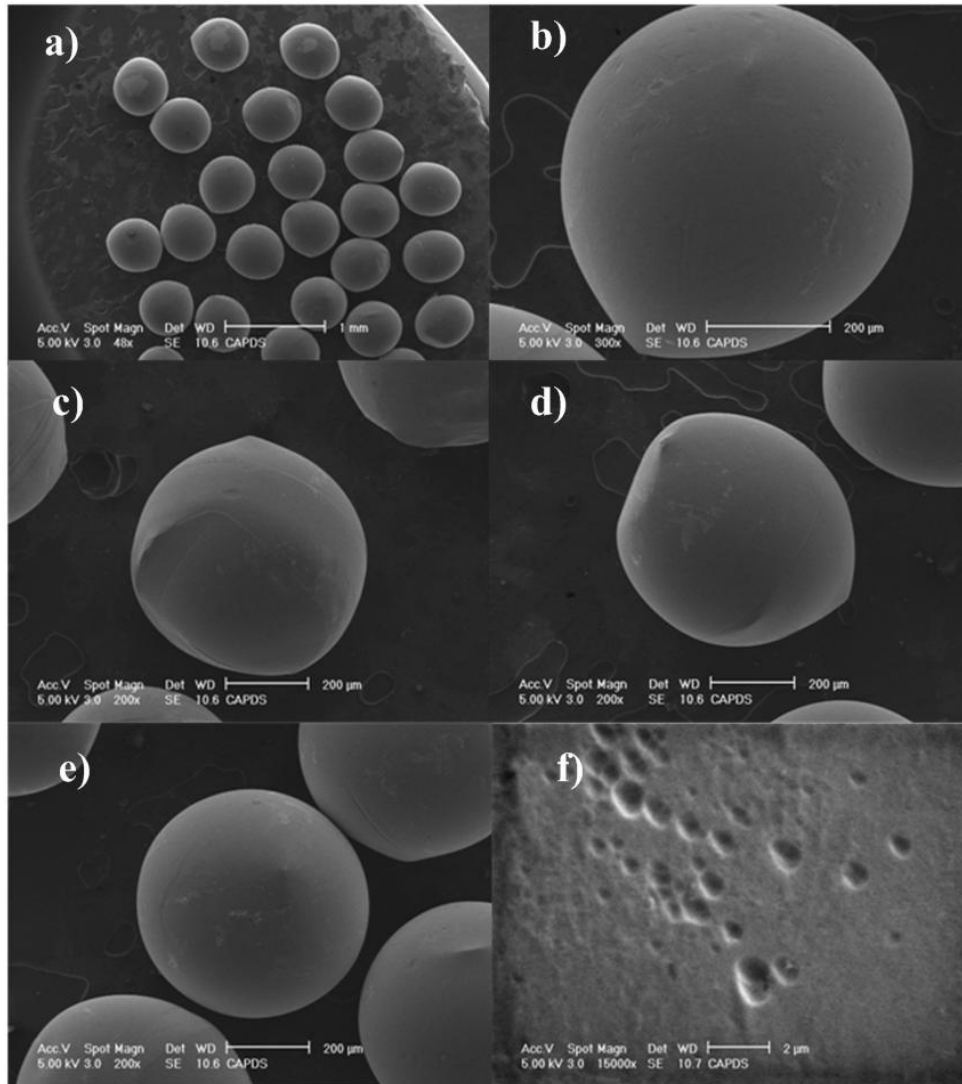


Figure 3.1: a) Scanning electron microscopy image of silicon spheres distributed on a carbon tape. Size of these spheres is about 600 μm in diameter. b-e) After melting and recrystallization process, due to the surface tension, optically fused powder silicon turns to a silicon sphere. However, shape of these spheres is not perfectly spherical and they tend to adopt pear-shaped morphology. f) Microscopic defects can be observed on the surface of spheres.

3.3 Investigation of the crystallinity of silicon spheres by X-ray diffraction

The crystalline structure of silicon spheres has been investigated using two different methods of X-ray powder diffraction and single-crystal X-ray diffraction. For powder XRD, spheres must be arranged on a substrate, while the crystallographic structural analysis of single sphere can be performed by the single-crystal X-ray diffraction method. Single-crystal XRD can provide detailed information about the crystallinity, lattice of crystalline structure and also defects in a single sphere.

3.3.1 X-ray powder diffraction

Powder XRD is a common technique used to analyze the crystalline structure of powder samples, thin films coated on substrates, and sintered pellets. In this technique, the x-rays generated in an x-ray tube are directed to the sample and diffracted x-rays are collected and counted by a detector. The principle is based on Bragg's law ($n\lambda=2d_{hkl} \sin \theta$), in which d_{hkl} is the distance between a family of planes and θ is the angle between the incident beam and the sample. The wavelength, λ , is constant and depends on the type of source which is used for x-ray generation. In this experiment, we use a $\text{CuK}\alpha$ source with a wavelength of approximately 1.54Å. At specific angles, at which Bragg's law is satisfied, the interaction of the incident x-rays with the sample creates constructive interferences which are collected by the detector. These constructive interferences generate a peak in the XRD pattern which belongs to a family of the planes of atoms. The powder XRD analysis is more suitable for samples with polycrystalline structure. In a polycrystalline sample, we assume that there is enough number of crystallites which are randomly oriented and each represents a set of planes that diffract the incident x-ray at a specific angle. Therefore, by scanning the sample over a proper range of 2θ angle, all peaks of polycrystalline structure will appear in the XRD pattern.

In the case of the silicon spheres arranged on a substrate, only a few spheres will be irradiated by the x-ray beam and only a small fraction of the scattered x-ray can be collected and counted by the detector. If there is polycrystalline structures or defects in the silicon sphere structure, powder XRD can easily reveal that in the collected XRD pattern. However, if the structure is close to the single-crystal form or multi-crystal only few peaks or even no peaks might be observed in the x-ray spectrum.

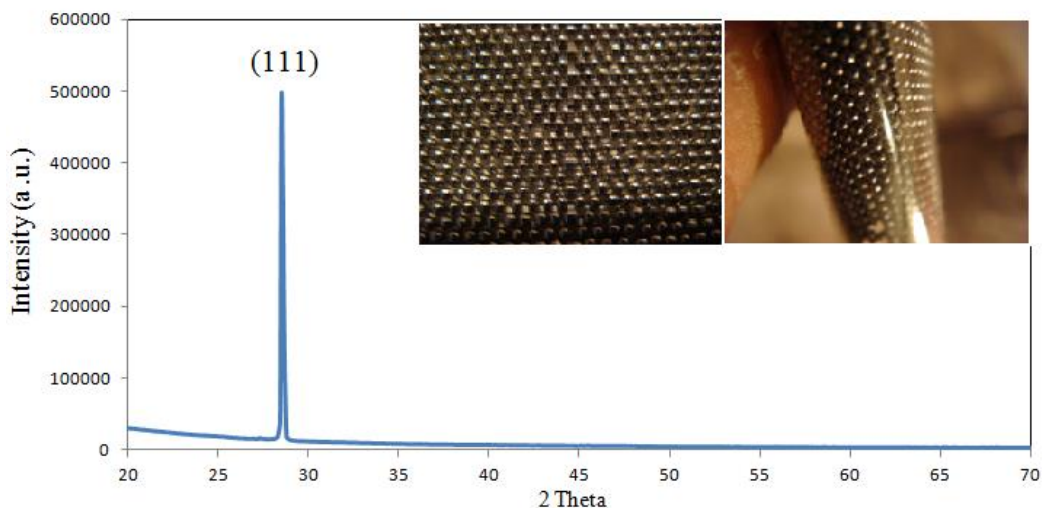


Figure 3.2: X-ray diffraction pattern of silicon spheres arranged and embedded on a flexible polymer substrate. Only the peak corresponding to (111) planes appeared in the XRD pattern. The inset shows the optical image of the arranged silicon spheres and the polymer substrate used for XRD measurements.

Fig. 3.2 shows the x-ray diffraction pattern of silicon spheres arranged and embedded on a flexible polymer substrate. The spheres are closely packed to have more spheres irradiated by the incident x-ray beam. However, the widest divergence slit was chosen for the experiments; only a few silicon spheres (10 to 15) will be irradiated by the incident x-ray. As can be seen in Fig. 3.2, only the peak corresponding to (111) planes appeared in the XRD pattern. Most of the x-ray diffraction patterns collected through this method only revealed one peak or no peaks was observed in the XRD pattern. This indicates the structure of silicon spheres is close to single-crystal or multi-crystal. The inset in this figure shows the optical image of the arranged silicon spheres and the polymer substrate used for XRD measurements.

The same experiment was performed on the silicon spheres embedded in an aluminum foil. The samples were chosen among the fabricated cells with an emitter diffusion. Fig. 3.3 shows the x-ray diffraction pattern of silicon spheres embedded in an aluminum foil. As can be seen in this Figure, a strong peak corresponding to (311) Si planes and a very small peak corresponding to (111) planes appeared in the XRD pattern of silicon spheres. The (311) peak at 56° (2θ angle) consists of $K_{\alpha 1}$ and $K_{\alpha 2}$ doublet and a very small peak due to the K_{β} diffraction was observed in the XRD pattern. In short, based on the x-ray powder diffraction patterns, the structure of silicon spheres is close to single crystal. Therefore, we also carried out single-crystal x-ray diffraction analyses on individual spheres.

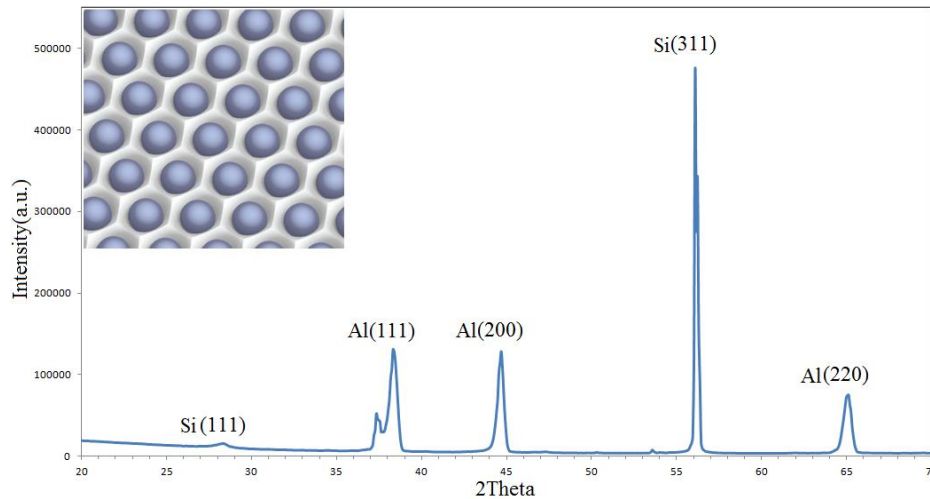


Figure 3.3: X-ray diffraction pattern of silicon spheres embedded in an aluminum foil (One of the fabricated cells). A strong peak corresponding to (311) planes and a very small peak corresponding to (111) planes appeared in the XRD of silicon spheres. The inset shows the schematic of silicon spheres embedded in a perforated aluminum foil.

3.3.2 Single-crystal x-ray diffraction

Fig. 3.4 shows an individual silicon sphere mounted on a thin glass fiber for single-crystal XRD measurements. A silicon sphere attached to the thin glass fiber and mounted on a goniometer can rotate to different angles while the silicon sphere is centered in the x-ray beam. The x-ray beam generated in an x-ray tube is directed to the sample and the diffracted x-ray is collected by a CCD (charge-coupled device) detector. In this image, the distance between concentric circles is about 100 μ m. Since the glass fiber structure is amorphous the diffracted x-ray will not interfere with the diffractions from the crystalline structure of silicon spheres.

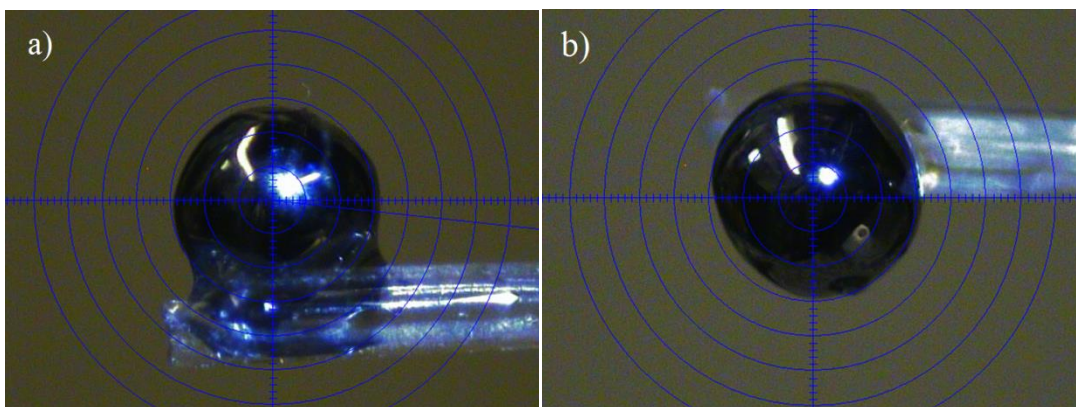


Figure 3.4: Shows an individual silicon sphere mounted on a thin glass fiber and centered in the x-ray beam for single-crystal XRD measurements. The x-ray beam generated in an x-ray tube is directed to the sample and the diffracted x-ray is collected by a CCD (charge-coupled device) detector.

For this characterization experiment, samples are irradiated by monochromatic x-ray and more than 1000 shots are collected at different angles. Fig. 3.5 shows the collected 2D diffraction patterns from the crystalline structure of silicon spheres. If the structure is single crystal, separated bright spots are expected in the 2D diffraction pattern. However, in the case of polycrystalline or amorphous structure, rings are formed. Fig. 3.5 (a) and (b) show strong reflections from single crystal silicon while at other angles, (c) and (d), twin-crystal diffractions were observed. In most of the images, twin-crystal diffractions corresponding to a different crystal orientation were observed.

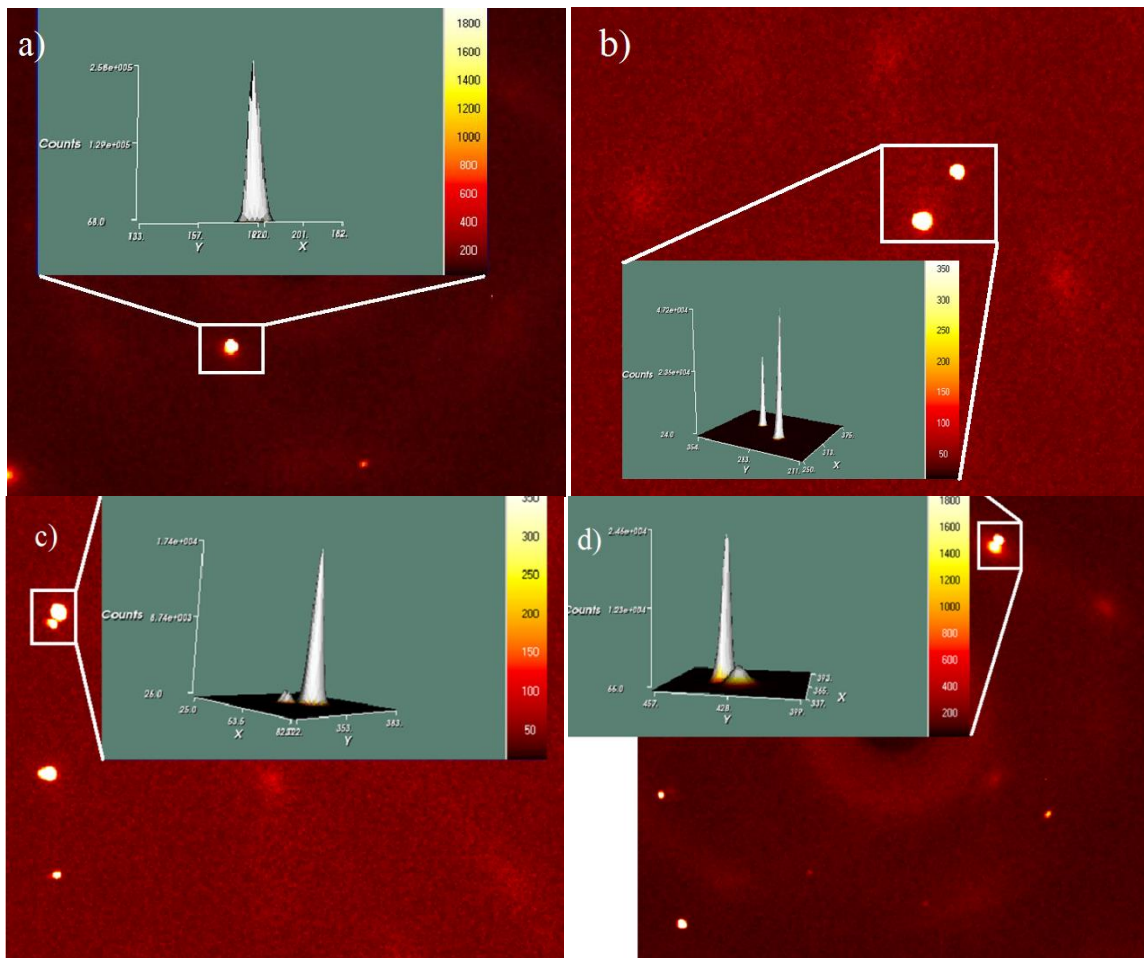


Figure 3.5: 2D diffraction patterns of the crystalline silicon structure collected by the CCD detector. (a) and (b) show the diffractions from single crystal silicon. The intensity of the reflections (bright spots) is depicted in the insets showing strong symmetric peaks. (c) and (d) are showing diffractions from twin-crystals. The insets illustrate a high and low intensity peaks for each of these reflections.

Simulated powder diffraction diagram

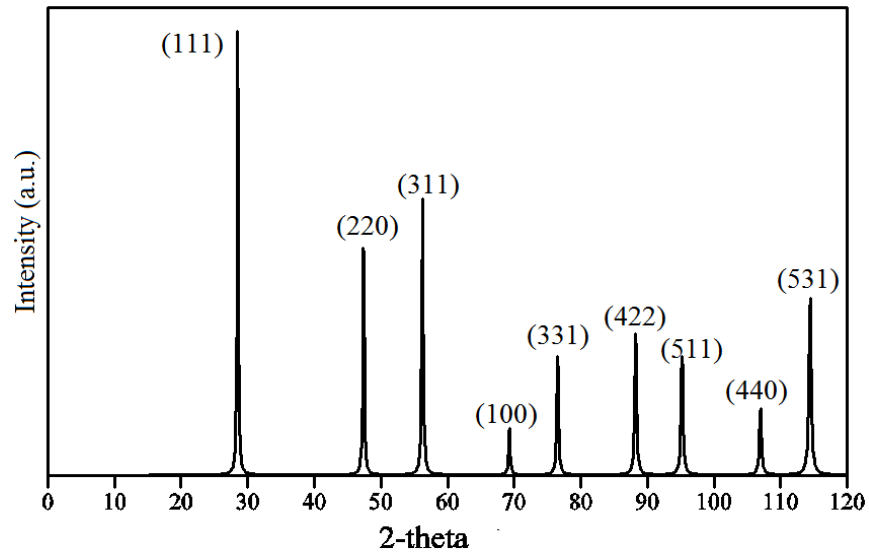


Figure 3.6: Simulated XRD pattern of crystalline structure of the silicon spheres showing the cubic phase crystal structure. The XRD simulated by Apex2 software program using the collected reflections (bright spots) from different family of planes in the crystal structure.

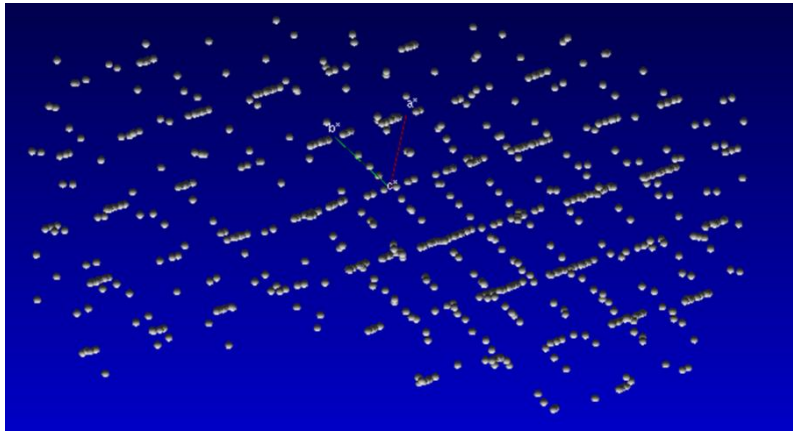
Based on the 2D diffraction patterns obtained by single-crystal XRD analyses, we can conclude the structure of silicon spheres is close to single crystal however, twin-crystals exist in the structure.

Since each diffraction spot corresponds to a specific family of parallel planes and the angle and the intensity of each peak is recorded, the crystalline structure of the sample can be obtained using the Apex2 software program. The simulated x-ray diffraction pattern is shown in Fig. 3.6. The crystalline structure corresponds to cubic phase crystal structure. The position and intensity of the peaks for cubic structure, obtained from the XRD database, is shown in table 3.1. As can be seen in the simulated XRD pattern and the table, (111) reflection has the highest intensity.

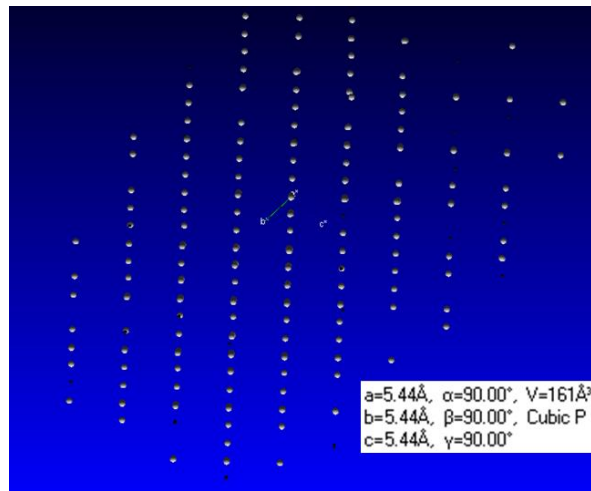
| No. | h | k | l | d [Å] | 2Theta[deg] | I [%] |
|-----|---|---|---|-------|-------------|-------|
| 1 | 1 | 1 | 1 | 3.13 | 28.44 | 100.0 |
| 2 | 2 | 2 | 0 | 1.92 | 47.30 | 55.0 |
| 3 | 3 | 1 | 1 | 1.63 | 56.12 | 30.0 |
| 4 | 4 | 0 | 0 | 1.35 | 69.13 | 6.0 |
| 5 | 3 | 3 | 1 | 1.24 | 76.38 | 11.0 |
| 6 | 4 | 2 | 2 | 1.10 | 88.02 | 12.0 |
| 7 | 5 | 1 | 1 | 1.04 | 94.95 | 6.0 |
| 8 | 4 | 4 | 0 | 0.96 | 106.71 | 3.0 |
| 9 | 5 | 3 | 1 | 0.91 | 114.09 | 7.0 |
| 10 | 6 | 2 | 0 | 0.85 | 127.54 | 8.0 |
| 11 | 5 | 3 | 3 | 0.82 | 136.89 | 3.0 |

Table 3.1: Intensity and peak position for silicon cubic phase structure (obtained from XRD data base).

Single-crystal XRD can also provide detailed information about the lattice structure and unit cell of the crystal. However in this case, due to the twin crystals in the structure, interpretation of data is difficult. The reflections in three-dimensional reciprocal space have been shown in Fig. 3.7. The reflections in reciprocal space can be related to the crystalline lattice in real space by an inverse Fourier transform. Using the Apex2 software program, the reflections are refined (Fig. 3.7 (b)) and lattice parameters are obtained as $a = 5.4234 \pm (0.0067) \text{ \AA}$ and $V = 159.52 \text{ \AA}^3$.



(a)



(b)

Figure 3.7: (a) Collected reflections in the three-dimensional reciprocal space. Each reflection represents diffraction from specific family of parallel planes in the crystal. (b) Using Apex2 software program, the data is refined and the lattice parameters are obtained.

3.4 Transmission electron microscopy study of silicon spheres

Transmission electron microscopy can provide direct images of morphology and crystallinity of the samples. Due to sample preparation difficulty, bright-field TEM study and transmission electron diffraction (TED) measurements can be performed only on a small portion of the sample, which has been thinned to a few tens of a nanometer. For TEM characterization studies, samples were prepared by the focused ion beam (FIB) technique. In order to minimize the FIB-induced damage and remove the introduced amorphous Si during sample preparation, the thinning process was completed by ion beam milling with energies less than 30eV. TEM observations were carried out using FEI Titan 80-300 microscope operating at an accelerating voltage of 300kV. Fig. 3.8 shows the result of TEM study of the sample prepared by the FIB method. The length of the prepared sample is about 20 μ m which is attached to a FIB grid. The bright-field TEM images taken from the sample showed the single crystal structure. The aperture size for TED measurements was about 300nm and diffraction patterns showed single crystal structure of silicon. TEM studies on the crystallinity of silicon spheres verify the result from x-ray diffraction analyses.

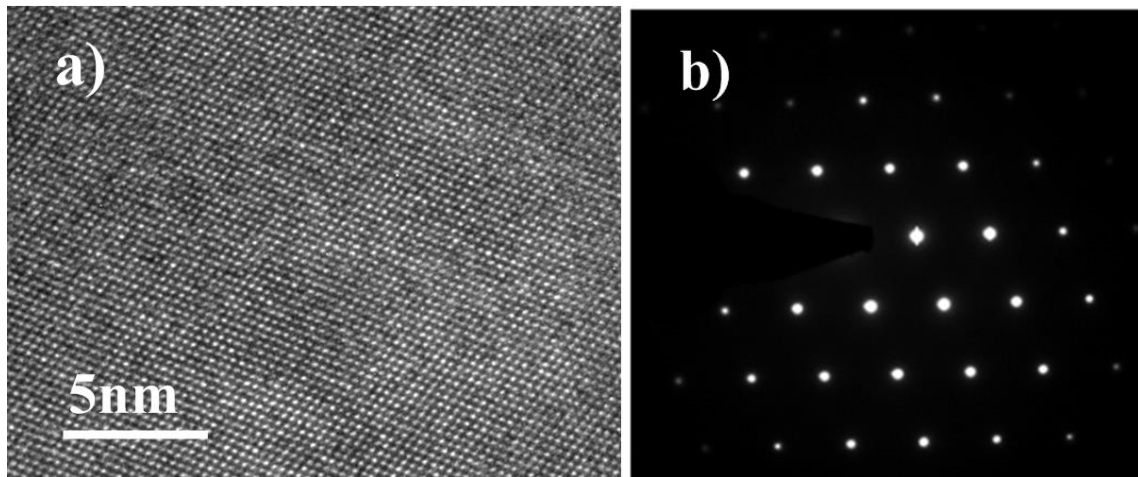


Figure 3.8: (a) Bright-field TEM image showing the silicon crystal structure. The FIB sample was prepared from the surface of the silicon spheres. (b) Selected area transmission electron diffraction pattern of samples showing perfect single crystal structure.

3.5 Secondary ion mass spectroscopy imaging of elemental distribution in the bulk of silicon spheres

Impurities in the bulk of silicon spheres can affect the electronic properties of material and also form point defects in the silicon crystal structure. Secondary ion mass spectroscopy (SIMS) is the most common technique to analyze the impurity levels in semiconductor and thin films. Detection limits of SIMS depends on the element and may vary from parts per billion to parts per million. In this technique, using a primary ion beam, species are ionized and sputtered from the surface of the sample. The ejected secondary ions are accelerated through a mass spectrometer to determine the elemental composition of the surface. This technique provides qualitative information about the elemental distribution in the samples; however, quantification is possible by use of standard samples. Previous SIMS depth profile studies on silicon spheres have shown high concentrations of Al and Co and low impurity levels of Cu, Fe, Cr, and Ti in the crystalline silicon structure.^{93, 94} In this section we focus on SIMS imaging of elemental distribution in the bulk of silicon spheres. In order to access the bulk of spheres for SIMS characterization, silicon spheres are embedded in a clear epoxy and polished to the mid-section (Fig. 3.9). For SIMS imaging, it is important to prepare samples with a smooth surface. Therefore, the polishing process started with sandpapers of different grit numbers and finished by using diamond paste with a particle size of less than 0.25 μm . Subsequently, for the removal of damage induced by the mechanical polishing, the surface of the silicon hemispheres was etched away in a solution of hydrofluoric and nitric acid.

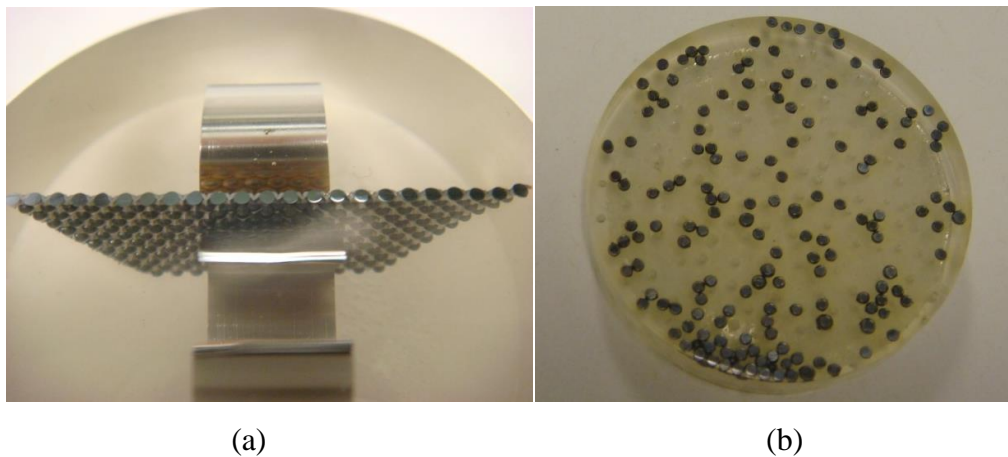


Figure 3.9: (a) Cross-sections prepared from silicon spheres embedded in a perforated aluminum foil (optical image). (b) Individual spheres are embedded in a clear epoxy and are polished to the mid-section, forming silicon hemispheres.

SIMS images of elemental distribution in negative mode were collected in Fig. 3.10. In order to obtain the surface scans, the focused primary ion beam is rastered across the sample and secondary ion intensities are recorded at each position. Prior to surface scans, the sputtering was carried out for 10min using a Cs ions beam on an area of $400 \times 400 \mu\text{m}^2$. Due to the angle of the Cs ion beam, a larger area was chosen to ensure the scanned area would be uniformly sputtered. As can be seen in this figure, microscopic defects can be observed in the elemental distribution map for carbon and oxygen.

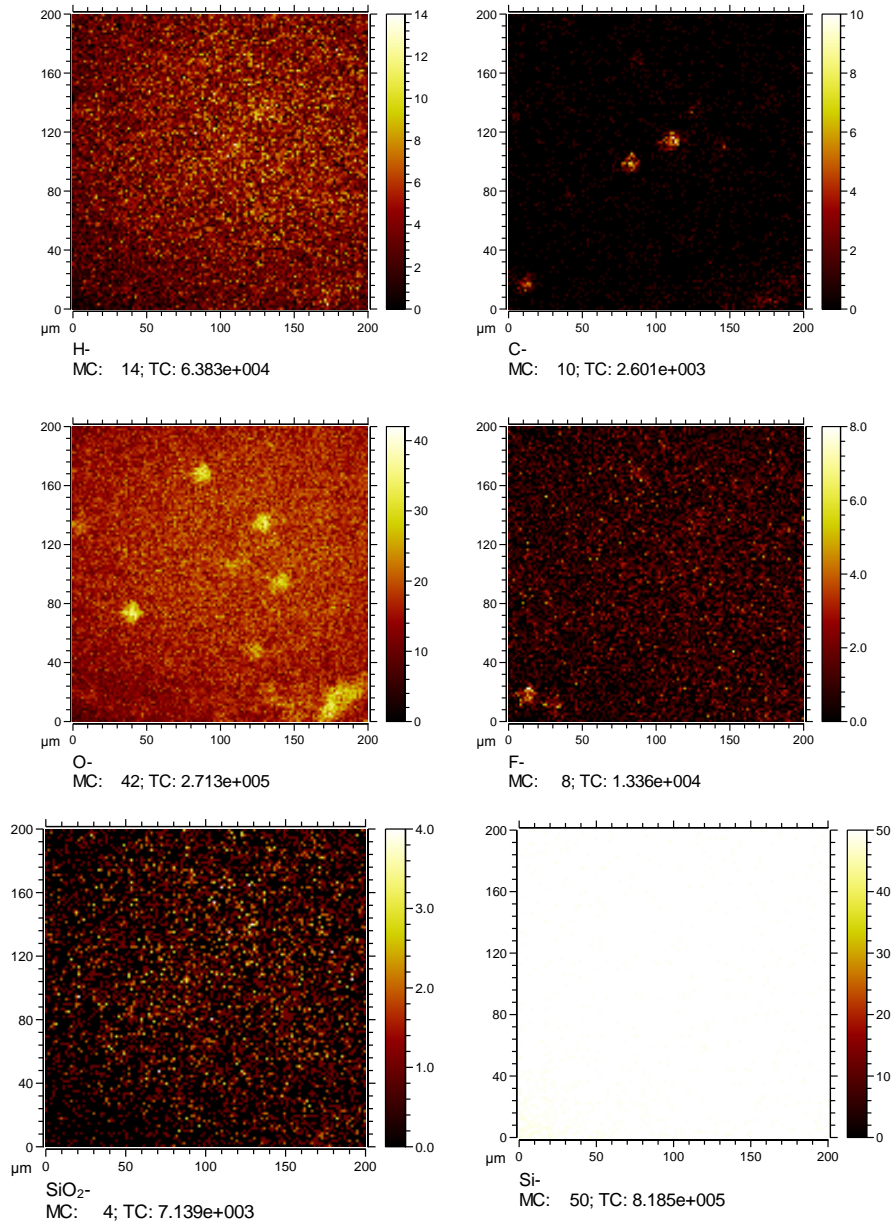


Figure 3.10: SIMS images obtained by scanning $200 \times 200 \mu\text{m}^2$ area of the polished surface of silicon spheres. The elemental distribution and total count (TC) for each element can be seen in this figure. Prior to surface scans, sputtering was carried out for 10 min using Cs ions beam on an area of $400 \times 400 \mu\text{m}^2$.

Due to the fabrication process of silicon spheres, a high concentration of oxygen exists in the bulk of silicon spheres and can act as a lifetime killer. Both interstitial and substitutional oxygen atoms create lattice imperfections and point defects in the crystalline structure of silicon. A high concentration of oxygen can also cause SiO₂ precipitation.⁹⁵ In order to investigate the elemental distribution at different depths, surface scans were obtained after different periods of sputtering time. Fig. 3.11 shows SIMS images from the same area after an extra 5mins of sputtering by a Cs ion beam.

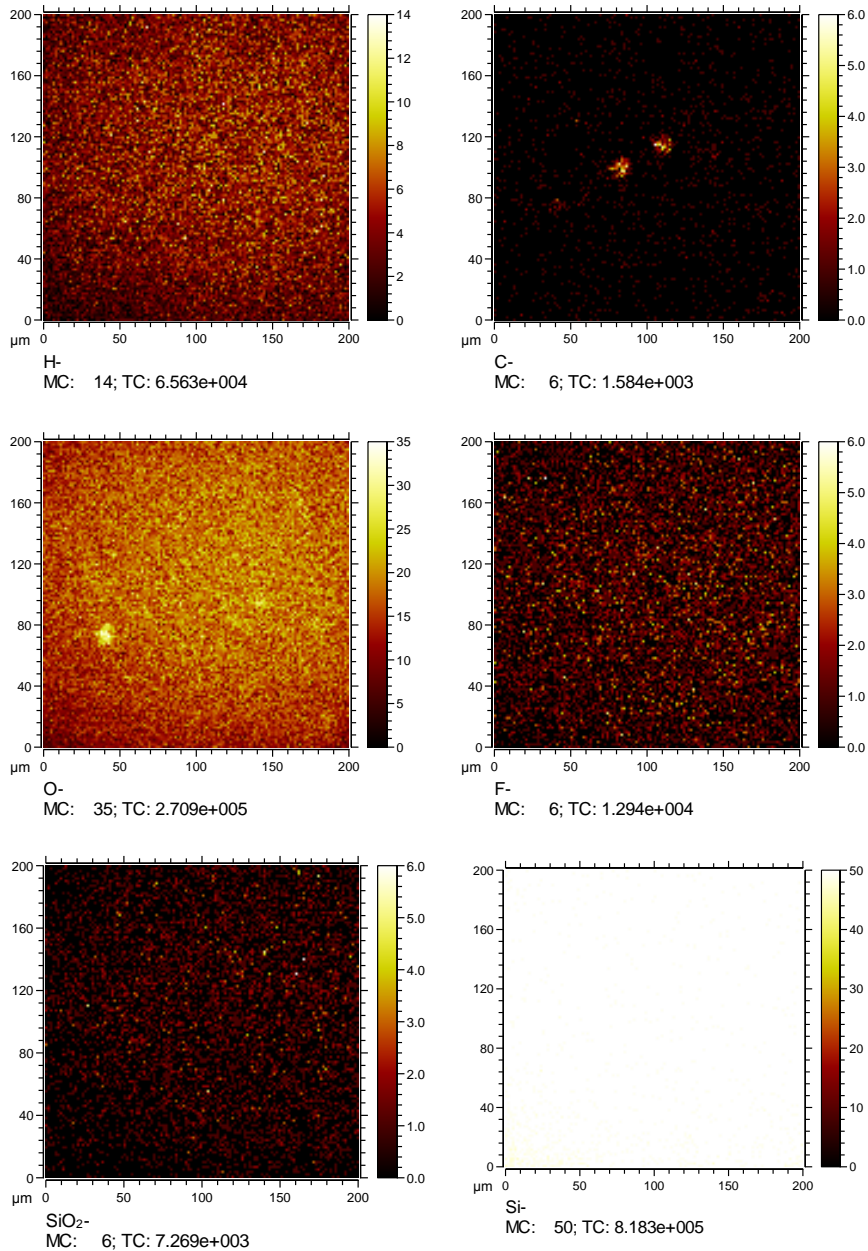


Figure 3.11: SIMS images obtained from the same area as in Fig. 3.9 after sputtering using a Cs ion beam for 15min (5min more).

As can be seen in this image the total count for carbon is decreased and less microscopic defects are observed in the elemental distribution map of oxygen.

3.6 Minority carrier lifetime in silicon spheres

Minority carrier lifetime measurements have been carried out using the microwave photoconductivity decay (μ -PCD) method. Photoconductivity decay is a common technique to measure the carrier recombination lifetime in silicon substrates. In this technique, a laser pulse is illuminated to the sample which results in the generation of excess carrier concentration in the bulk of the semiconductor. The decay of excess carrier concentration is monitored through microwave reflections from the surface of the semiconductor. For photoconductivity decay measurements, silicon spheres are embedded in a clear epoxy and are polished to the mid-section (Fig. 3.9(b)) to form silicon hemispheres. Since the measured carrier lifetime is affected by both bulk and surface properties, only when the surface recombination velocity (SRV) is significantly suppressed, the measured lifetime can be considered as the bulk lifetime. Therefore, the exposed surface of silicon hemispheres embedded in a clear epoxy is chemically passivated using diluted hydrofluoric acid solution (2% HF). The map of lifetime measurements from few spheres closely packed and embedded in the epoxy is shown in Fig. 3.12. Based on microwave reflection photoconductivity decay measurements, the average minority carrier lifetime in the silicon spheres varies from 0.2 to 1 μ s. However, higher minority carrier lifetimes can be obtained by using high quality silicon as a source material.

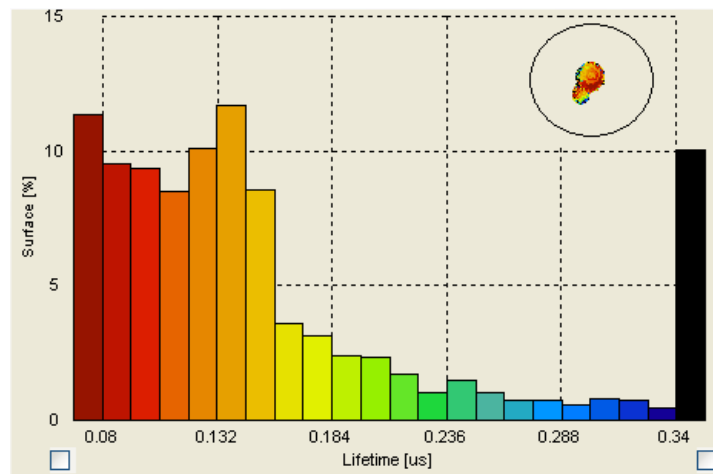


Figure 3.12: Microwave reflection photoconductivity decay measurements performed on a few silicon spheres closely packed and embedded in a clear epoxy. The inset shows the lifetime map.

3.6 Conclusion

The material properties of silicon spheres included surface morphology, crystallinity, lattice structure, microwave photoconductivity decay lifetime, and impurity elemental distributions were studied. SEM images obtained from the surface of silicon spheres revealed microscopic defects on the surface of crystalline silicon spheres. Due to the higher rate of etching, these defects can be formed on the surface of crystalline spheres during chemical etching processes. These defects may originate from impurity sites such as oxygen or lattice defects in the crystalline structure of spheres. Crystallinity of silicon spheres was investigated by means of a single-crystal x-ray diffractometer and an x-ray powder diffraction machine. Most of the x-ray diffraction patterns collected by the x-ray powder diffraction (XRD) method only revealed one peak or no peaks were observed in the x-ray diffraction pattern. This indicates silicon spheres do not contain polycrystalline silicon and the structure is single-crystal or multi-crystal. However, 2D diffraction patterns obtained by Single-crystal XRD method illustrate twin-crystal reflections from silicon spheres. TEM studies on the crystallinity of silicon spheres verify the result from x-ray diffraction analyses. Elemental distribution was studied using SIMS imaging technique. Microscopic defects were observed in the elemental distribution map for carbon and oxygen. High concentration of oxygen is expected in the bulk of silicon spheres as they undergo sequential melting and re-crystallization steps to achieve high crystalline quality. High concentration of oxygen can act as a lifetime killer, create lattice imperfections, or cause SiO₂ precipitation. Photoconductivity decay technique was used to obtain the carrier recombination lifetime in silicon spheres. Based on microwave reflection photoconductivity decay measurements, the average minority carrier life time in the silicon spheres varies from 0.2 to 1 μ s.

Chapter 4

Baseline fabrication process and fabrication of new designs with integration of novel nanostructures into silicon spheres

4.1 Introduction

Spherical solar cells are based on embedment of silicon spheres of about 1mm size into a flexible aluminum foil. The spheres used in this research are produced by spheroidization of molten silicon. This technique was initially developed by Texas Instruments (TI). In this technique, using a high power arc lamp, a small amount of silicon powder is optically fused and melted to form spherical shape of about 1mm in size. Powder silicon can be obtained from various sources with different quality levels, such as kerf loss from wafer cutting which has a higher quality and metallurgical grade silicon which has a lower quality level. This process including the melting and solidification is done in a very short time. Therefore, the spheres obtained initially are not single crystal and they are expected to have more of a poly-crystalline structure. Further annealing process at high temperatures (above 1400°C) is performed to obtain a higher crystalline quality and elevated impurity levels. Prior to each annealing process, spheres are covered with a layer of thermal oxide and this layer of oxide prevents the spheres from sticking

together. During the annealing process and recrystallization, impurities are moving toward the surface oxide layer and are segregated at the surface of the spheres. This oxide layer, along with segregated impurities is etched away using a chemical etching process. Subsequently, the emitter is formed all over the sphere surface using a high temperature (above 900°C) diffusion step from an infinite phosphorus doping source. This chapter deals with the fabrication process of spherical silicon solar cells. The emitter diffusion process, embedment of sphere in an aluminum foil and realization of back aluminum contact are explained. The silicon spheres used in this research are produced by ATS solar cell company. Each sphere was p-type in the bulk with a uniformly diffused emitter over the surface.

In this Chapter, we explain the baseline fabrication process of silicon spheres and present the fabrication process of new designs with the integration of nanostructures into silicon spheres. These new device structures include: spherical silicon solar cell integrated with nanostructured porous layers, sphere silicon solar cells with hemispherical nanopit texturing, and cells integrated with colloidal quantum dots.

4.1 Baseline fabrication process

A 3D schematic of silicon spheres with diffused emitter is illustrated in Fig. 4.1. Silicon spheres are embedded and thermally bonded to an aluminum foil. The back and front contacts to silicon spheres as well as the insulator layer can be seen in this figure. Fig. 4.2 shows the 2D schematic of the spherical silicon solar cells. Each sphere is p-type in the bulk with n-type diffusion over



Figure 4.1: 3D schematic of a silicon sphere with diffused emitter thermally bonded to aluminum foil.

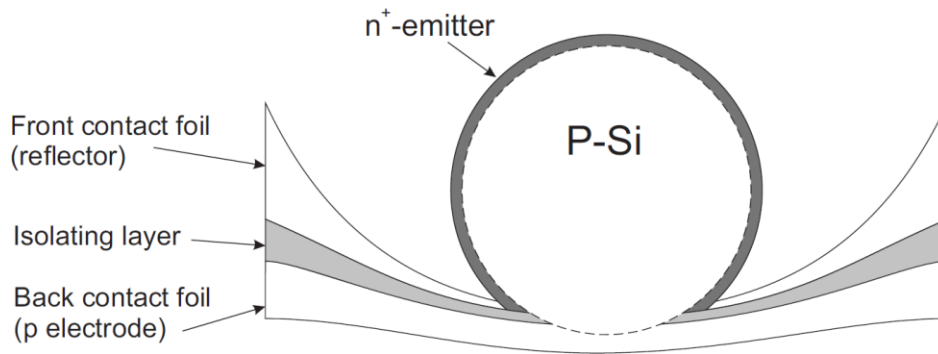


Figure 4.2: Schematic of spherical silicon solar cells.

the surface. The emitter is formed all over the sphere surface using a high temperature (above 900°C) diffusion step from an infinite phosphorus doping source. After junction formation, the silicon spheres are pressed and thermally bonded into an aluminum (Al) foil. The bonding process is performed by a thermo-mechanical process at a temperature around 500°C. Once the contact to the emitter (cathode) is formed, the n^+ layer from the portion of the sphere below the aluminum foil bonding is chemically etched away to expose the p-type bulk for base (anode) contact. In order to provide a contact to the p-type sphere, a thin layer of polyimide as an insulating layer has been deposited to separate the front and the back foil. Finally, the back aluminum foil is bonded to the spheres to create the p-contact. However, ohmic contacts can also be applied to p-type silicon spheres by using e-beam deposition technique.

Fig. 4.3 shows the SEM image of Si spheres with a diameter of about 700 μ m embedded and thermally bonded into an aluminum foil. The hexagonal-shape reflector used as the n-electrode significantly reduces the dead area (off silicon) among the spheres.

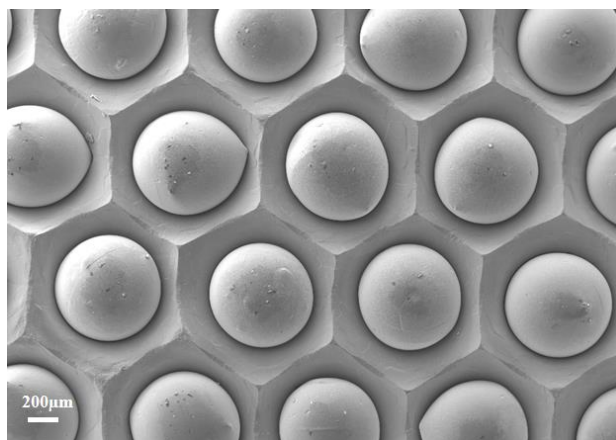


Figure 4.3: SEM image of the crystalline Si spheres with a diameter of about 700 μ m embedded and thermally bonded into an aluminum foil.

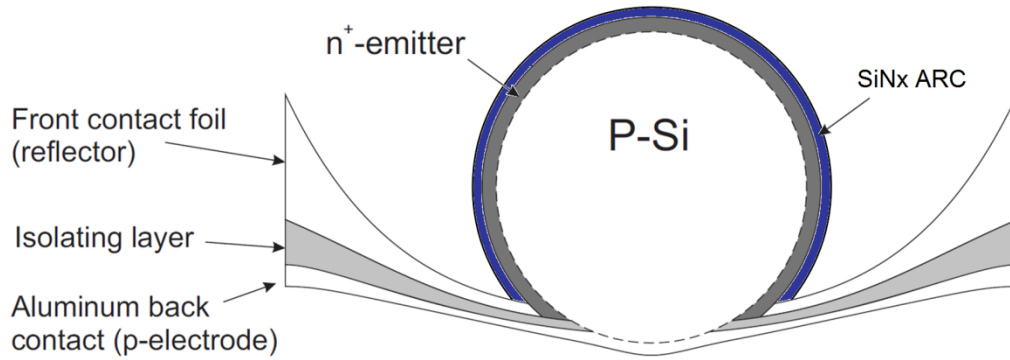


Figure 4.4: Spherical silicon solar cells with PECVD SiN_x layers. Silicon nitride passivation/ARC layers have been developed and deposited onto spherical silicon solar cells. Furthermore, a low temperature hydrogenation plasma technique was developed to improve the passivation quality of spherical silicon solar cells.

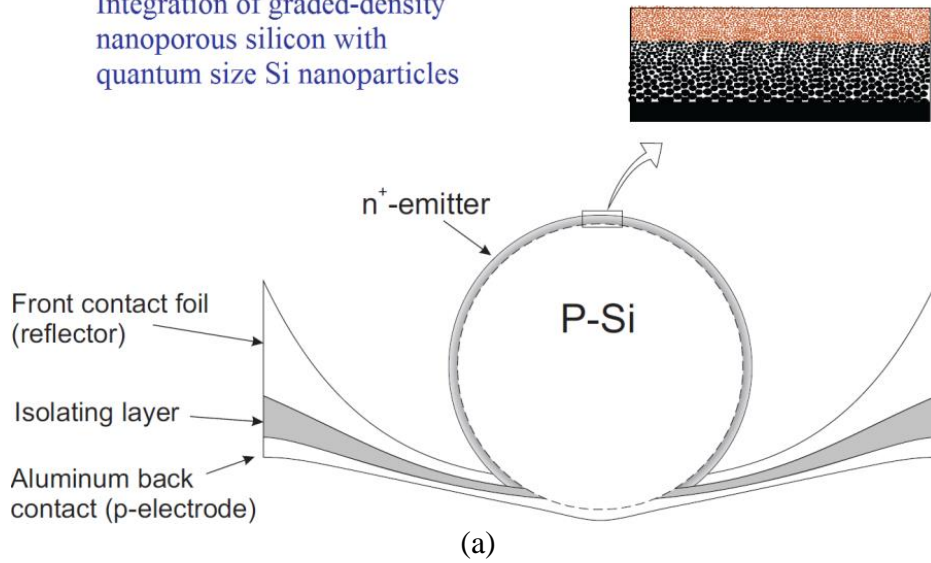
4.2 Development of SiN_x passivation/ARC layers for silicon spheres (chapter 5)

A schematic of spherical silicon solar cells with silicon nitride antireflection coating layer has been shown in Fig. 4.4. Silicon nitride antireflection coating layers were deposited onto spherical silicon solar cells, using Oxford Plasmalab PECVD system. By control of the plasma condition (gas flow ratio, power and pressure) silicon nitride layers were optimized. Furthermore, a low temperature hydrogenation plasma technique was developed to improve the passivation quality of spherical silicon solar cells. The spectral response of silicon spheres with and without silicon nitride antireflection coating has been studied.

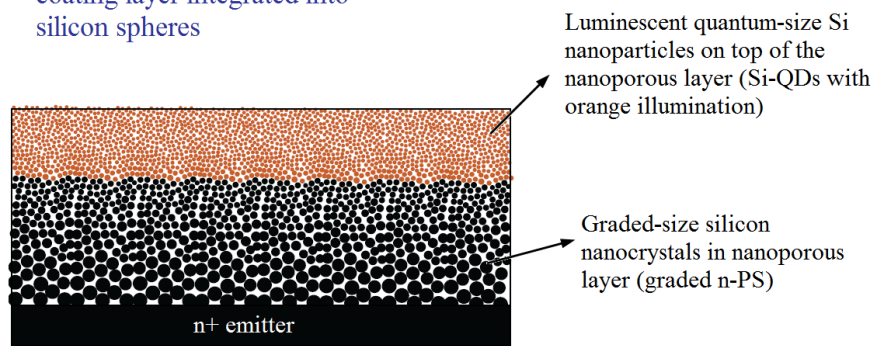
4.3 Integration of a graded-density nanoporous Si layer with quantum-size Si nanoparticles (Chapter 6)

Fig. 4.5 shows the schematic of silicon spheres with integrated graded-density nanoporous Si layer. This layer consists of graded-size silicon nanocrystals and Si quantum dots embedded in an oxide matrix. After the baseline fabrication process, using an electrochemical etching technique, nano-PS layers were successfully formed on the silicon spheres. The anodization process was performed in a conventional single tank Teflon cell under ambient light. A platinum grid was used as the cathode and a mixture of HF and ethanol was prepared as the electrolyte solution.

Integration of graded-density nanoporous silicon with quantum size Si nanoparticles



Nanostuctured antireflection coating layer integrated into silicon spheres



(b)

Figure 4.5: (a) Schematic of spherical silicon solar cells with integrated graded-density nanoporous Si layer. (b) This layer consists of graded-size silicon nanocrystals and Si quantum dots embedded in an oxide matrix.

The samples were mounted by screw pressure at the bottom of a Teflon cell with an opening of about 2-inch diameter. The applied current to the spherical solar cells is varied 0.5 to 2A. The current density was kept constant during the etching process to have better control of thickness and structure of the PS layer as well as reproducibility of the process. The anodizations were performed at room temperature with a constant current for the periods of less than 60 seconds.

4.4 Integration of hemispherical nanopit texturing into silicon spheres (Chapter 7)

A conventional single tank system was used for the electrochemical etching process. In order to obtain the hemispherical nanopit texturing, silicon spheres electrochemically etched in a solution of hydrofluorosilicic (Fig. 4.6). A platinum grid was used as the cathode and a mixture of diluted H_2SiF_6 (35% with H_2O) and ethanol was prepared as the electrolyte solution. The samples were mounted by screw pressure at the bottom of Teflon cell with an opening of 2-inch diameter. A constant current of 550 mA was imposed in the anodization tank and the forming voltage during the anodization process was 3.5 V. However, the voltage slowly increased during the anodization process due to the silicon texturing and changes at the surface of silicon. The schematic of silicon spheres with hemispherical nanopit texturing on the emitter is shown in Fig. 4.7. As can be seen in this Figure, nano-texturing of silicon spheres with a diffused emitter results in a selective emitter solar cell.

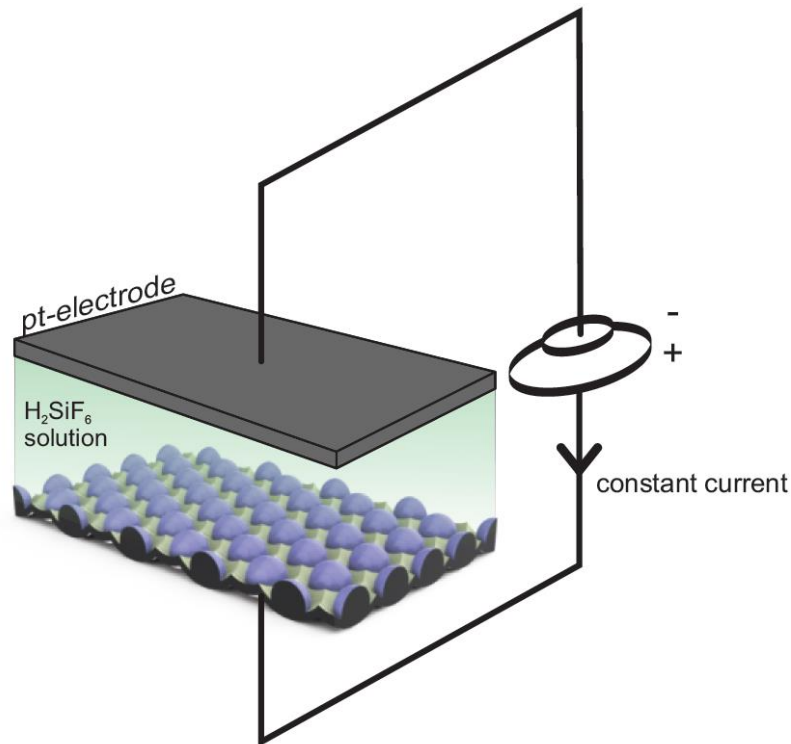


Figure 4.6: In order to obtain the hemispherical nanopit texturing, silicon spheres electrochemically etched in a solution of hydrofluorosilicic acid under constant current.

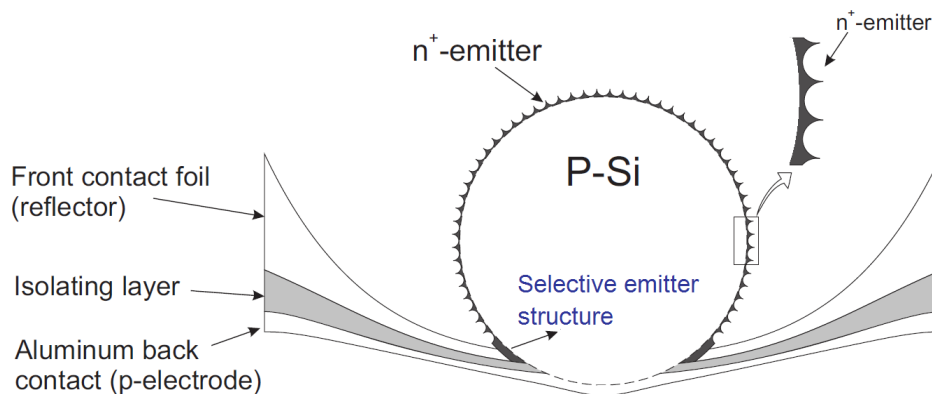


Figure 4.7: Schematic of silicon spheres with hemispherical nanopit texturing on the emitter. Nanotexturing of silicon spheres with a diffused emitter results in selective emitter solar cells.

4.4 Integration of colloidal CdSe-QDs into silicon spheres (Chapter 8)

We have successfully fabricated a QDs-embedded layer by processing colloidal QDs into a graded-density nanoporous silicon layer (Fig. 4.8). The proper concentration of CdSe quantum dots in toluene solution was prepared and spherical silicon solar cells with a nanoporous layer were immersed in the solution using an ultrasonic system. The CdSe quantum dots are dispersed in the pores of the nanoporous Si structure. Subsequently, the cell is washed with toluene solution to remove the CdSe quantum dots precipitated on the surface of the nanoporous layer. The spectral response of spherical silicon solar cells with and without CdS-QDs incorporation was studied.

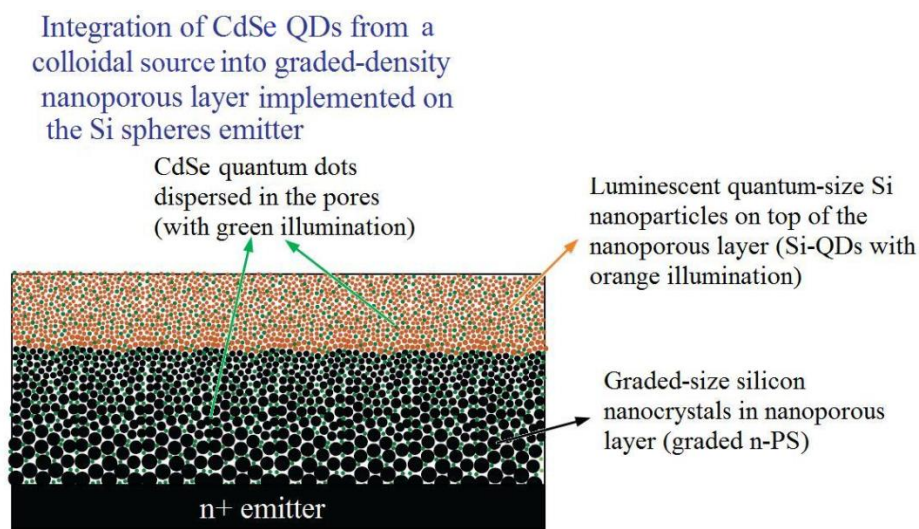


Figure 4.8: Incorporation of colloidal QDs into graded-density nanoporous layer.

Chapter 5

Development of SiN_x passivation/ARC layers for spherical solar cells

5.1 Introduction

Optimization of the optical losses of spherical silicon solar cells is one of the most important techniques to improve the short-circuit current density and hence the efficiency of the cells. Deposition of antireflection coating (ARC) layers and texturing of the silicon surface are the most common methods to improve the optical losses of silicon solar cells. Single layer ARCs such as ZnO, ITO, SiO_x, and SiN based on a destructive interference of reflected waves minimize the reflection at one single wavelength (λ_{min}). Single ARC layers can reduce the overall reflectivity of the crystalline silicon to less than 10%. However, using multilayer coatings can further reduce the reflection in a wider spectral range; however, this increases the cost and adds additional steps.⁹⁶

Dark-blue silicon nitride layers deposited by a plasma-enhanced chemical vapor deposition (PECVD) method have been widely used as an industrial process to improve the reflectivity of silicon solar cells. However, due to the shape of silicon spheres and their embedment in aluminum foil, the deposition process is different to flat silicon wafers.

In this short Chapter, we optimize PECVD deposited silicon nitride layers to obtain dark-blue SiN_x coated spheres. Furthermore, a low temperature hydrogenation plasma technique was developed to improve the passivation quality of spherical silicon solar cells. The spectral response of silicon spheres with and without silicon nitride antireflection coating is studied.

5.2 Experimental results

Silicon nitride layers were deposited using Oxford Plasmalab 80 Plus PECVD system. In order to optimize the SiN_x layers, they were initially deposited onto glass and flat silicon substrates. The reflection and transmission spectra of the SiN_x films were obtained and the optical constants were extracted using PUMA software program. The optimized SiN_x layer exhibited different properties once deposited onto spherical silicon solar cells. This is attributed to the shape of silicon spheres and aluminum foil, changing the plasma condition at the surface of the silicon spheres and hence producing different SiN_x layers. It was observed the working pressure and the size of the sample (edge effect) significantly affect the properties of deposited layer. Optical images of silicon solar cells obtained by two different process conditions are shown in Fig. 5.1. The process conditions for each sample are summarized in Table 5.1.

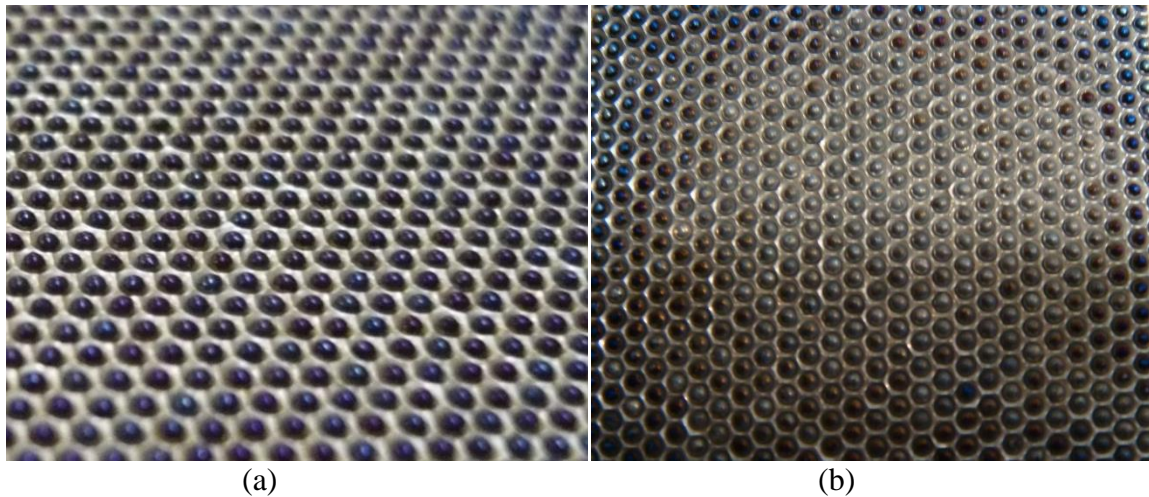


Figure 5.1: PECVD deposited SiN_x layers obtained at different plasma conditions. (a) at pressure of 0.6 Torr, and (b) at pressure of 0.2 Torr. As can be seen in this image, dark-blue SiN_x-coated spheres were obtained at higher pressures. However, at both process conditions, blue color SiN_x layers were obtained on flat silicon wafers.

| Sample | Pressure (mTorr) | Temperature (°C) | Power (W) | SiH ₄ (sccm) | NH ₃ (sccm) |
|------------|------------------|------------------|-----------|-------------------------|------------------------|
| Sample (a) | 600 | 280 | 25 | 20 | 30 |
| Sample (b) | 200 | 280 | 21 | 10 | 20 |

Table 5.1: Process condition for PECVD nitride deposition

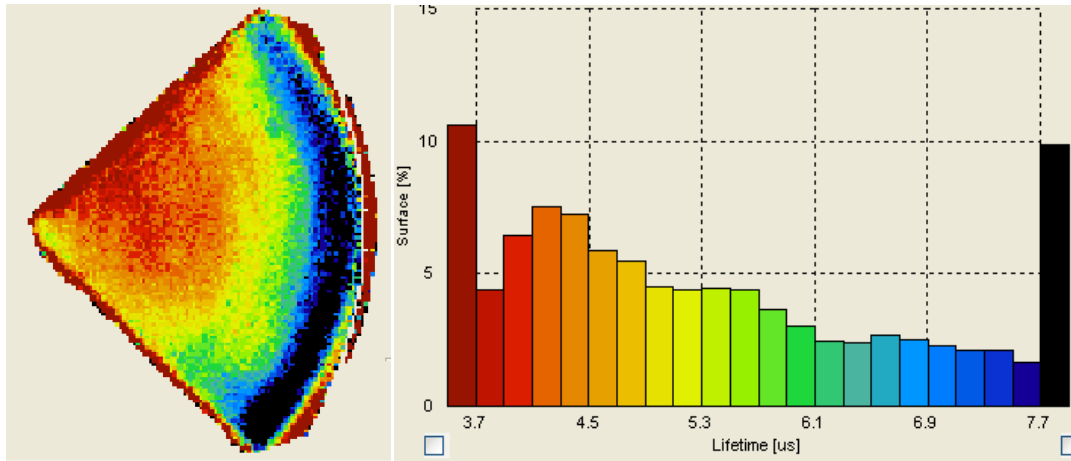
These layers were first optimized on the silicon wafers to obtain a high quality uniform SiN_x layer with refractive index of about 1.95 and subsequently were deposited onto the silicon spheres. As can be seen in this image, dark-blue SiN_x-coated spheres were obtained at the working pressure of about 0.6 Torr (Fig. 5.1(a)). While, non-uniform deposition of silicon nitride layers were observed at lower pressures. Fig. 5.1(b) shows the sample coated with a silicon nitride layer at working pressure of 0.2 Torr. Light-blue spheres can be observed at the edge of the sample and poor deposition of SiN_x was observed in the centre.

5.3 Development of a hydrogenation plasma process to improve the surface passivation quality

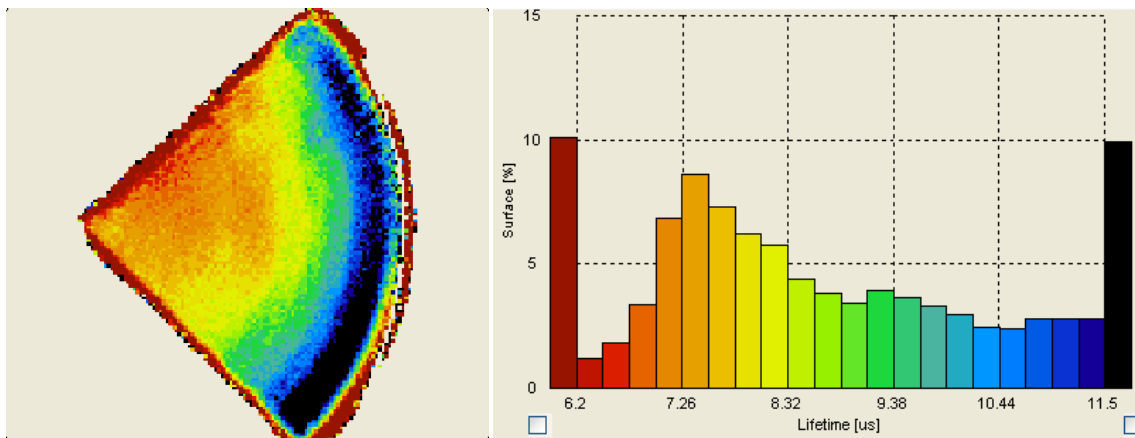
Silicon nitride layers can also be used as an efficient surface passivation layer to improve the surface recombination velocity and therefore, minority carrier lifetime in silicon solar cells. In general, high quality silicon nitride layers are deposited at temperatures of about 400°C. However, since in the fabrication process of the spherical silicon solar cells insulating polyamide layers as well as aluminum bonding have been used, the deposition process temperature should be kept below 300°C. In order to improve the passivation quality of the silicon nitride layers we have developed a hydrogenation plasma process at a low temperature of 175°C. The process condition for the hydrogenation plasma treatment is summarized in Table 5.2. In order to study the passivation quality improvement, silicon nitride layers were deposited on the both sides of a p-type silicon wafer and photoconductivity decay measurements were performed. Based on microwave reflection measurements, the average minority carrier lifetime of about 5.5 μ s was obtained (Fig. 5.2(a)).

| time | Pressure (mTorr) | Temperature (°C) | Power (W) | H ₂ (sccm) |
|--------|------------------|------------------|-----------|-----------------------|
| 15 min | 200 | 175 | 120W | 100 |

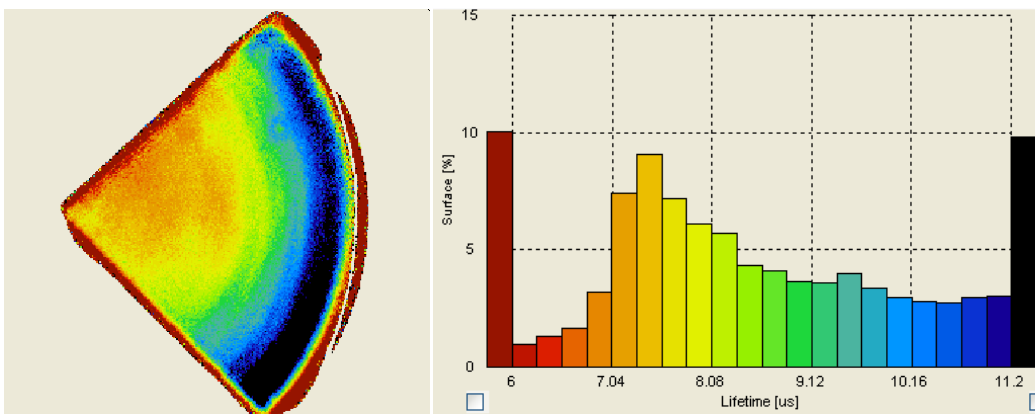
Table 5.2: Process condition for Hydrogenation plasma



(a)



(b)



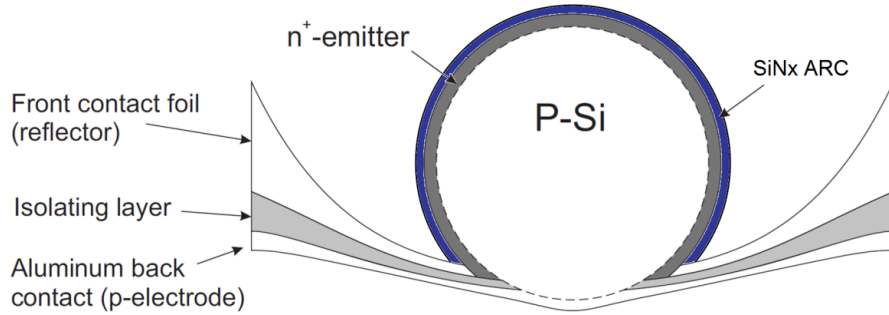


Figure 5.3: Spherical silicon solar cells with PECVD SiN_x layer. Silicon nitride passivation/ARC layers have been developed and deposited onto spherical silicon solar cells. Furthermore, a low temperature hydrogenation plasma technique was developed to improve the passivation quality of spherical silicon solar cells.

Subsequently, the sample was placed in the Oxford PECVD system and the hydrogenation plasma treatment, based on the process condition in Table 5.2, was performed. The photoconductivity decay measurements revealed significant improvement in the minority carrier lifetime. Fig. 5.2(b) shows the lifetime map of the sample after the hydrogenation plasma process. In order to study the stability properties of the passivation layer, the photoconductivity measurements were repeated after 20h resulting in the same minority carrier lifetime. Fig. 5.2(c) illustrates the lifetime map after 20h. Since at low temperatures, less than 300°C , hydrogen diffusion to the bulk of silicon is low, the lifetime improvement is attributed to the improvement of surface quality passivation.²²

5.4 Reflectance and spectral response of spherical solar cells with SiN_x ARC layer

The schematic of spherical silicon solar cells with silicon nitride antireflection coating layer is shown in Fig. 5.3. Reflection measurements of spherical silicon solar cells were carried out using a UV/Vis spectrophotometer equipped with the integrated sphere. Reflectance spectra of the spherical silicon solar cells are depicted in Fig. 5.4. Single layer ARCs based on a destructive interference of reflected waves, minimize the reflection at one single wavelength. Due to the dark-blue color of the silicon spheres, the minimum of the reflectance spectra is expected to be at higher wavelengths. This is attributed to the effect of silicon nitride layers deposited over aluminum foil. Since aluminum foil is a reflector for silicon spheres, this is not favorable.

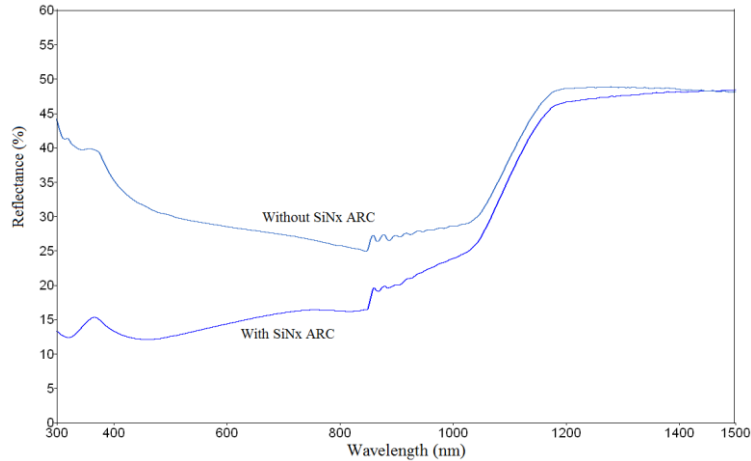


Figure 5.4: Reflectance characteristics of spherical silicon solar with and without SiNx antireflection coating layer.

The selective removal of silicon nitride layer from aluminum foil is difficult; therefore, this counts as a drawback for PECVD silicon nitride layers. In the next Chapter we investigate the integration of the graded-density n-PS layer which is selectively formed over silicon spheres and can suppress the reflectivity in a wide range of spectral response.

External quantum efficiency spectra of silicon spheres with and without SiNx layer are collected in Fig. 5.5. Due to the improvement of optical losses, spectral response of silicon spheres with SiNx layer showed significant improvement. Furthermore, silicon nitride layers improve the passivation quality of the spherical solar cells resulting in the enhancement of the spectral response in lower wavelengths. The latter is more noticeable in solar cells with shallow emitter structures.

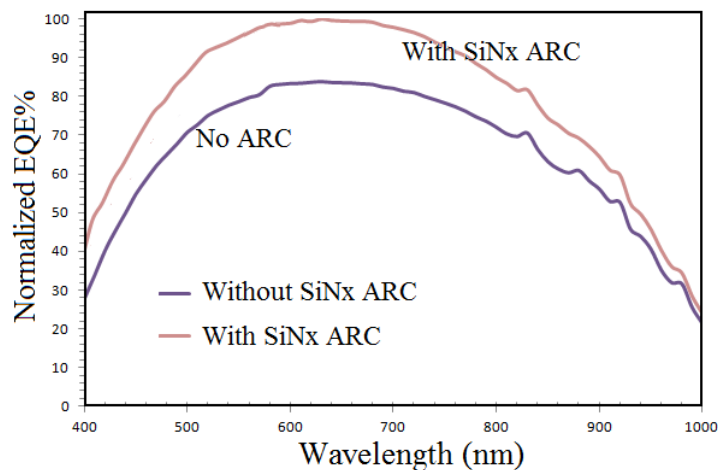


Figure 5.5: Spectral response measurements of spherical silicon solar cell with and without SiNx antireflection coating layer.

5.5 Conclusion

Silicon nitride antireflection coating layers were deposited onto the spherical silicon solar cells, using a PECVD system. By control of the plasma condition (gas flow ratio, power and pressure) dark-blue SiN_x coated spheres were obtained. However, silicon nitride layers developed at low pressures on silicon wafers, exhibited poor uniformity and a low deposition rate once deposited onto silicon spheres. Furthermore, a low temperature hydrogenation plasma technique was developed to improve the passivation quality of spherical silicon solar cells. The spectral response of silicon spheres with and without the silicon nitride antireflection coating has been studied.

Chapter 6

Integration of a graded-density nanoporous Si layer with quantum-size Si nanoparticles

6.1 Introduction

Since the discovery of visible luminescence from porous Si,³¹ it has been widely studied by many researchers resulting in the publication of various extended review articles and books. However, in spite of extensive studies, the mechanisms of the etching process as well as parameters involved in the chemical reactions are still not fully understood. Under controlled conditions, porous silicon layers consist of disordered micro-pores and network of silicon interconnections can be formed.³²⁻³⁴ Nanoporous layers with quantum confinement effects can show properties such as enhanced luminescence, light trapping, and photon shifting (light transformation from ultraviolet to longer wavelengths).³³⁻³⁹ It has therefore been a potential candidate for applications in optoelectronics, micro-electronics and photonics.^{38,42,43} It is well known that porous Si layers can be successfully used as an effective antireflection coating (ARC) in crystalline silicon solar cells.⁴⁴⁻⁴⁶

Black silicon has been proposed as a potential candidate to replace conventional antireflection coatings based on interference in silicon solar cells. Single layer ARCs such as ZnO, ITO, SiO_x,

and Si_3N_4 based on a destructive interference of reflected waves minimize the reflection at one single wavelength (λ_{min}). For photovoltaic applications, this λ_{min} is optimized to lie in the range of 650 to 700nm, which corresponds to the peak of energy in the solar spectrum. Although using multilayer coatings can further reduce the reflection in a wider spectral range, it increases the cost and adds additional steps.

Optimization of the optical losses of spherical silicon solar cells is one of the most important techniques to improve the short-circuit current density and hence the efficiency of the cells. As it was addressed in the previous chapter, conventional deposition methods cannot easily be applied to make a uniform ARC layer on spherical silicon solar cells. In contrast, growth of a graded-density porous Si (PS) layer is a single-step, low cost, high performance and fast process (less than 60s). Integration of this graded-density nanoporous Si layer with quantum-size Si nanoparticles not only provides a black silicon solar cell but also due to the quantum confinement effects and band gap opening, the light absorption in the emitter layer is reduced.

In this Chapter, we study the characterization of graded-density nanoporous layer with a Si-QDs embedded layer. This layer has been characterized by the means of scanning electron microscopy (SEM), transmission electron microscopy (TEM), Scanning TEM, energy filtered TEM, dark-field TEM, transmission electron diffraction (TED), electron energy loss spectroscopy (EELS), energy dispersive x-ray (EDX), Raman spectroscopy and photoluminescence spectroscopy (PL). Furthermore, we successfully integrated this layer into silicon spheres, and the solar cell characteristics were studied.

6.2 Experimental details

Using an electrochemical etching technique as a post-processing step, nano-PS layers have been successfully formed on the silicon spheres. The anodization process was performed in a conventional single tank Teflon cell for electrochemical etching (Fig. 6.1). A platinum grid was used as the cathode and a mixture of HF and ethanol was prepared as the electrolyte solution. The samples were mounted by screw pressure at the bottom of the Teflon cell with an

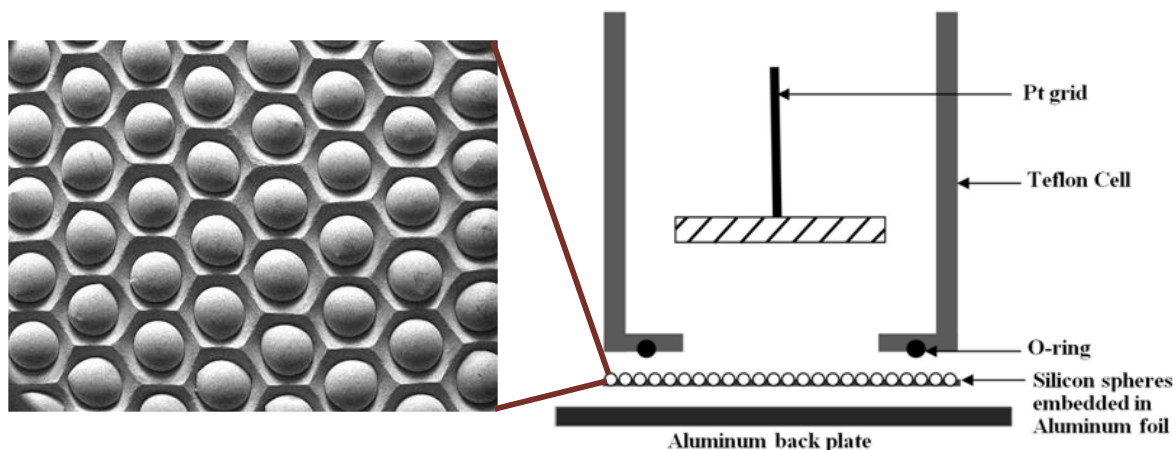


Figure 6.1: Cross-sectional view of the single-tank anodization cell used for PS coating of silicon spheres.

opening of about 2-inch diameter. The applied current to the spherical solar was varied from 0.5 to 2A. The current density was kept constant during the etching process to have better control of thickness and structure of the PS layer as well as reproducibility of the process. The anodizations were performed at room temperature with a constant current for the periods of less than 60 seconds under ambient light.

6.3 Scanning electron microscopy: Surface morphology of the graded-density nanoporous layer

Fig. 6.2 shows the SEM image of the microstructure of the PS layer formed on silicon spheres. Fig 6.2(b) and (c) show the surface morphology of the porous layer on the top and side of the sphere indicating the formation of a uniform layer around the Si sphere. Homogenously distributed pores with the same nanostructure and very fine interconnections can be observed on the top and sides of spheres. The magnified image (Fig. 6.2(d)) illustrates the distribution of the micropores and Si interconnections with a size of less than 5nm. Obtaining high quality HRSEM images from the surface of microporous silicon is not easy as the conductivity is low plus the oxidation of the surface in the ambient atmosphere would make it even more difficult. Formation of macro- or micropores in porous silicon strongly depends on the anodization current, type of silicon and doping density (heavily or lightly doped). The applied current for the porous layer in this image was 0.55A and not a significant change in the morphology of the nanoporous layer was observed by increasing the current. However, it was noticed that obtaining a clear SEM image from samples prepared with higher anodization current is more difficult. This can be attributed to the formation of a thicker nanoporous layer with quantum size nanoparticles

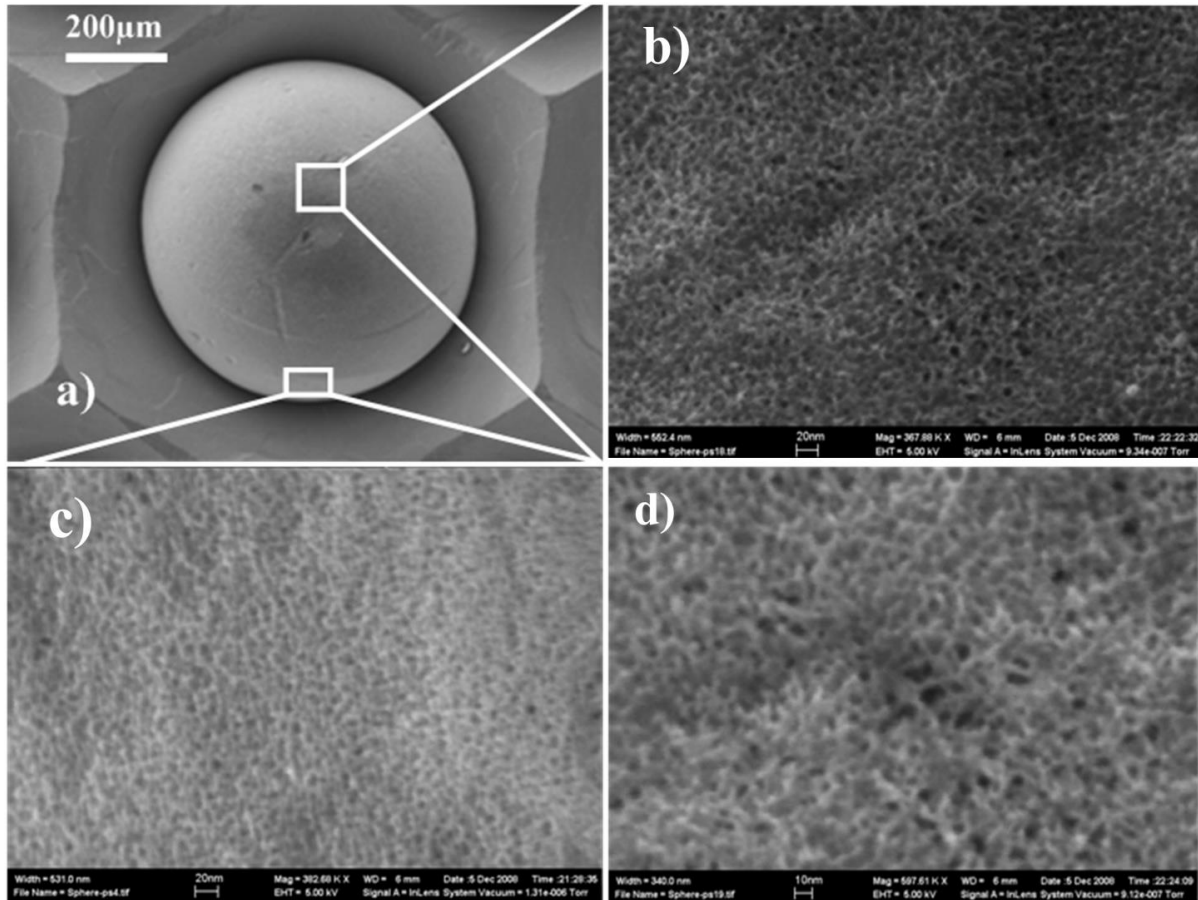


Figure 6.2: a) SEM image of a single crystalline Si sphere embedded into a perforated aluminum foil. b) SEM micrograph of PS layer formed on crystalline silicon spheres. c) SEM image taken from side of sphere, showing uniform formation of porous layer around the sphere. d) HR-SEM image magnified from image (b) showing distribution of micro-pores with silicon interconnections of less than 5nm in width.

at higher currents. Due to the oxidation of the samples in ambient atmosphere, these quantum size nanoparticles ($<3\text{nm}$) are embedded in an oxide matrix which has poor conductivity.

Fig. 6.3 shows the porous layer formed with an applied current of 0.7A. The morphology and nanostructure of the porous layer including the pore diameters and the size of nanocrystals are related to the depletion layer and the charge transfer mechanism. In n^+ Si wafers, charge transfer is dominated by tunneling and therefore, the size of the pores is determined by the width of the depletion region which is typically around 5-10nm. While, PS layers formed on p-type Si contain very small pores less than 5nm with uniform branching and interconnections.

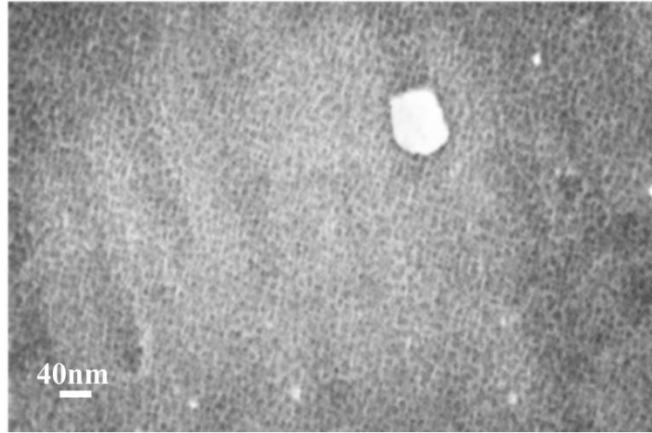


Figure 6.3: SEM micrograph of PS layers formed on silicon spheres with an applied current of 0.7A.

6.4 Cross-sectional TEM study of graded-density n-PS layer

Cross-sectional TEM observations (bright-field) were carried out using FEI Titan 80-300 microscope operating at an accelerating voltage of 300kV, and Dark-field TEM images were obtained by JOEL 2010F at 200kV. Sample preparation for the TEM study was performed using a focused ion beam (FIB) technique. In order to minimize the FIB-induced damage and remove the introduced amorphous Si during sample preparation, the thinning process was completed by ion bombardment having energies down to 30eV. Fig. 6.4(a) shows the bright-field TEM image of the graded-density porous layer obtained with an anodization current of 0.55A. The microstructure of the PS layer is composed of a network of silicon nanocrystals and interconnections of less than 10nm at the silicon interface which gradually decreases toward the air/film interface. The size of these nano-crystallites at the surface of the porous layer is less than 2nm. The PS layer with graded-size nanocrystals results in a graded-index PS layer on top of the emitter layer which can efficiently suppress the reflectivity in a broad spectral range. Fig. 6.4(b) shows the dark-field TEM cross-sectional image of the PS layer formed on the diffused emitter of single-crystal spheres. The changes in the nanocrystalline structure of the PS layer can be observed more clearly in the dark-field TEM imaging demonstrating the graded-density structure of the PS layer. The substrate has been used for beam alignment along [220] direction and bright reflections represents diffracting nanocrystallites. Random branching of pores starts from silicon interface and the feature sizes becomes smaller by moving toward the surface. Fig. 6.4(c) shows the cross-section, TEM image of the Si/PS interface illustrating a smooth transition between Si and the PS layer forming a uniform interface.

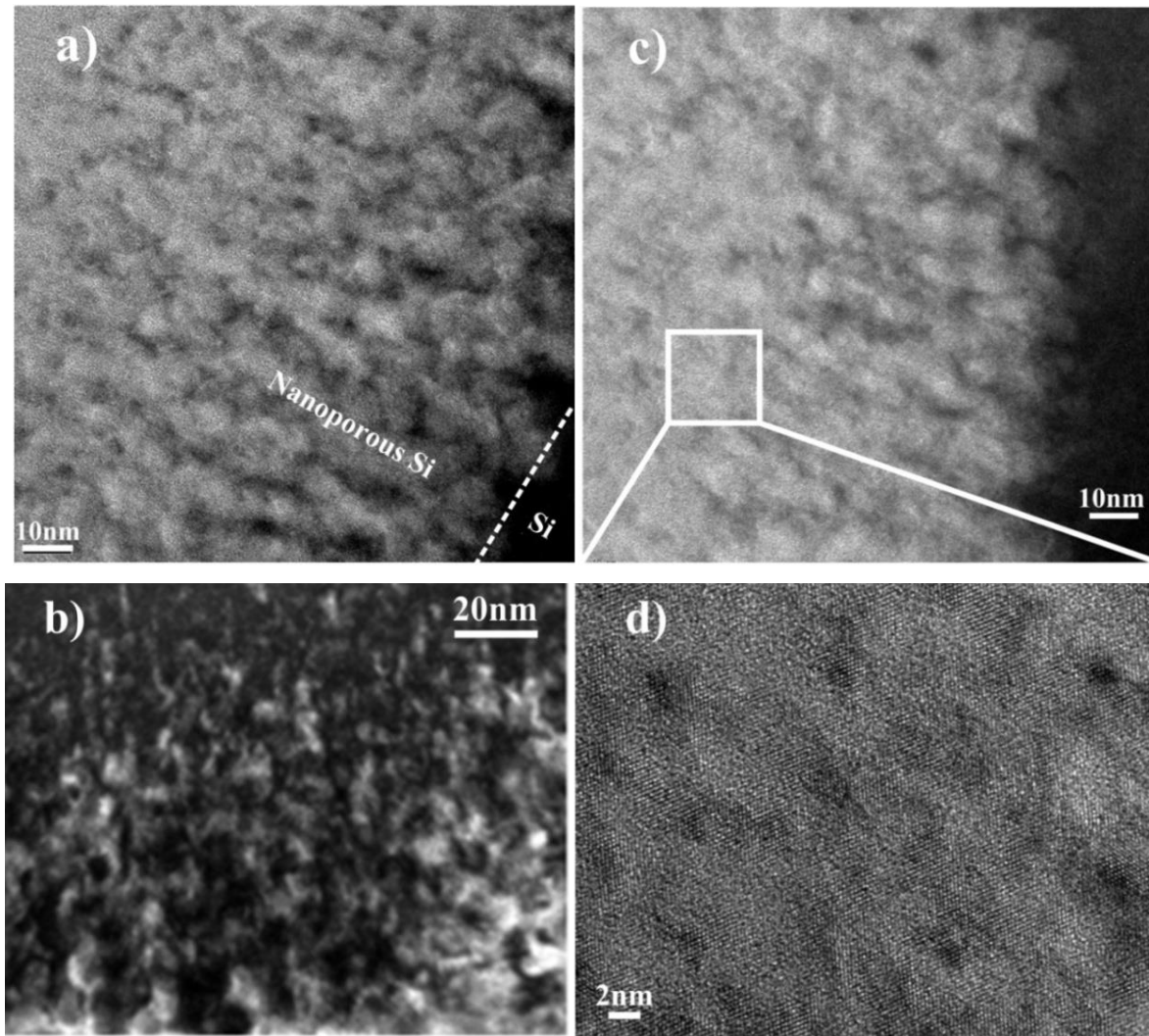


Figure 6.4: (a) Bright-field TEM image of nanoporous Si layer showing the graded nanostructure of PS layer (the dashed line shows the interface of Si/n-PS and the direction toward the surface). (b) Dark-field TEM image of the nano-PS cross-section showing the diffracting nano-crystallites. By moving from the silicon/PS interface along the diagonal and toward the surface, the size of Si nanocrystals decreases. (c) TEM image from the Si/PS interface illustrating the smooth transition between Si and PS layer and uniform interface. (d) HRTEM image of the porous layer showing nano-crystallites of about 5nm in size.

One of the advantages of the anodic etching technique over metal-assisted etching is the smooth interface of silicon and PS film. In metal-assisted technique, metal nanoparticles, such as Pt, Ag, etc. are distributed on the surface of the silicon prior to immersion in an HF solution. Metal nanoparticles used as the etching catalyst generate cylindrical holes, a few times larger than the nanoparticle size, into the silicon substrate.^{97, 98} Therefore, these nanoparticles can diffuse to the substrate deeper than the junction level. The latter becomes more important when PS formation is applied as a post-processing technique and control of emitter thickness is crucial.

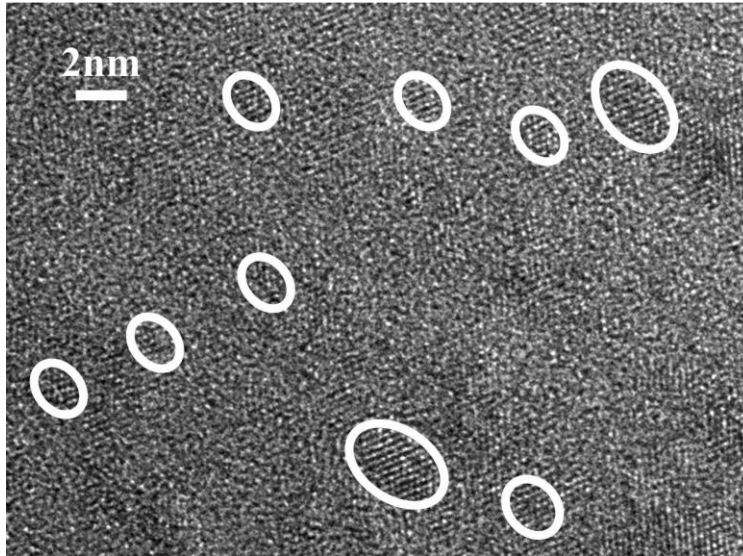


Figure 6.5: Bright-field TEM image showing the isolated Si nanocrystals close to the surface.

Diffracting Si nano-crystallites with dimensions of about 5nm can be observed. By getting closer to the surface the size of nanocrystalline decreases to less than 3nm and they become isolated in an amorphous matrix (Fig. 6.5).

The scanning transmission microscopy (STEM) image of the n-PS layer at the silicon interface is shown in Fig. 6.6(a). The structural morphology of the PS layer including the pores size, interconnections and branching pattern can be seen more clearly in the STEM image. Random branching of silicon interconnections of less than 10nm starts from the silicon interface and pores with sizes of about 5 nm is observed.

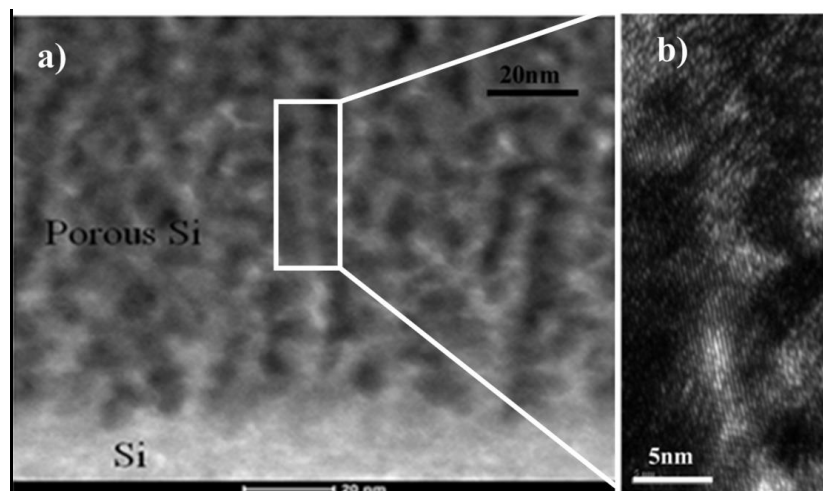


Figure 6.6: a) Scanning tunneling electron microscopy image of n-PS layer showing the growth morphology (branching) of the PS layer. b) Dark-field TEM image of the crystallites close to the Si interface.

Fig. 6.6(b) shows the dark-field image of the crystallites close to the Si interface. Si nanocrystals which are fringing can be observed in this image. The nanocrystal network is not continuous and many defects and amorphous structures can be observed in the nanoporous network. Amorphous silicon in the PS layer can easily oxidized and form an oxide matrix.

Cross-sectional TEM images of nanoporous layer formed under higher anodization current of 1A are illustrated in Fig. 6.7. The BF-TEM image shows graded-size nanocrystals and Si-QDs layer.

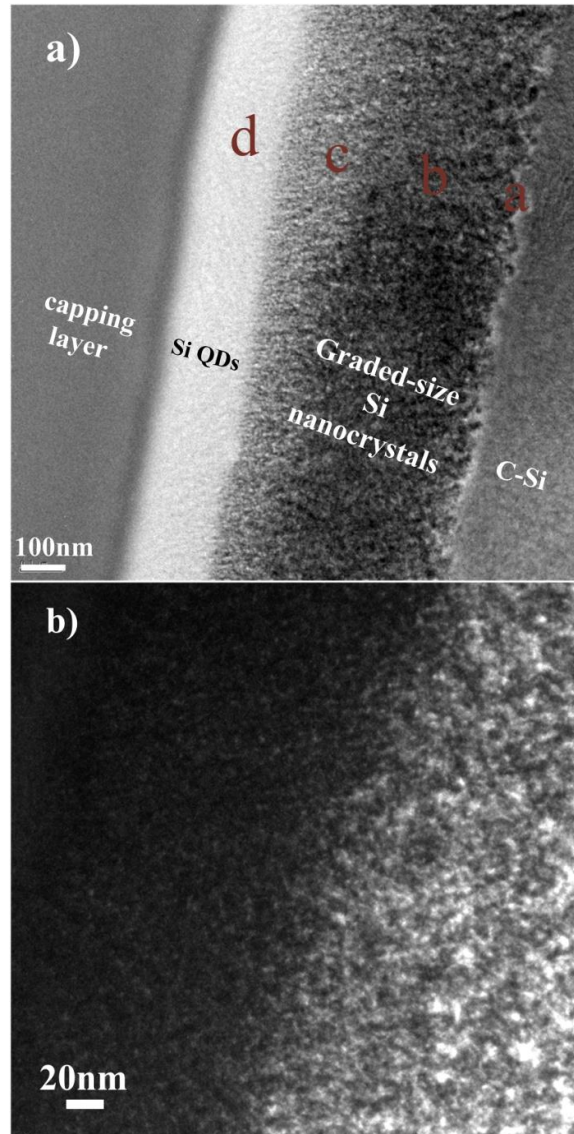


Figure 6.7: a) Cross-sectional, bright-field TEM image of nanoporous layer formed under higher anodization current of 1A. The brighter part of Porous layer is marked as Si-QDs. This layer contains quantum size Si nanoparticles less than 2nm which are isolated and distributed in an oxide matrix. b) Dark-field TEM image taken from the interface of Si-QDs layer and graded-size Si nanocrystal layer. This image clearly shows crystallite size gradually decreases and crystallites are isolated close to the surface.

As can be seen in this image the colour of the Si-QDs layer is brighter in the structure of nanoporous Si. This can be attributed to the high content of oxygen in the Si-QDs layer coming from the oxide matrix. The detailed elemental study of this layer is performed by means of EELS, EDX and energy filtered TEM.

Fig. 6.7(b) shows dark-field TEM image taken from the interface of Si-QDs layer and graded-size Si nanocrystal layer. This image clearly shows that the crystallite size gradually decreases and crystallites are isolated close to the surface. In comparison with the nanoporous layers obtained at lower currents (0.55A, Fig. 6.4), the size of crystallites at the interface of Si/n-PS is larger and also the Si-QDs layer formed on top the nanoporous layer is thicker. However, the graded-size network of nanocrystals has a same pattern as in samples anodized with different currents.

High resolution TEM images of the graded-density nanoporous layer formed at current of 1A are collected in Fig. 6.8. These images are taken from four spots marked in Fig 6.7 (a). They show the nanostructure of the porous layer in high resolution by moving from the Si/n-PS interface towards the surface of the nanoporous layer. Pore nucleation starts from surface of silicon and propagates to the crystal volume. It has been reported that the mechanism of the pore growth depends on the crystalline orientation of the silicon substrate. In a (100) Si substrate regardless of type, pores grow in $\langle 100 \rangle$ direction perpendicular to the surface of the substrate. It has been shown that the pores in n-type Si substrate only grow in $\langle 100 \rangle$ and $\langle 113 \rangle$ directions.^{62,63} Directional growth of pores was also observed in silicon spheres.

Fig. 6.8(b) shows a nanostructured crystalline network of n-PS and the propagation of pores in crystal volume. The pore growth direction can more clearly be observed in scanning TEM images. Isolated Si nanocrystals with dimensions of less than 2nm were observed in the Si-QDs layer (marked in Fig. 6.8(d)). However, due to the thickness of TEM samples, fringing in Si-QDs with dimensions of less than 2nm can hardly be observed in bright-field images.

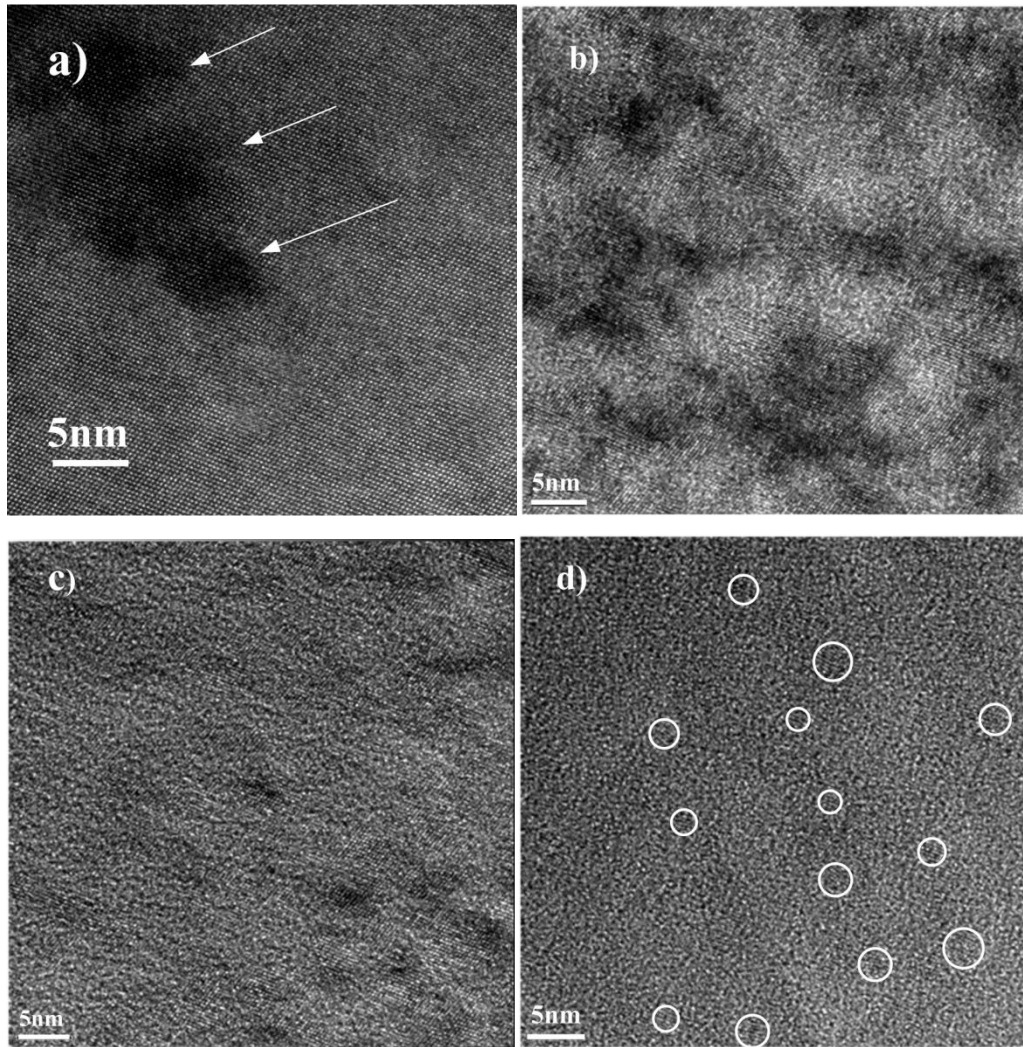


Figure 6.8: High resolution TEM images of graded-density nanoporous layer formed under higher anodization current of 1A. Images are taken from four spots as marked in Fig 6.7(a) (corresponding to a, b, c, and d). (a) Formation of pores with dimensions of about than 10nm in crystalline silicon structure (b) Nanostructured crystalline network of n-PS and propagation of pores in crystal volume. (c) Formation of isolated Si nanocrystals. (d) Isolated Si nanocrystals with dimensions of less than 2nm.

The result of the transmission electron diffraction (TED) study is shown in Fig. 6.9. The smallest aperture, with a size of about 250nm, was used to study the diffraction patterns. Selected area diffraction patterns (SADP) were obtained from the bulk of spheres, graded-size nanocrystal layer and Si-QDs embedded in the oxide matrix. The SADP obtained from the bulk of the Si sphere illustrated a perfect crystal structure. However, diffraction patterns obtained from the graded-size nanocrystal layer showed slight crystal imperfection. Arced reflections were observed in TED patterns obtained from the Si-QDs embedded layer.

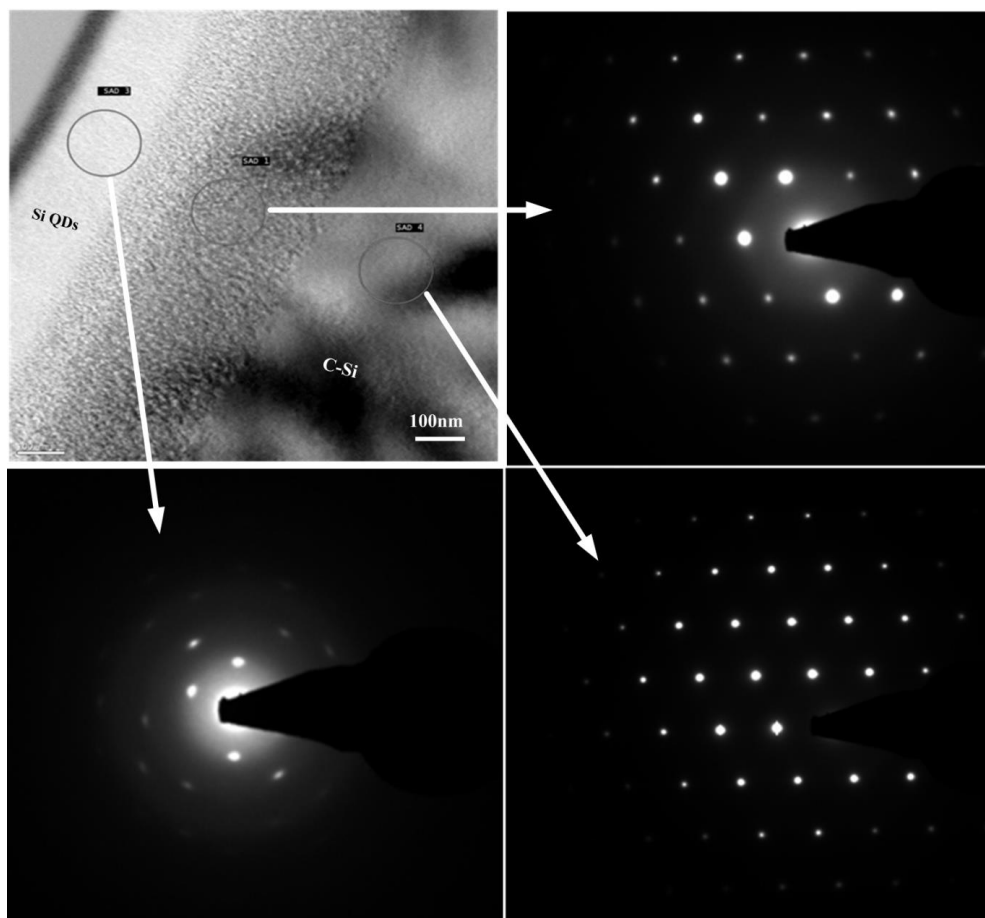
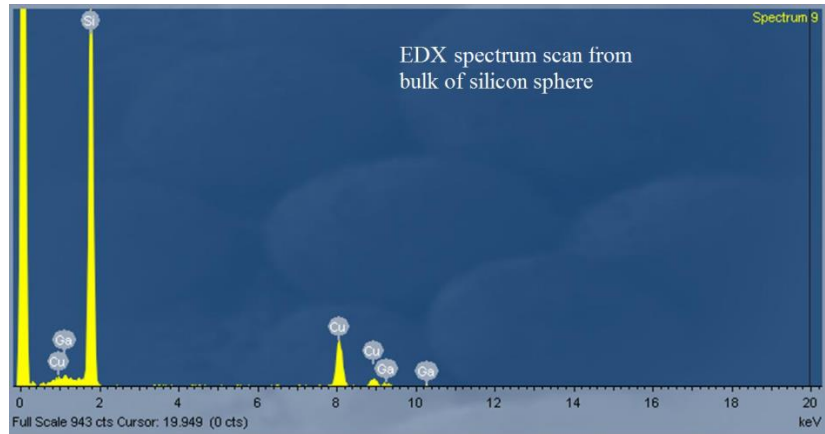


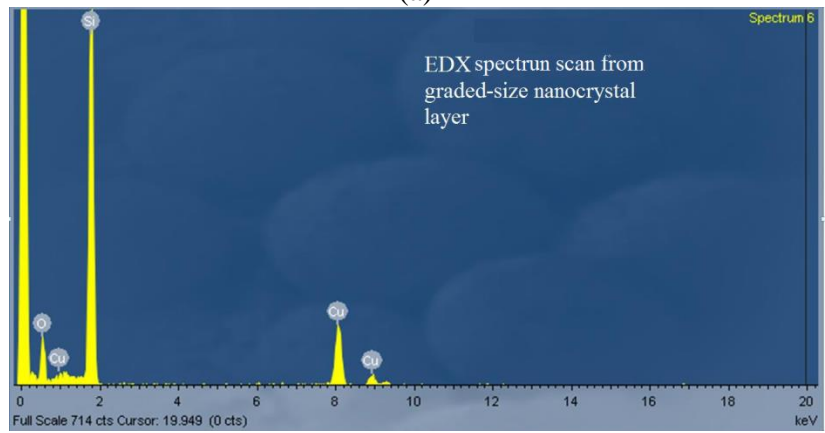
Figure 6.9: Transmission electron diffraction (TED) pattern of Si obtained from the bulk of spheres, graded-size nanocrystal layer and Si-QDs embedded in oxide matrix. Arcing only observed in TED pattern of Si-QDs embedded in oxide matrix. This can be attributed to the misoriented nanocrystals embedded in an oxide matrix.

This can be attributed to the misoriented nanocrystals in this layer. Since these Si-QDs are embedded in an amorphous matrix, misoriented nanocrystals with slight deviation from the crystal structure can cause arced reflections.

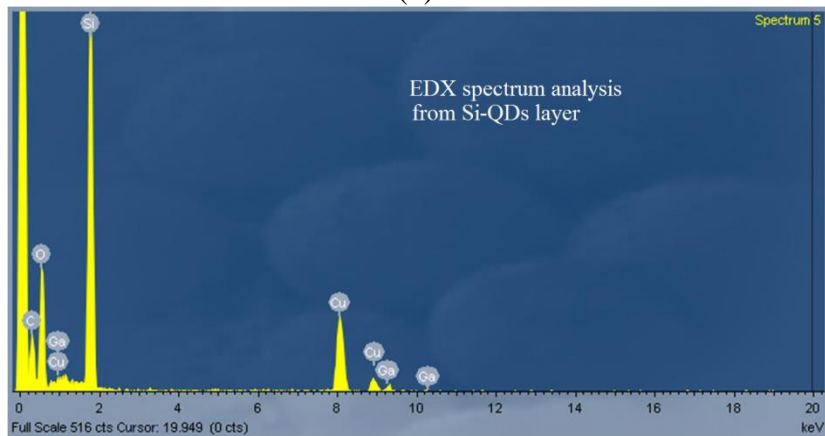
The result of the elemental study on different areas of nanoporous layer has been shown in Fig 6.10. EDX spectrum scans were collected from an area of $100 \times 100 \text{ nm}^2$ on the bulk of Si spheres, graded-size nanocrystal layer and Si-QDs layer. As can be seen in these spectra, the peak corresponding to oxygen is significantly increased in the spectrum obtained from Si-QDs layer. Ga, Cu, and C were also observed in the spectra. Ga has been induced from the FIB sample preparation and Cu is coming from the TEM grid. High carbon contamination in the Si-QDs layer is induced from the carbon capping layer.



(a)



(b)



(c)

Figure 6.10: EDX spectrum scan of $100 \times 100 \text{ nm}^2$ area from (a) bulk of Si spheres, (b) graded-size nanocrystal layer and (c) Si-QDs. As can be seen in these spectra, oxygen content in Si-QDs layer is significantly increased. Ga, Cu, and C were also observed in the spectra. Ga has been induced from the FIB sample preparation and Cu is coming from the TEM grid. High carbon contamination in Si-QDs layer is induced from the carbon capping layer.

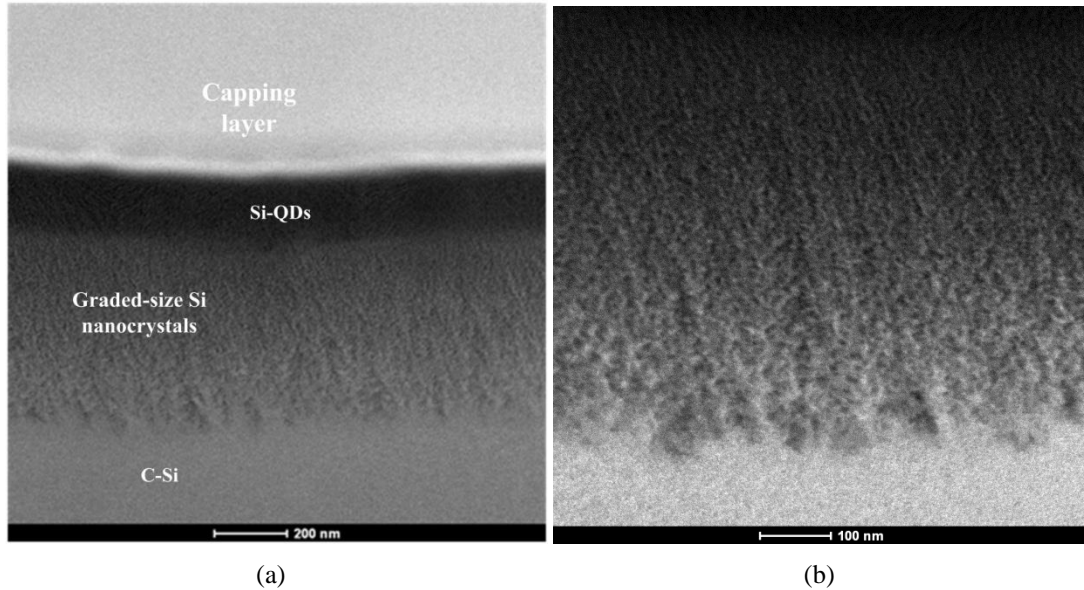


Figure 6.11: Scanning tunneling electron microscopy images of nanoporous layer formed by anodization current of 1A, showing the growth morphology and pore branching in the PS layer.

Scanning TEM is more favorable when studying the morphology and pore propagation in nanoporous layers. Fig. 6.11 shows the STEM images of the n-PS layer obtained by anodization current of 1A. The pore propagation and crystallite size in nanoporous silicon is controlled by different factors such as anodization current, doping concentration, and the type of substrate. As can be seen in this figure, the crystallites sizes are significantly larger at the interface of Si/n-PS. These spheres are p-type Si and uniformly doped by phosphorous to make a junction of about 0.7 μ m depth. The porous layer thickness of the samples anodized by 1A is about 0.7 μ m which is comparable to the junction depth. The lower doping concentration close to the junction can affect the pore formation mechanism and also crystallite size. The change in the pore dimensions and crystallite size might induce a significant stress to the porous layer. Fig. 6.12 shows the nanoporous layer detached and separated from the bulk of the sphere close to the junction depth. This can be attributed to the stress between nanoporous layer formed in the n+ emitter region and lower doping concentration region close to the junction. This can also explain the drop of external quantum efficiency of spherical cells anodized at currents higher than 1A.

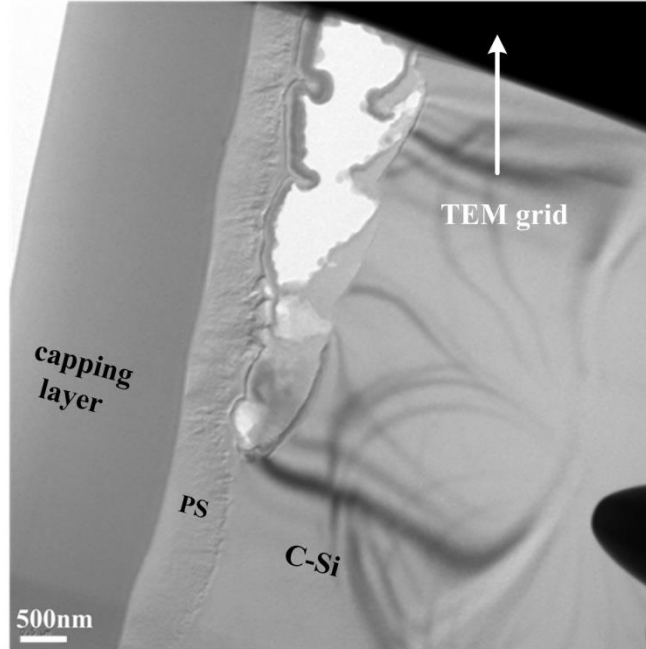


Figure 6.12: STEM image of nanoporous layer formed at anodization current of 1A. The nanoporous layer is broken and separated from the bulk of sphere. This can be attributed to the stress between nanoporous layer formed in n+ emitter region and lower doping concentration. This can also explain the drop of external quantum efficiency of spherical cells anodized at currents higher than 1A.

6.5 EDX and EELS line scan analyses: linear graded-density PS

Fig. 6.13 shows the cross-sectional STEM image of the nanoporous layer obtained using an anodization current of 0.7A. During the FIB preparation process a thin layer of Pt was deposited onto the surface of the n-PS layer using an electron-beam. This Pt layer protects the surface of the nanoporous layer from any damage during ion milling. The electron-beam Pt deposition is carried out on samples where studies of features close to the surface are of interest. The capping-Pt layer on top of the PS layer is observed to be brighter than other layers in the scanning TEM image. Since the rate of Pt-deposition by electron beam is low, subsequently, a thicker layer of carbon is deposited by an ion-beam technique.

Same as other investigated nanoporous layers, the nanostructure of this layer is consisting of graded-size nanocrystals and Si-QDs embedded layer. In order to study the elemental composition and intensity of Si and O along the graded-density nanoporous layer, EELS and EDX line scans, spot analyses, and spectrum scans were performed. The EDX line scans show the intensity of elements along the nanoporous layer; while, EDX spot analyses are required to reveal the elemental compositions of the nonporous layer.

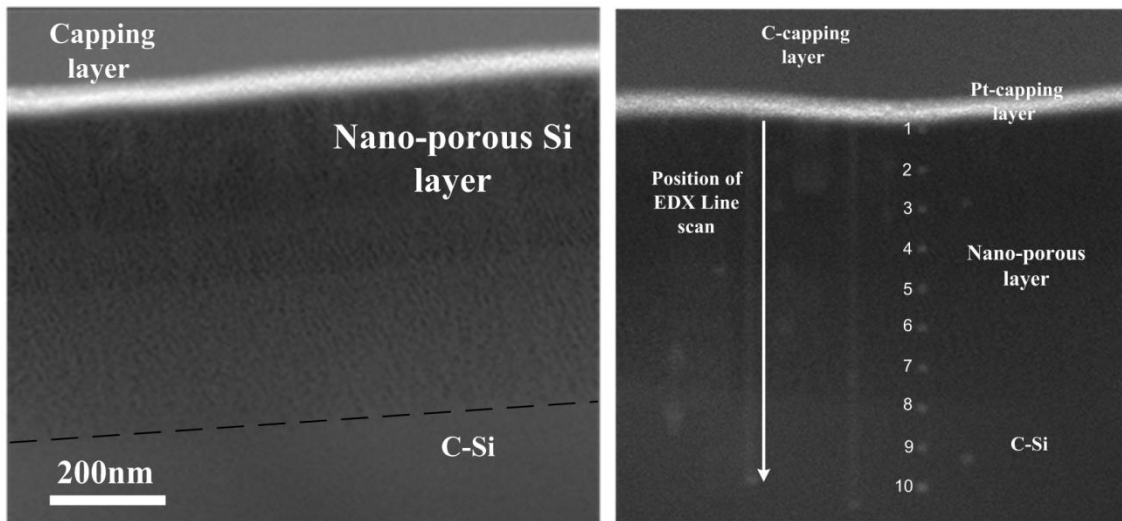


Figure 6.13: (left) STEM image showing morphology of graded-nanoporous layer obtained by anodization current of 0.7 A. (Right) Positions of EDX spot analysis and line-scan along the graded-density nanoporous layer have been marked.

Depth profiles obtained by EELS measurements confirm the data collected from the EDX analyses. The result of EDX line scan analysis along the nanoporous layer, from the surface towards the Si interface, is depicted in Fig. 6.14. The position of the line scan is marked in Fig. 6.13 by an arrow. The Si intensity in the bulk of silicon is constant and gradually decreases in a linear form along the graded-size nanocrystal layer. By getting closer to the surface (about 200nm), the Si intensity decreases more slowly. As observed in DF-TEM and BF-TEM images,

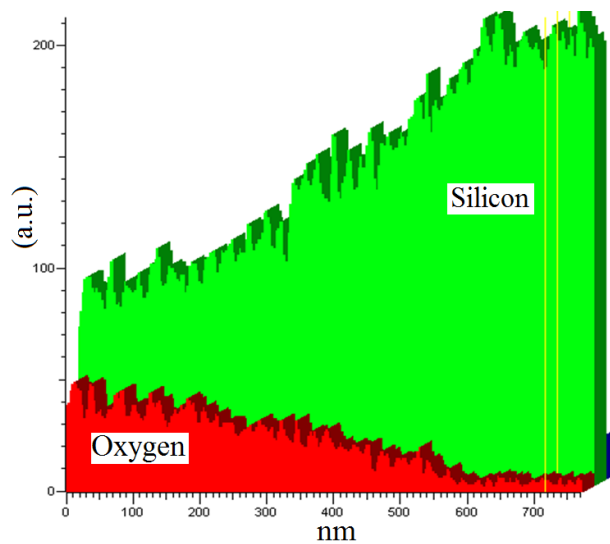


Figure 6.14: EDX line scan analysis along the nanoporous layer, from the surface towards the Si interface (The position of the line scan is marked in Fig. 6.13).

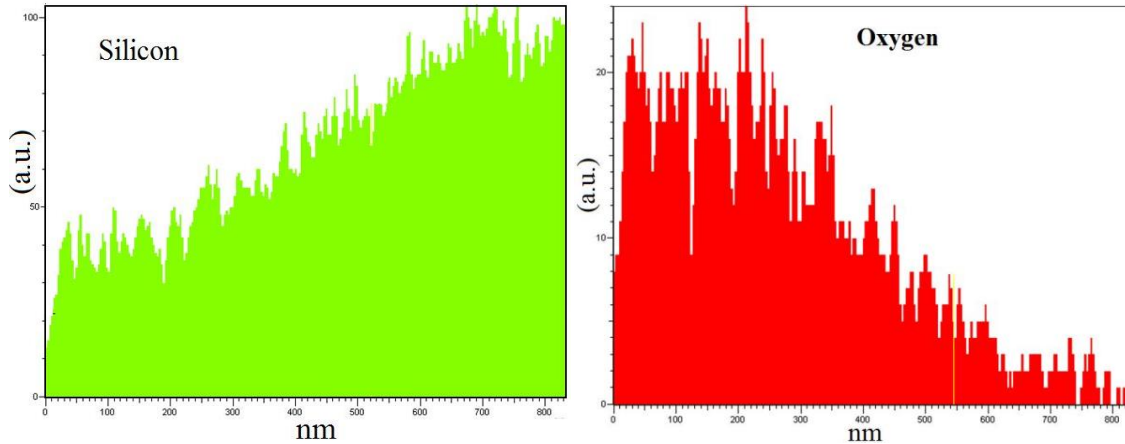


Figure 6.15: EDX line scan analysis along the nanoporous layer, from the surface towards the Si/n-PS interface performed on another area of this sample.

the size of silicon nanocrystals decreases to less than 2nm in the Si- QDs layer and Si intensity changes slowly in this layer. Oxygen intensity is also constant in the bulk of Si spheres (close to zero) and gradually increases to the maximum in the Si-QDs layer close to the surface. EDX line scan analysis performed on another area of this sample is illustrated in Fig. 6.15. In both analyses, silicon intensity gradually decreases along the nanoporous layer and oxygen intensity increases reaching its maximum close to the surface.

The result of elemental composition study is collected in Table 6.1. The spectra were obtained from the ten spots marked in Fig. 6.13. Based on the collected data, a small amount of oxygen exists in the crystal Si (S8, S9, S10) which is attributed to the native oxide formed on the surface of the thinned sample.

| Spectrum | Weight% O | Weight% Si | W% Total | Atomic% O | Atomic% Si |
|--------------|-----------|------------|----------|-----------|------------|
| Spectrum(1) | 43.92 | 56.07 | 100 | 57.89 | 42.10 |
| Spectrum(2) | 42.74 | 57.25 | 100 | 56.71 | 43.28 |
| Spectrum(3) | 43.53 | 56.46 | 100 | 57.51 | 42.48 |
| Spectrum(4) | 31.92 | 68.07 | 100 | 45.15 | 54.84 |
| Spectrum(5) | 24.44 | 75.55 | 100 | 36.22 | 63.77 |
| Spectrum(6) | 19.74 | 80.25 | 100 | 30.16 | 69.83 |
| Spectrum(7) | 14.31 | 85.68 | 100 | 22.67 | 77.32 |
| Spectrum(8) | 4.80 | 95.19 | 100 | 8.14 | 91.85 |
| Spectrum(9) | 3.24 | 96.75 | 100 | 5.56 | 94.43 |
| Spectrum(10) | 3.43 | 96.562 | 100 | 5.88 | 94.11 |

Table 6.1: Result of EDX spot analyses marked in Fig. 6.13.

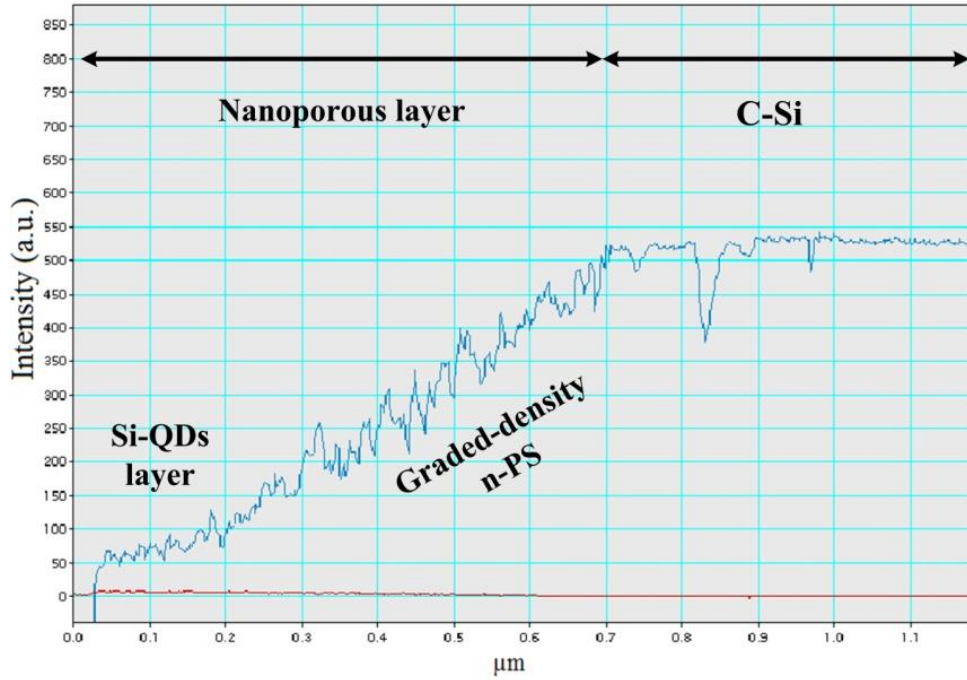
| Spectrum | Weight% O | Weight% Si | W% Total | Atomic% O | Atomic% Si |
|--------------|-----------|------------|----------|-----------|------------|
| Spectrum(1) | 34.12 | 65.87 | 100 | 47.63 | 52.36 |
| Spectrum(2) | 30.44 | 69.55 | 100 | 43.45 | 56.54 |
| Spectrum(3) | 31.93 | 68.06 | 100 | 45.16 | 54.83 |
| Spectrum(4) | 31.89 | 68.10 | 100 | 45.11 | 54.88 |
| Spectrum(5) | 20.66 | 79.33 | 100 | 31.38 | 68.61 |
| Spectrum(6) | 14.57 | 85.42 | 100 | 23.04 | 76.95 |
| Spectrum(7) | 10.21 | 89.78 | 100 | 16.65 | 83.34 |
| Spectrum(8) | 1.06 | 98.93 | 100 | 1.85 | 98.14 |
| Spectrum(9) | 0.84 | 99.915 | 100 | 0.14 | 99.85 |
| Spectrum(10) | 1.02 | 98.97 | 100 | 1.7 | 98.21 |

Table 6.2: Result of EDX spot analysis from another area of the sample anodized with 0.7A. The data is slightly different but still confirms the result of EDX study collected in Table 6.1.

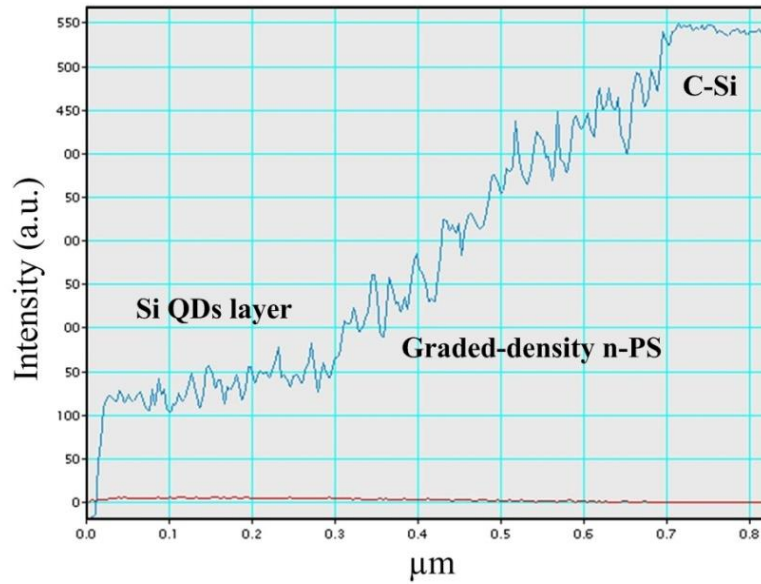
The ratio of oxygen to silicon (weight %) gradually increases along the nanoporous layer and reaches to 67% close to the surface. It is observed that the oxygen ratio to silicon is almost constant in the Si-QDs layer (S1, S2, and S3). Table 6.2 shows the result of EDX spot analysis from another area of this sample. The data is slightly different but still confirms the result of the EDX study collected in Table 6.1. As it can be seen in this table, the oxygen ratio to silicon is about 1% on the crystal silicon and increases to about 53% close to the surface.

Elemental depth profile of the nanoporous layers has also been studied by means of transmission EELS. The principle of the energy loss spectroscopy is based on the inelastic interaction of the TEM electron beam with atoms in the specimen. The elastic interactions will form the zero-peak loss in the spectrum; while inelastic interactions including plasmon excitations and inner-shell ionizations provide detailed information about the elements in the sample. Transmission EELS, as compared to EDX analysis, is more accurate and spectra with an energy resolution of less than 1eV can be collected.

The Si intensity depth profile obtained by EELS analysis is depicted in Fig. 6.16. Depth profiles in this figure were collected from different areas of the sample anodized at 0.7A. In the C-Si region, the Si intensity is almost constant and linearly decreases along the nanoporous layer. By getting closer to the surface, the Si intensity decreases more slowly and two regions with different slopes can be observed. These regions are assigned to graded-size nanocrystal layer and Si-QDs embedded layer. The latter is clearer in Fig. 6.16(b).



(a)



(b)

Figure 6.16: Si-intensity depth profiles of nanoporous layer, obtained by energy loss spectroscopy analysis. (a) and (b) are collected from different areas of the sample anodized at 0.7A (same sample used for EDX analyses).

6.5 EELS investigation of Si quantum dots embedded in nanoporous oxide: stability properties of oxide matrix

EELS spectra recorded from Si-QDs embedded in oxide matrix, before and after irradiation with a high energy electron beam (300KeV), are depicted in Fig. 6.17. The core-loss EELS spectra are obtained through inelastic interaction of the electron beam with inner-shell electrons of atoms in the specimen where the energy loss is recorded by the spectrometer. The collected spectra show the Si L edges and the oxygen K edges from the unirradiated and irradiated silicon quantum dots embedded in oxide matrix. The characteristic edge structure of pure Si with an edge at 100eV and first maximum at 102eV as well as SiO₂ with an edge onset at 106eV and strong peaks at 108 and 114eV can be seen. The Si-L₁ edge of silicon quantum dots and SiO₂ matrix were observed at 152eV and 157eV, respectively. No significant change was observed in the intensity of the O-K edge (~540eV) of silicon oxide after irradiation. This indicates the oxide matrix formed in nanoporous layer is stable and it is not sensible to the electron beam. However, it is reported that the oxide formed in the macroporous silicon layer containing pores in the micron size is sensible to the electron beam and the O-K signal almost disappears after irradiation.⁹⁹

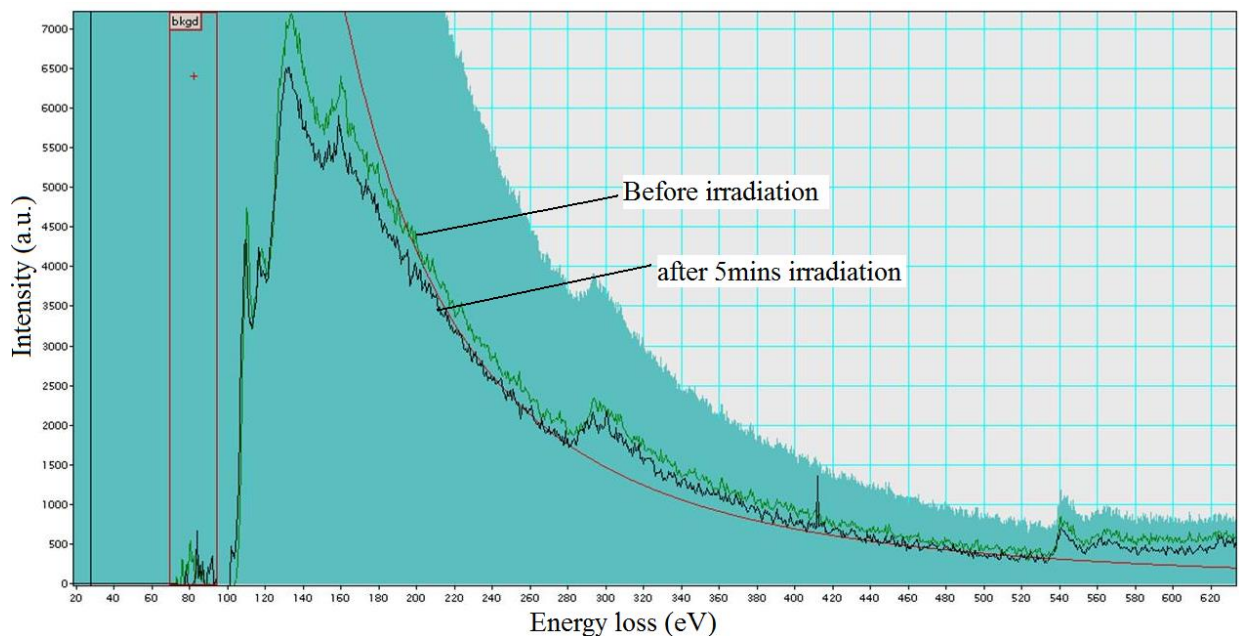


Figure 6.17: Energy loss spectra showing Si L edges and the oxygen K edges from the unirradiated and irradiated silicon quantum dots embedded in oxide matrix. The back ground is subtracted to highlight the Si L edge.

6.6 Energy filtered TEM study of Si nanocrystals in n-PS layer

Since plasmon peaks of Si and silicon oxide are positioned at different energies, 16.8 and 23 eV, energy filtered TEM is a useful technique to study the Si nanostructures in the oxide matrix. The EFTEM imaging technique is based on filtering of the electron beam by energy slit ($\sim 2\text{eV}$) to form the image of a specific element in the specimen. The EFTEM image produced from the plasmon peak of Si at 16.8eV, with 2eV energy slit, is shown in Fig. 6.18. The porous silicon network is bright, and the oxide matrix appears dark. The pore branching close to the crystal Si (C-Si) and isolated Si nanocrystals close to the surface are observed in this image. These quantum-size silicon nanocrystals are dispersed in an oxide matrix. However, the EFTEM image doesn't give any information about the crystallinity of the samples.

6.7 Raman spectroscopy

Raman spectra of samples with and without n-PS ARC layer, measured in broad range of 200-1200, are shown in Fig. 6.19. Unpolarised Raman spectra were collected at room temperature using an Ar ion laser excitation source, operating at 488nm wavelength. In order to reduce the laser-induced heating effect on nanoporous Si layers, the average laser power was about 1mW at

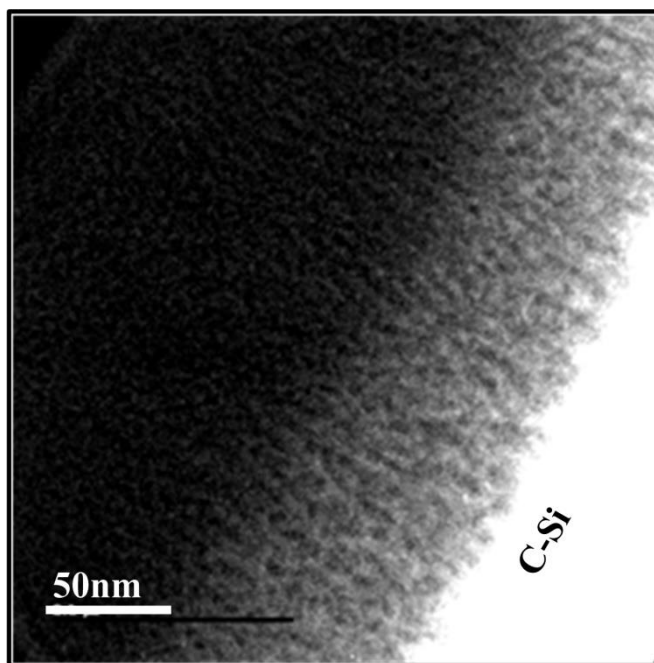


Figure 6.18: Energy Filtered TEM image showing filtered image of the plasmon peak of Si at 16.8 eV.

the sample surface. In comparison with bulk, the Raman peak in the n-PS silicon layer noticeably downshifted toward lower frequencies and asymmetrically broadened. In bulk crystalline silicon, because of conservation of phonon momentum q , only phonons at the centre of the Brillouin zone can take part in the Raman scattering process resulting in a narrow zone-centre optical mode around 520cm^{-1} at room temperature. However, in nanocrystalline silicon, localization of phonons in small grains relaxes the k -selection rule and allows phonons with $q \neq 0$ to contribute to Raman spectra.^{100,101} Therefore, in the n-PS layer with silicon interconnections (wires) and crystallites of about a few nanometers, the wave function of optical phonons is no longer a plane wave; and due to participation of phonons with $q \neq 0$ in Raman scattering process, the red shift and broadening of the Raman peak occurs.¹⁰²⁻¹⁰⁴ It has been established that the Raman peak shift toward lower frequencies is more pronounced with the decrease of nanocrystals size. There is also a shoulder appearing close to 480 cm^{-1} which corresponds to the position of the strong TO band in a-Si.

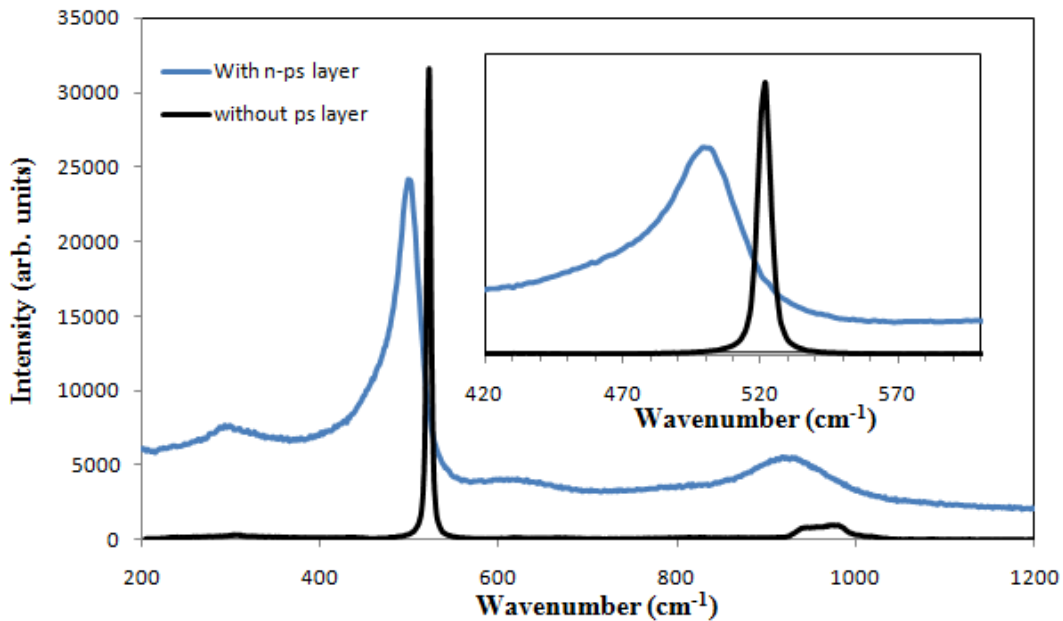


Figure 6.19: Room temperature Raman spectra of silicon spheres with and without graded-nanoporous layer. The silicon sphere spectrum without a PS layer is similar to standard bulk crystalline silicon with a peak around 521cm^{-1} . As can be seen in inset, Raman peak found to be broadened and downshifted in the silicon sphere spectrum with an n-PS layer.

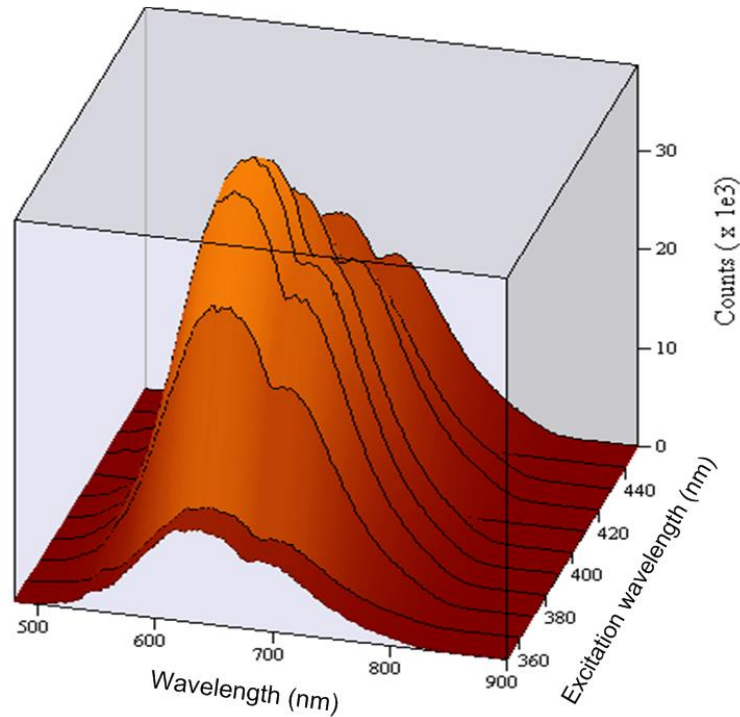


Figure 6.20: Photoluminescence spectra of Si-QDs.

6.8 Luminescence properties of graded-density nanoporous Si

The photoluminescence spectra of the graded-density n-PS layer formed on silicon spheres are collected in Fig 6.20. The PL spectra were collected with different excitation wavelengths at room temperature. Two strong peaks at wavelengths of 640nm and 690 were observed in the photoluminescence spectra which are independent of the excitation wavelength. Figure 6.21 shows the excitation spectrum of the emission intensity at 640nm. By changing the excitation wavelength the intensity of the emission peaks significantly changes. As can be seen in this spectrum the excitation wavelengths from 350 to 500, which are corresponding to high energy photon wavelengths in the solar spectrum, create strong emission peak at 640nm. Furthermore, the emission peaks lie in the high conversion efficiency region of spectral response of crystalline silicon solar cells.

Different luminescence mechanisms have been considered and proposed to be responsible for visible emission of nanoporous silicon. Mainly three different models have been discussed: 1) luminescence due to native oxide formed in the PS layer or defects in the SiO_x; 2) Visible

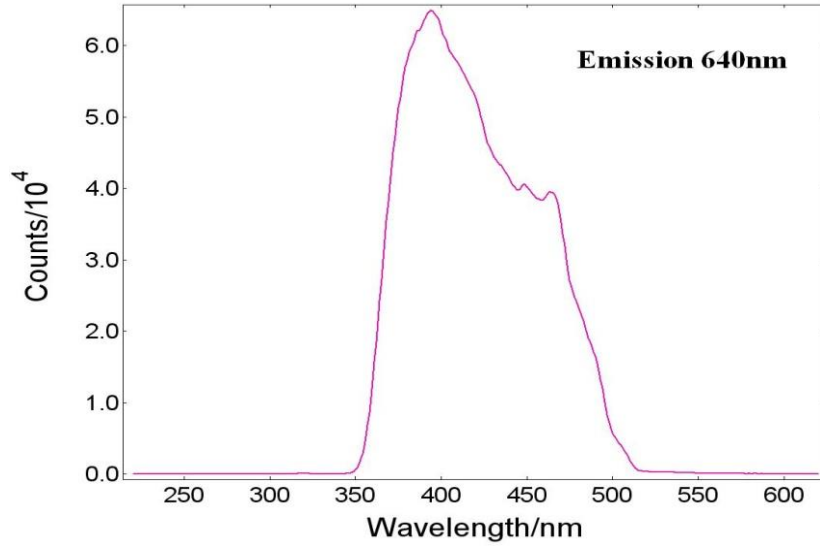


Figure 6.21: Excitation spectrum of the emission intensity at 640nm.

photoluminescence based on recombination of carriers confined in Si nano-crystallites or nanoscale interconnections (quantum confinement effect);^{31,37} 3) surface effect of Si nano-crystallites.⁷¹ Fig. 6.22 shows the optical image obtained by digital camera from luminescence of nanoporous layer formed on silicon spheres. An area of about $0.5 \times 0.5 \text{ cm}^2$ was illuminated by monochromatic light (380nm) from a xenon lamp.

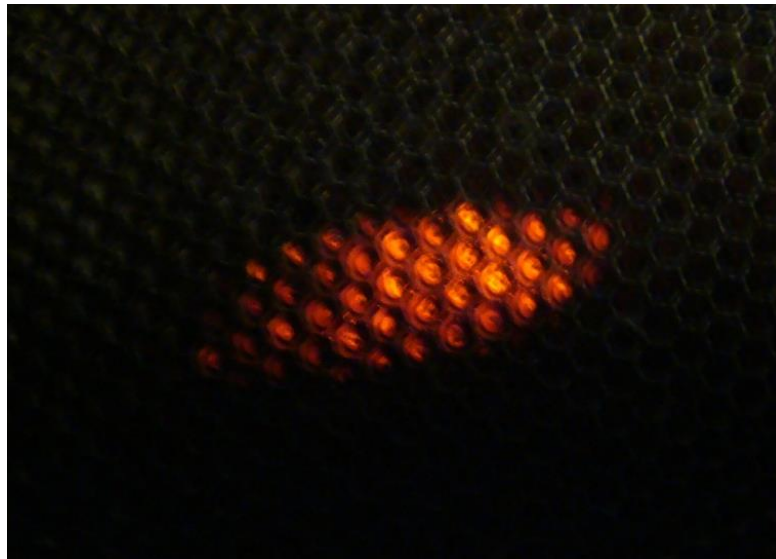


Figure 6.22: Optical image obtained by digital camera from luminescence of nanoporous layer formed on silicon spheres. An area of about $0.5 \times 0.5 \text{ cm}^2$ was illuminated by monochromatic light (380nm) from a xenon lamp.

6.9 Light trapping and external quantum efficiency of spherical silicon solar cells

Fig. 6.23 shows the schematic of silicon spheres with the integrated graded-density nanoporous Si layer. As seen in this image, the graded-density layer consists of graded-size silicon nanocrystals and quantum-size Si nanoparticles. These Si-QDs are embedded in an oxide matrix with high orange luminescence; therefore, they are shown with orange dots. The reflectance characteristics of spherical silicon solar cells with and without the n-PS ARC layer are depicted in Fig. 6.24.

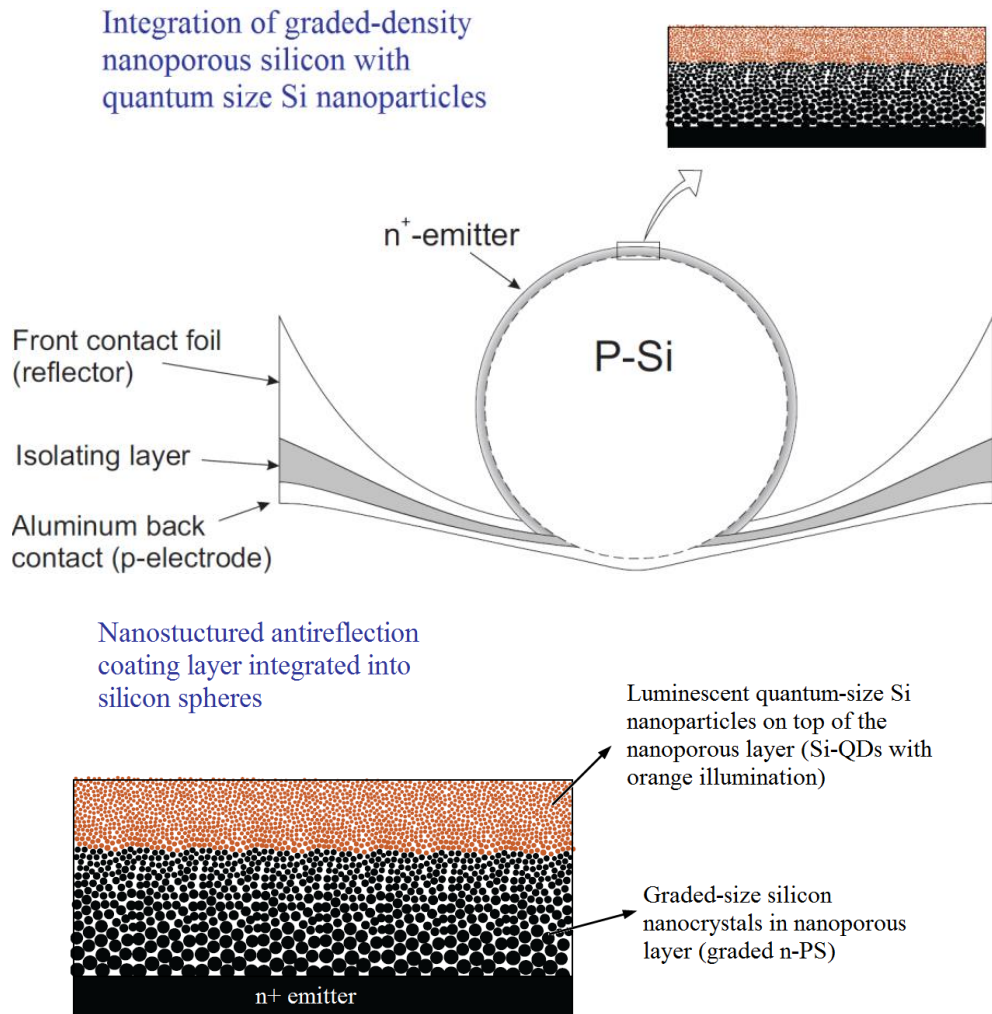


Figure 6.23: Schematic of spherical silicon solar cells with integrated graded-density nanoporous Si layer.

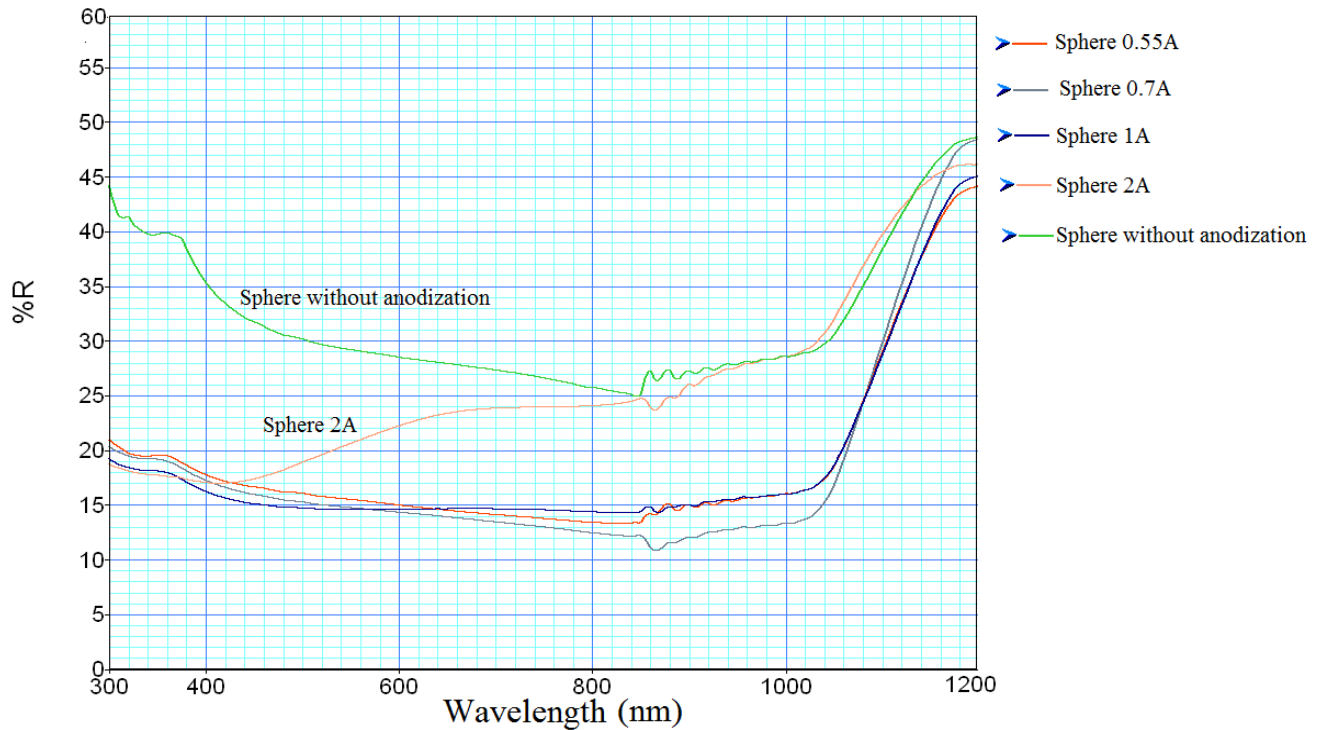


Figure 6.24: Reflectance characteristics of spherical silicon solar integrated with graded-density n-PS layers obtained by different anodization currents.

As can be seen in this Figure, in contrast to the regular PS layers, the graded-density film can uniformly suppress the reflectivity in the entire visible spectral range. However, due to the reflections from aluminum foil, the reflectivity of the cells with n-PS coating does not become zero. The refractivity of regular PS layers can be controlled by etching conditions to obtain a quarter-wavelength antireflection coating, which results in reduced reflectivity in certain frequencies. However, it is difficult to obtain a layer for efficient suppression of reflection in a broad spectral range. Also visible in this Figure, the reflection of cells integrated with n-PS anodized with currents less than 1A has reduced to less than 15% in a wide range of spectral response (400-1000nm). The samples anodized by high current of 2A showed different reflection behavior. This can be attributed to the decrease of the graded-size nanocrystal layer thickness at high currents as well as the separation of the n-PS layer from silicon crystal (Fig. 6.12). The suppression of the reflectivity in a wide range of the spectral response has been explained by Stephen and Cody¹⁰⁵ based on the graded refractive-index structure. Stephens and Cody have developed a model demonstrating a graded-textured surface with features smaller than the light wavelength can efficiently suppress the reflection through the entire usable spectrum. Fig. 6.25 to 6.29 show the external quantum efficiency spectra of silicon spheres integrated with graded-

intensity n-PS layer obtained by different anodization currents. The EQE measurements were performed on the same cell with and without ARC (before and after anodization). Spherical silicon solar cells integrated with graded-density n-PS obtained by anodization current of less than 0.7A, showed significant improvement in the whole range of spectral response. At higher anodization currents, due to the decrease of the effective emitter thickness and poor conductivity, the cell performance is degraded.

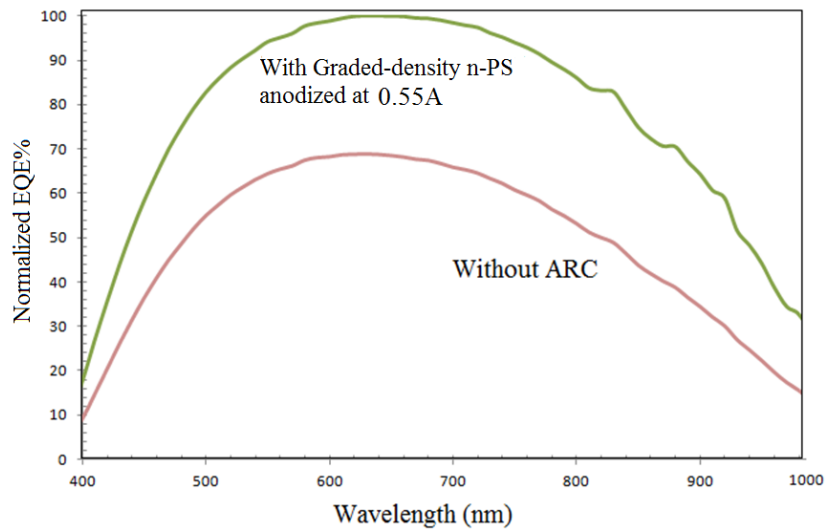


Figure 6.25: Spectral response measurements of spherical silicon solar cell with anodization current of 0.55A.

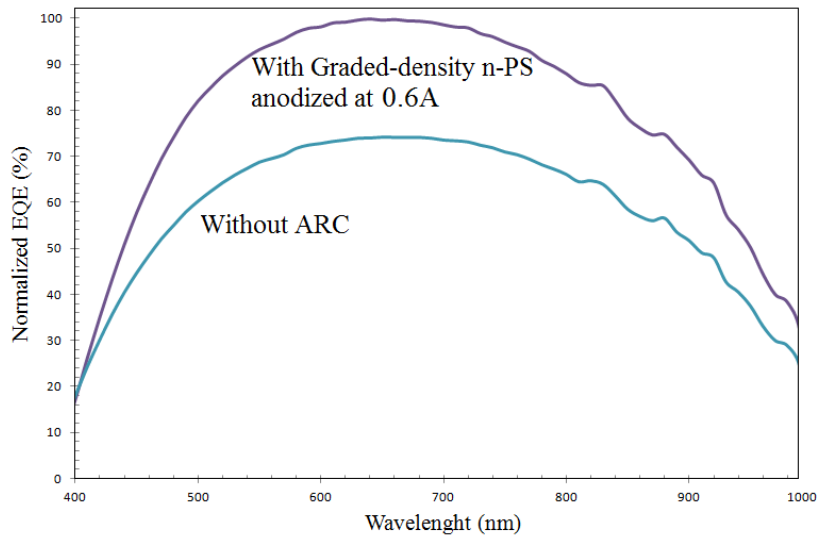


Figure 6.26: Spectral response measurements of spherical silicon solar cell with anodization current of 0.6A.

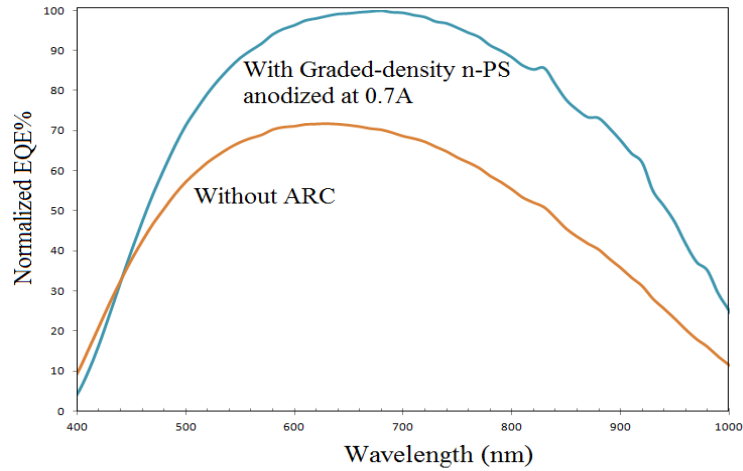


Figure 6.27: Spectral response measurements of spherical silicon solar cell with anodization current of 0.7A.

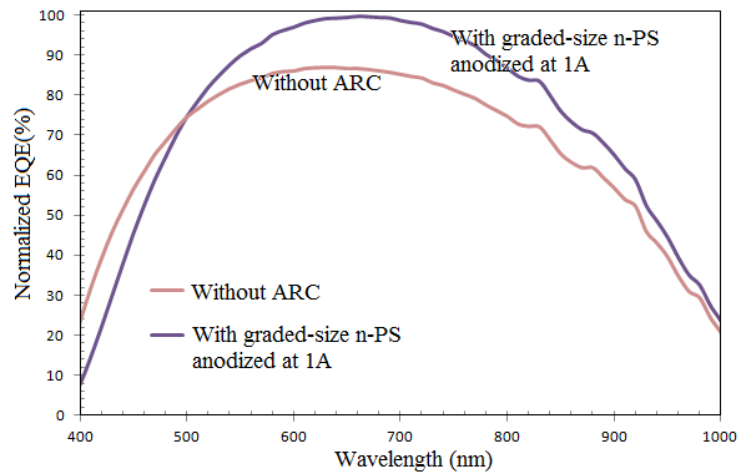


Figure 6.28: Spectral response measurements of spherical silicon solar cell with anodization current of 1A.

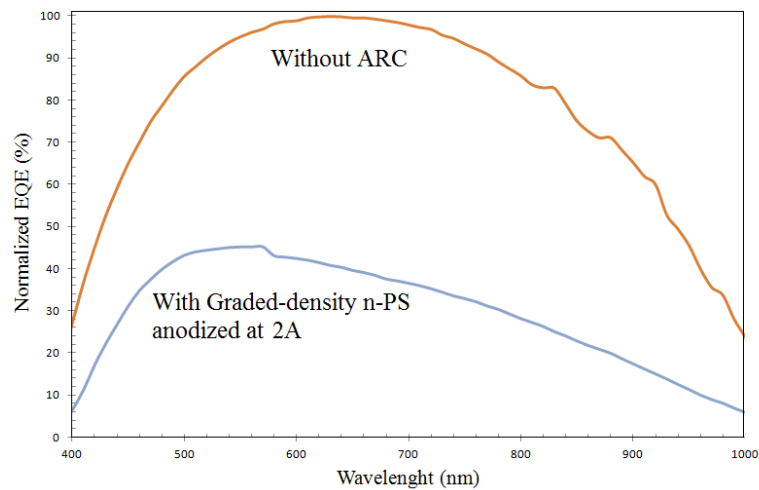


Figure 6.29: Spectral response measurements of spherical silicon solar cell with anodization current of 2A.

The significant improvement of the spectral response is attributed to the light trapping and light-diffusing behavior of graded-density n-PS as well as the bandgap opening in this layer. Due to the quantum confinement effects of Si-QDs in the nano-PS layer, the bandgap opening results in highly transparent porous Si layer minimizing the absorption of incident photons inside the PS layer. The high luminescent Si-QDs embedded layer can be employed as an efficient down-shifting layer to improve the absorption of high energy photons. However, efficient optical capping layers are required to prevent the escape of re-emitted photons from the surface of the silicon.

By increasing the anodization current, less improvement in blue spectral response were observed. This can be attributed to the effect of the shallow emitter and increase of the surface recombination velocity due to the induced defects.

6.10 Conclusion

We successfully developed and integrated a graded-density nanoporous layer into spherical silicon solar cells. This layer has been characterized by the means of scanning electron microscopy (SEM), transmission electron microscopy (TEM), Scanning tunneling TEM, energy filtered TEM, dark-field TEM, transmission electron diffraction (TED), electron energy loss spectroscopy (EELS), energy dispersive x-ray (EDX), Raman spectroscopy and photoluminescence spectroscopy (PL). Due to the quantum confinement effects, this ARC layer shows incredible properties such as enhanced luminescence, light trapping, photon-shifting and bandgap opening. The nanostructured porous layer consists of graded-size silicon nanocrystals and quantum-size Si nanoparticles embedded in an oxide matrix. The graded-size structure explains the suppression of reflectivity at the wide range of spectral response (black silicon). Quantum-size silicon nanoparticles with dimensions less than 2nm justify the significantly high luminescence. Bandgap opening in the emitter structure minimizes the absorption of photons in the dead layer and improves the short circuit current. The spectral response of silicon spheres integrated with graded-density n-PS layers exhibited significant improvement in a wide range of the spectral response.

Chapter 7

Hemispherical nanopit silicon texturing: a novel method of texturing based on etching through a liquid-phase deposited mask

7.1 Introduction

Currently, in commercial solar cells, the standard process for silicon wafer texturization is to form random pyramids of about 5 to 10 μ m in size on the Si surface. These pyramids are formed during an anisotropic etching process and by removal of about 20 μ m from the surface silicon. Anisotropic etching of Si, using alkaline solutions such as sodium hydroxide (NaOH), potassium hydroxide (KOH), sodium carbonate (NaCO₃), etc., has been extensively studied for texturization of (100)-oriented single-crystalline Si.¹⁰⁶⁻¹⁰⁸ However, since the method is based on selective etching of (100) planes, it cannot be applied to multicrystalline Si (mc-Si) with randomly oriented grains. For texturing mc-Si, several other methods have been proposed, such as reactive ion etching,¹⁰⁹ acidic etching,¹¹⁰ laser cutting, “honeycomb” texturing,¹¹¹ and porous Si layer formation.¹¹² Among these methods, “honeycomb” texturing considerably reduces optical losses and improves photon trapping. In this method inverted hemispheres are isotropically etched through patterns (holes) that are formed photolithographically on a thermally

grown oxide layer. The method developed in this research is cost efficient and requires no photolithography or mask deposition steps, and it can be applied post-process since it does not require any mask formation at high temperature.²⁶

In this technique, we use hydrofluorosilicic acid (H_2SiF_6) as the anodization solution. H_2SiF_6 is the byproduct of silicon etching in Hydrofluoric acid (HF). Therefore, we can consider this solution as an HF solution which has reached close to the saturation by dissolving of silicon. During the anodization process using H_2SiF_6 , two reaction mechanism of silicon etching and deposition of SiO_x , occur simultaneously. The liquid phase deposited SiO_x acts as a mask on the surface of the silicon and hemispherical nanopits are formed by isotropic etching through the holes in this mask. The key feature of this method is the utilization of an LPD oxide layer which grows simultaneously during the etching process. An important advantage of this method over all other texturing methods is removal of less than 1 μm from the surface of the silicon to produce a uniform texturing. The developed nanopit-texturing method has also potential applications in fabrication of selective emitter solar cells and it can be applied as post-processing texturing method to advance photovoltaic and photonic devices. This novel method of texturing is extensively studied and the spectral response of spherical silicon solar cells textured by this method was investigated.

7.2 Surface morphology of nanotextured silicon spheres and elemental study of LPD mask

A conventional single tank system was used for the electrochemical etching process. A platinum grid was used as the cathode and a mixture of diluted H_2SiF_6 (35% with H_2O) and ethanol was prepared as the electrolyte solution. The samples were mounted by screw pressure at the bottom of the Teflon cell with an opening of 2-inch diameter. The anodizations were performed at room temperature with various constant current densities for periods of up to two minutes. A constant current of 550 mA was imposed in the anodization tank and the forming voltage during the anodization process was 3.5 V. However, the voltage slowly increased during the anodization process due to the silicon texturing and changes at the surface of silicon. During the anodization process, a SiO_2 layer is uniformly grown on the Si spheres in an aqueous solution of H_2SiF_6 acid and at the same time the Si surface texturing with isotropic etch-pits takes place underneath the oxide layer. Fig. 7.1 shows the SEM image of the oxide layer formed on the surface of Si spheres

during the anodization process. Fig. 7.1(a) shows the image of the LPD silicon oxide layer covering the surface of the Si sphere. As can be seen in this figure, micro-pores are formed in the LPD oxide (Fig. 7.1(b)).

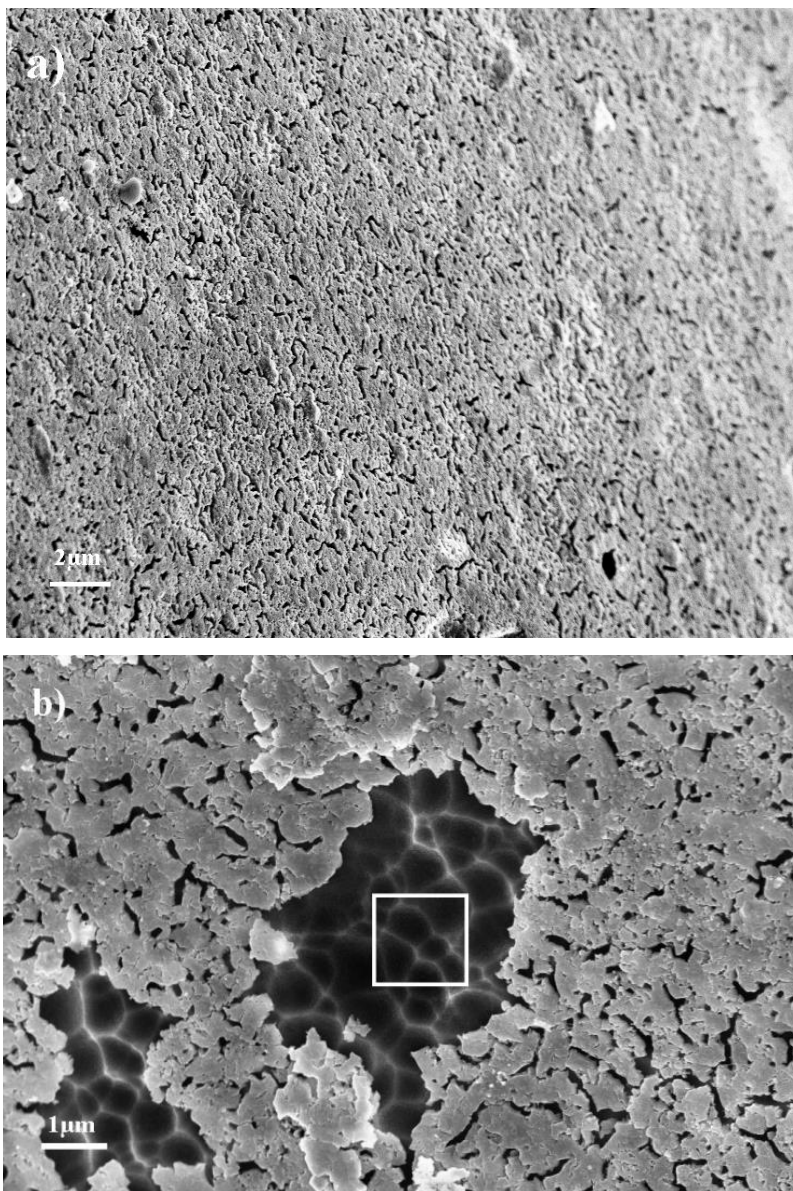


Figure 7.1: (a) SEM image of the LPD silicon oxide layer covering the surface of the Si sphere (image has been taken from the side of a sphere). Micro-pores can be observed in the oxide layer. (b) SEM image showing the textured Si surface underneath the silicon oxide layer, after partial removal of the latter (area marked by white box, used in EDX of figure 7.2(b)).

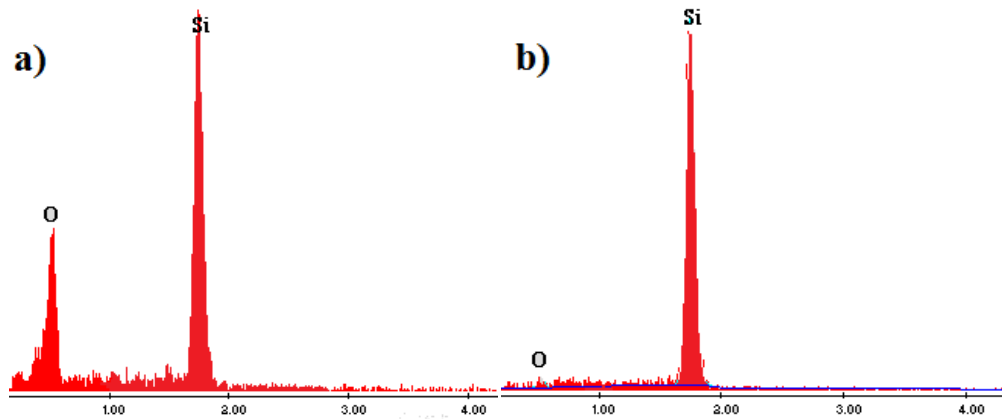


Figure 7.2: (a) EDX analysis of the liquid-phase deposited oxide. (b) EDX analysis of the exposed Si surface (marked by white box) of figure 7.1(b).

Fig. 7.1(a) shows the SEM image of the textured Si surface underneath the silicon oxide layer, after partial removal of the latter. Fig. 7.2(a) and (b) show the energy dispersive x-ray spectroscopy (EDX) spectra of the surface of the oxide layer of Fig. 7.1(a), and of the exposed textured Si (white box in Fig. 7.1(b)). While the Si and O are seen in the EDX spectrum of the LPD oxide layer, only Si appears in the EDX spectrum of the Si surface. Although the exposed Si surface may have contained a native oxide layer, no O appeared in the EDX spectrum indicating that the observed O in the spectrum of the LPD oxide layer is from the LPD growth.

Fig. 7.3 shows the SEM image of the thin layer of LPD silicon oxide covering the surface of the sphere. The thickness of the layer appears to be about 100nm. The solution reaches the surface of the silicon through the micro-pores and the silicon texturing and LPD oxide deposition simultaneously occurs.

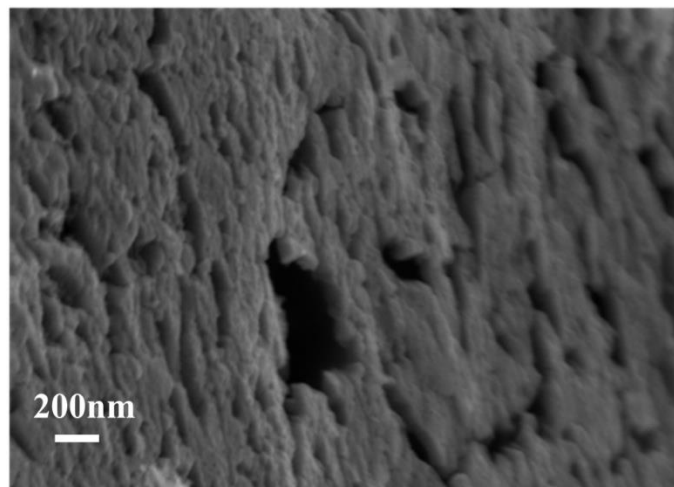


Figure 7.3: SEM image of the thin layer of LPD silicon oxide covering the surface of the sphere. The thickness of the layer appears to be about 100nm. The solution reaches the surface of silicon through the micropores and the silicon texturing and LPD oxide deposition simultaneously occurs.

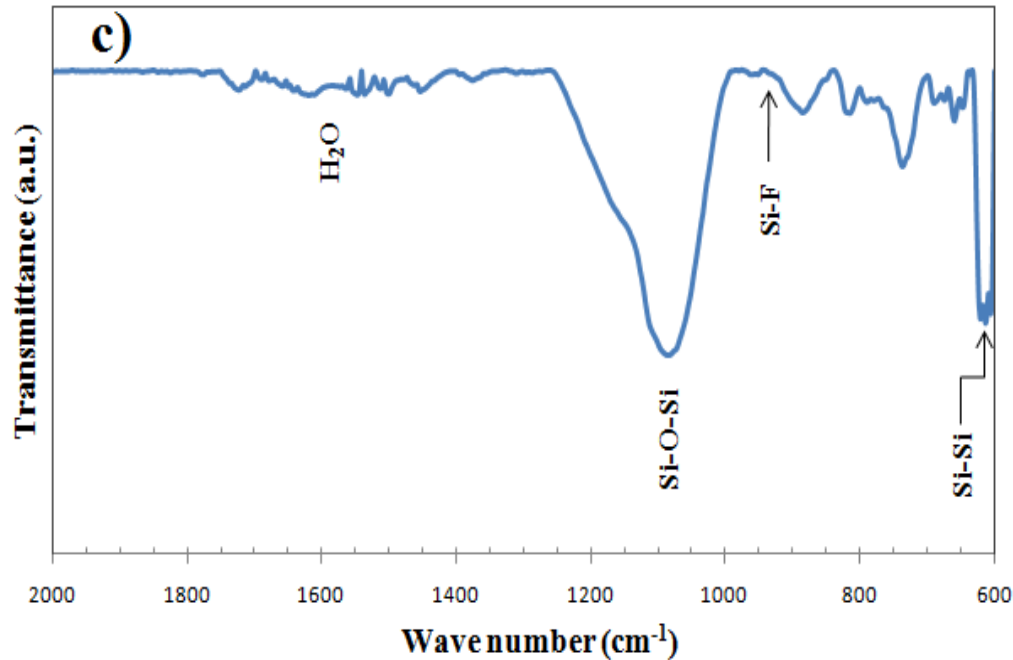


Figure 7.4: FTIR transmission spectrum of LPD oxide between 2000 and 600 cm^{-1} .

Fig. 7.4 shows the FTIR transmission spectrum of the LPD oxide layer. The absorption bands around 610 and 735 cm^{-1} are attributed to the silicon substrate. The absorption peaks corresponding to Si–O–Si stretching and bending vibration modes were observed at around 1085 and 810 cm^{-1} , respectively.¹¹³ The absorption band around 1600 cm^{-1} is attributed to H₂O vibrations. The 940 cm^{-1} peak for the Si-F stretching vibration was not obviously observed. The morphology of the textured Si surface after complete removal of the oxide layer is shown in the SEM image of Fig. 7.5. As can be seen in the Figure, homogeneous Si texturing with hemispherical etch-pits has been obtained. Under the oxide mask, through random defined pores, the etching rates in different orientations are the same, resulting in the formation of a hemispherical structure.

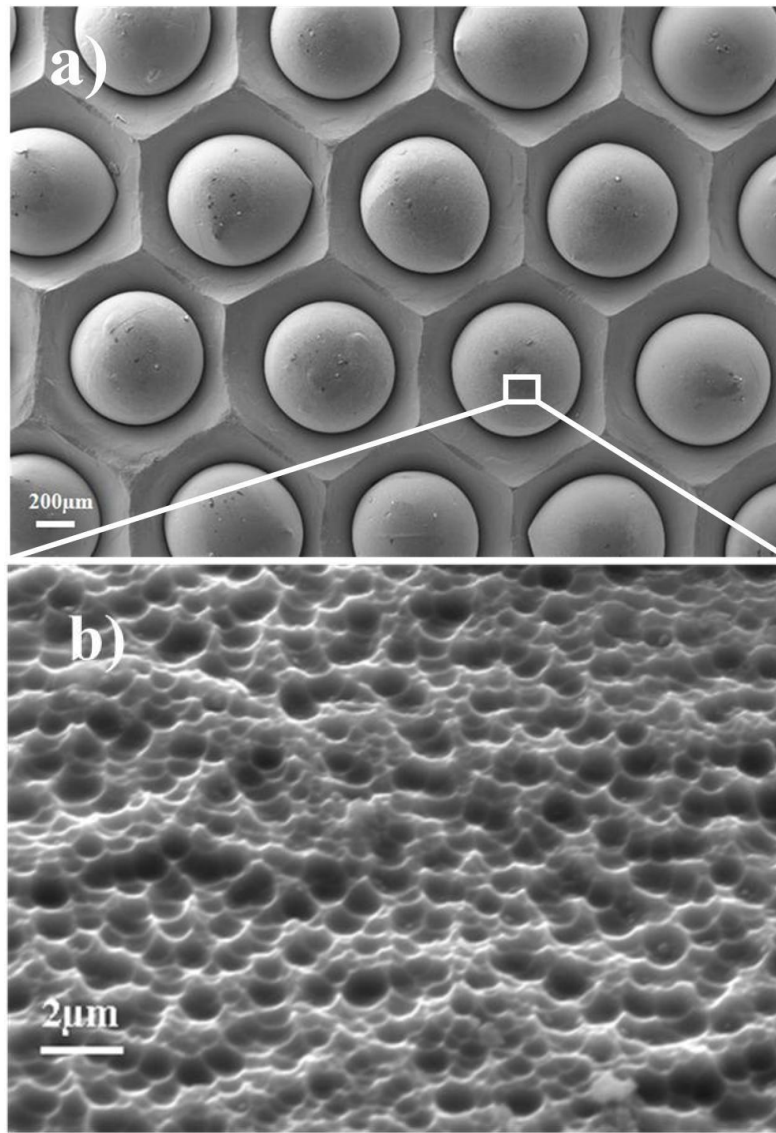


Figure 7.5: SEM image of the Si surface after removal of the LPD oxide layer showing the homogeneous texture on the Si surface

AFM studies performed on the textured Si surface revealed etch-pits of up to 1.5 μm in size and 0.7 μm in depth (Fig. 7.6). The inverted hemispherical texturing was also confirmed, which is an efficient texturing to not only minimize the reflectance but also increase the effective optical thickness in photovoltaic devices. Fig. 7.7 shows the 2-D AFM image of hemispherical structures on the silicon surface.

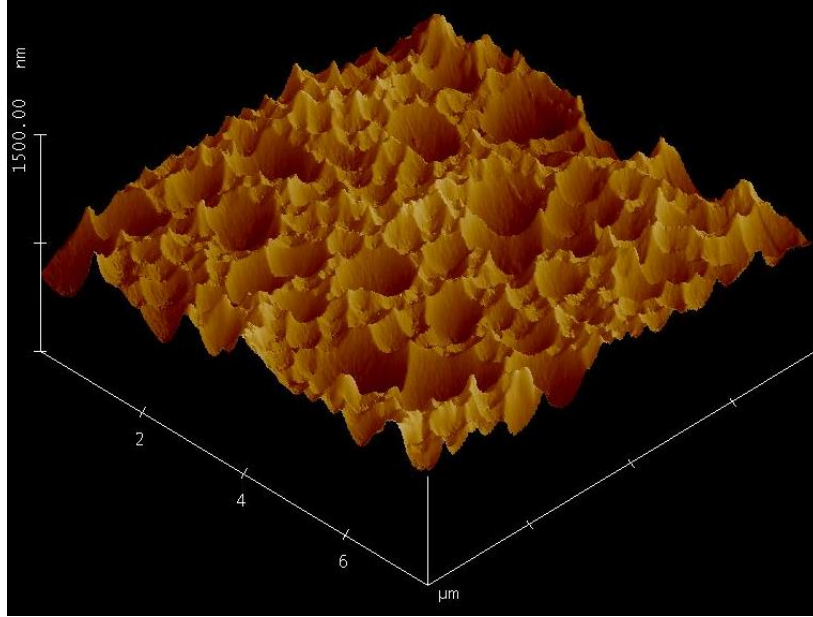


Figure 7.6: AFM image of the textured silicon after oxide removal.

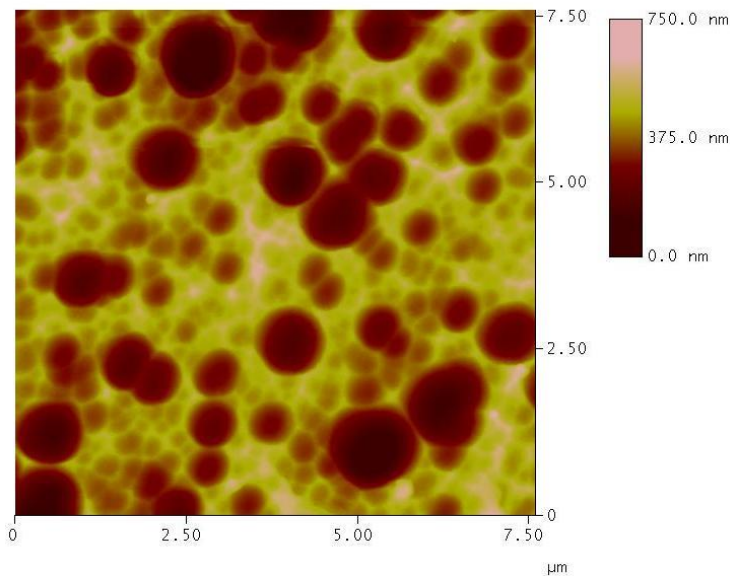


Figure 7.7: 2-D AFM image showing hemispherical structures on the silicon surface. Etch-pits of up to 1.5 μm in size and 0.7 μm in depth were revealed.

7.3 Transmission electron microscopy study

Since there is no previous study on the electrochemical etching of silicon using H_2SiF_6 , detailed investigation is necessary to reveal the nature of nanotexturing as well as the mechanism of the etching. In order to study the nature of nanotexturing as well as the elemental properties of the LPD oxide, transmission electron microscopy studies were performed. Cross-sectional TEM

samples from the nanotextured surface before and after the removal of the LPD oxide were prepared. Fig. 7.8 shows the cross-section TEM sample preparation from the surface of the silicon spheres using focused ion beam (FIB) technique. Fig. 7.8(a) shows the carbon layer deposited ion-beam to protect the surface from ion milling. Using a high beam current (gallium ion beam), two trenches are formed on both sides of the carbon layer (Fig. 7.8(b) and (c)). In order to prevent damaging of the area of interest, ion milling is continued with a low current beam to obtain a thickness of about 1 μ m. After this step, Frame Cuts are created and the membrane is polished to the level of electron transparency (~50 to 100nm). Using a glass needle and a micromanipulator, the membrane is removed and attached to a TEM grid (Fig. 6.8(d)). However for the preparation of the sample with the LPD mask, prior to the FIB preparation process, a thin layer of aluminum was deposited onto the surface using an e-beam system. This Al layer will protect the surface of the layer from any damage during carbon ion-beam deposition.

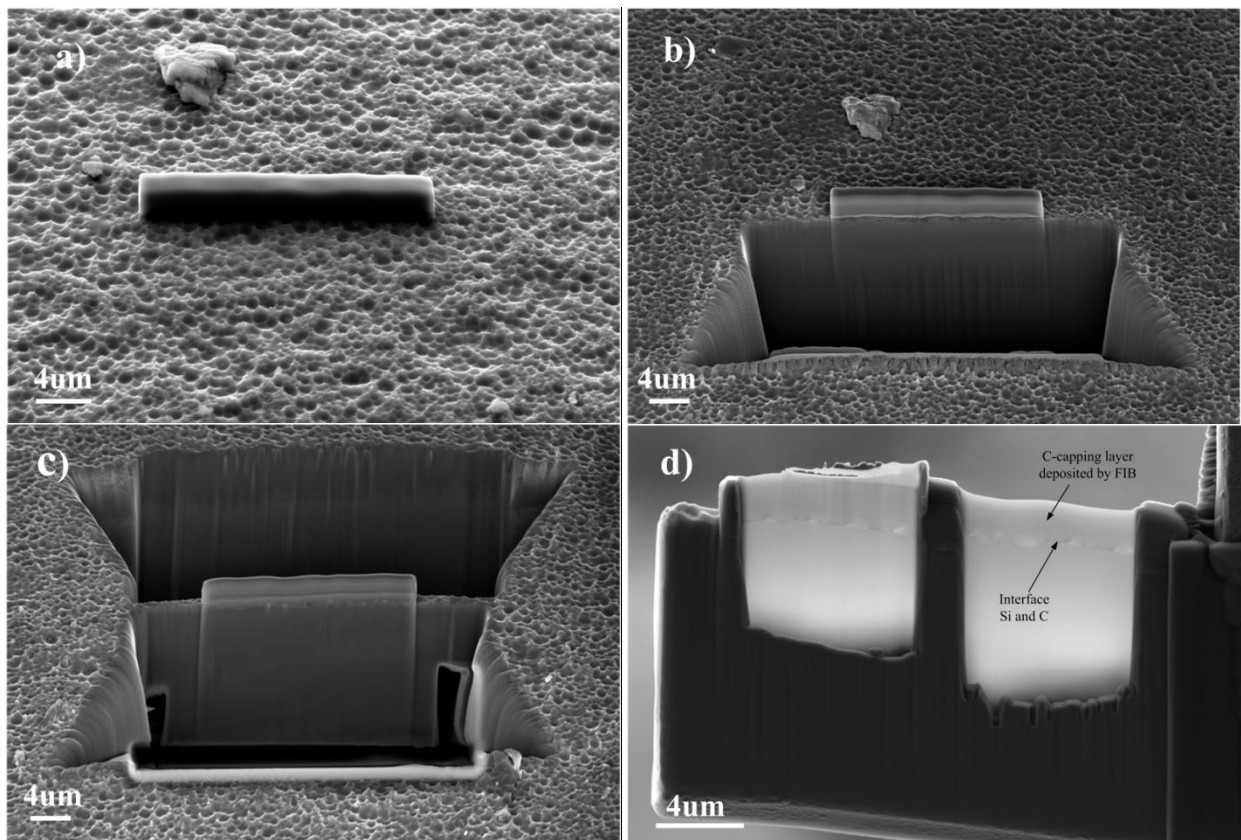


Figure 7.8: Preparation steps of TEM sample from nanotextured surface of silicon using focus ion beam technique (FIB-prepared cross-section for TEM imaging).

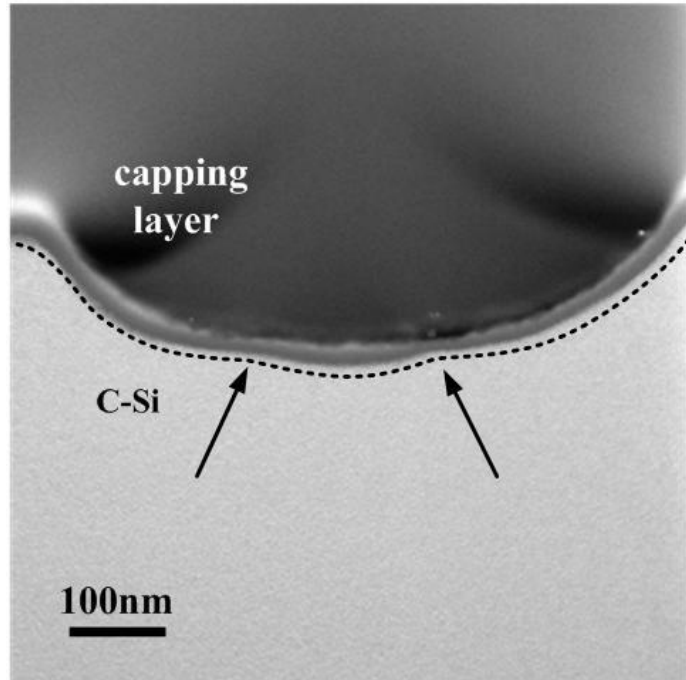


Figure 7.9: Scanning TEM image of an isotropic etch-pit from the surface of the nanotextured Si. No pore formation or branching was observed.

The cross sectional TEM analysis performed on the samples revealed the isotropic nature of the texturing and no pore formation was observed (Fig. 7.9). Therefore, the mechanism of this nanotexturing is different to porous silicon formation. In the PS formation process, random pores are formed on the surface of the silicon by dissolution of Si atoms in an HF solution. The depletion region formed around these pores, restricts the hole injection process from bulk Si and branching continues from the tip of the pores. The arrows in this figure are indicating that the etch-pit is formed by the merging of the smaller etch-pits, which corresponds to the nature of the isotropic etching of silicon.

Fig. 7.10 shows the cross-sectional bright-field TEM image of the silicon, oxide mask and Al-capping layer for surface protection from FIB-induced damage. The dashed-line (which is parallel to the Si surface) shows the interface of deposited Al and oxide mask. However, due to the high porosity of the LPD oxide mask, Al is diffused to the oxide layer and there is no clear interface between Al and the LPD oxide mask. As can be seen in this figure, a thin layer of oxide is formed directly on the surface of silicon and a thicker layer has just covered the etch-pit.

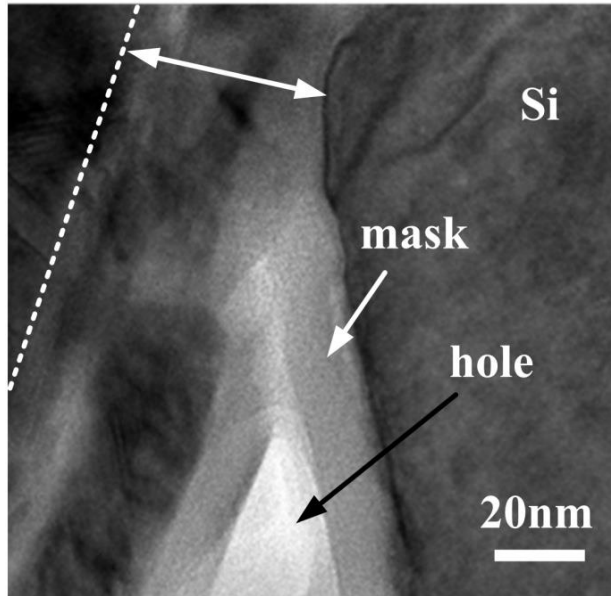


Figure 7.10: The cross-sectional bright-field TEM image of silicon, oxide mask and Al capping layer for the surface protection from FIB-induced damage.

The solution can reach the surface of the Si through the micro-pores in the oxide layer and the Si texturing and LPD oxide deposition simultaneously occurs. Fig. 7.11 shows the high-resolution TEM image of the silicon/oxide mask interface indicating that no pore formation process has occurred. Therefore, the etching mechanism is different to the porous silicon formation process.

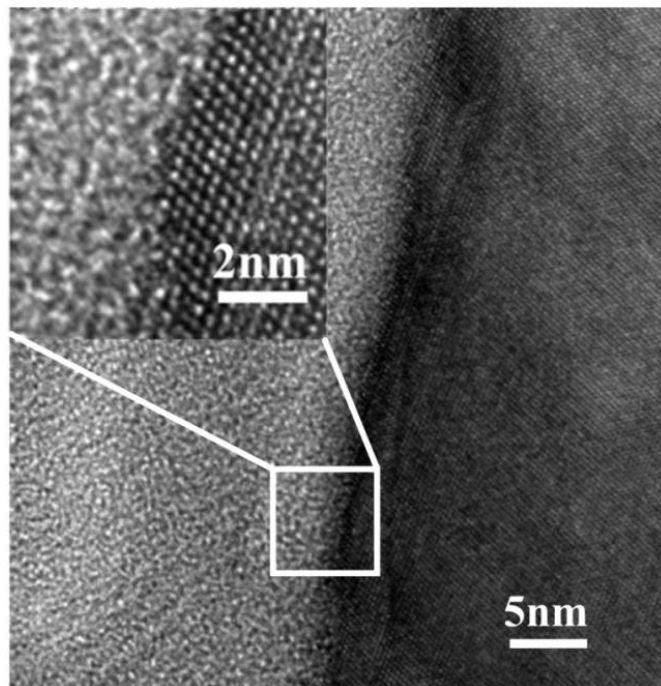


Figure 7.11: High-resolution TEM image of silicon/SiO_x interface (no pore formation was observed).

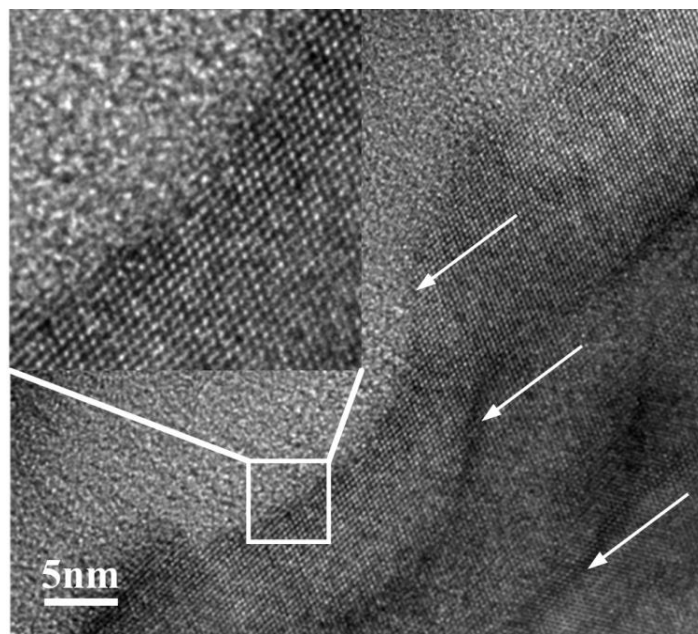


Figure 7.12: High-resolution TEM image showing the formation of very small etch-pits on the Si surface.

On some parts of the sample formation of very small etch-pits was observed which is shown in Fig. 7.12. The scanning TEM image of the SiO_x layer formed on the summits of the textured surface is shown in Fig 7.13. As can be seen in this figure, a thick layer of silicon oxide is formed on the summit, acting as a mask during the etching process. Assuming two competing mechanisms exist during the texturing process, etching and deposition of LPD oxide, the isotropic etching of silicon can be explained based on a higher deposition rate of LPD oxide on the summits. By initiation of the reactions, random etch-pits are formed on the surface of silicon and subsequently, summits are covered by an LPD oxide mask and isotropic etching continues inside the etch-pits. In order to investigate the elemental composition of the LPD mask, EDX analyses were carried out. In this image, the mask layer is highlighted by dashed-lines (in the inset) and the arrow shows the direction of the EDX line scan. The spectra show the EDX line scan for oxygen and silicon along the arrow.

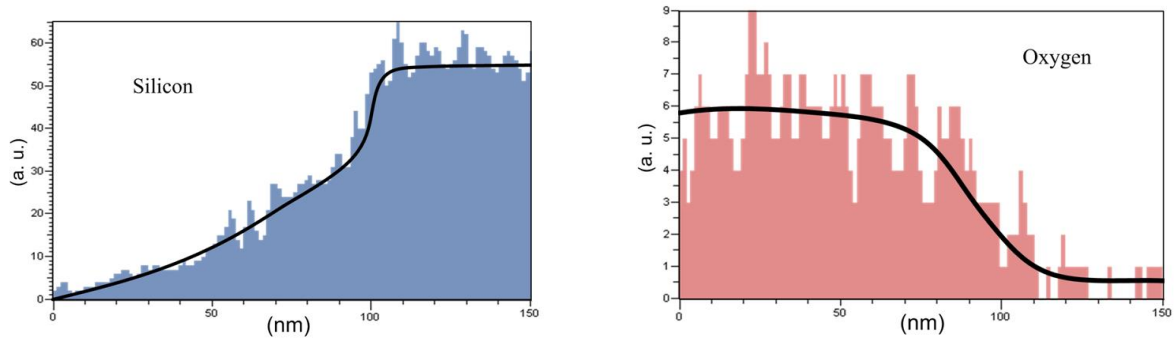
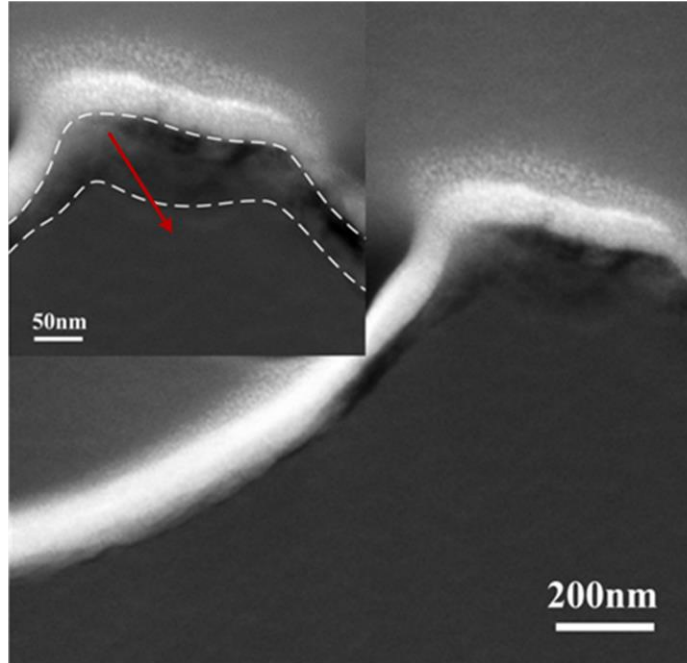


Figure 7.13: Scanning TEM image of mask layer formed on the summits of textured surface. The mask layer has been highlighted by dashed-lines in the inset and the arrow shows the position of the EDX line scan. The spectra show the EDX line scan for oxygen and silicon along the arrow.

Fig. 7.14 shows the SEM image of the Si textured surface showing a pentagonal (symmetric) etch-pit with sub-wavelength dimensions. The mechanism of the formation of this pentagon is explained using the schematic. The etching starts through the generated holes in the liquid phase mask layer deposited at the initial stage of the etching. Isotropic etching of silicon through these holes and simultaneously deposition of LPD SiO_x results in the formation of the pentagonal texture.

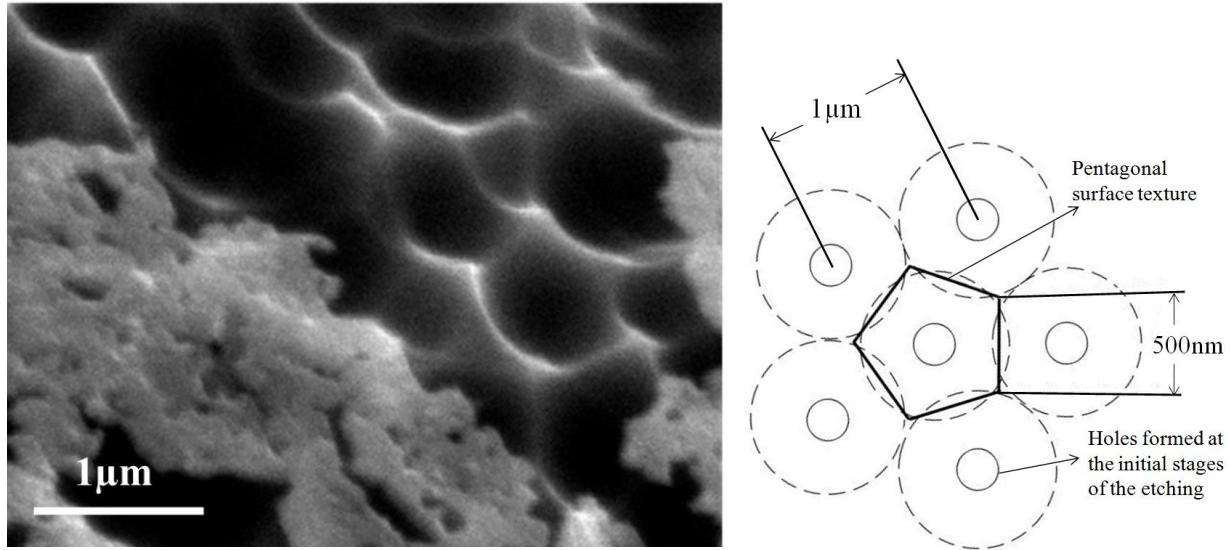


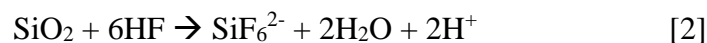
Figure 7.14: (Left) SEM image of the Si textured surface showing a pentagonal (symmetric) etch-pit with sub-wavelength dimensions. (Right) the schematic shows generated holes in the mask layer at the initial stage of the etching. The etching continues through these holes and a pentagonal surface texture is created.

7.4 Etching mechanism and chemical reactions

Different LPD techniques, such as immersing silicon wafers in saturated hydrofluorosilicic acid (H_2SiF_6)^{114,115} and anodic oxidation in diluted H_2SiF_6 solution^{106, 107} have been investigated for silicon oxide growth. The chemical reaction responsible for LPD oxide growth has been proposed as follows:^{116, 117}

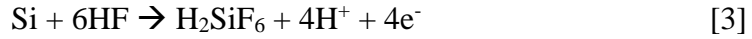


However, due to the HF content of the solution, etching of SiO_2 may occur during the oxide growth. Thus, there are two competing mechanisms during the liquid-phase oxide deposition. Since we are not using a saturated H_2SiF_6 acid solution, it is supposed that the oxide etch rate in this method is higher than in LPD oxide methods. The etching of SiO_2 occurs due to the following chemical reaction:¹¹⁸



The oxide etching and the hydrogen bubbles released from the surface of Si during the Si texturing are responsible for the rough surface and the micro-pores in the oxide layer. As discussed in Chapter 2, in the electrochemical etching process, if the current density exceeds a critical value (electropolishing threshold) the anodization results in complete removal of the Si

and smoothing of the surface.^{119, 120} However, in our method the LPD oxide acts as a mask for the eletropolishing process resulting in isotropic etch-pits formation. The chemical reaction for electropolishing can be written as:



The by-product of Si dissolution in Hydrofluoric acid (HF) is H_2SiF_6 acid. The solution reaches the surface of the Si through the micro-pores in the oxide layer and the Si texturing and LPD oxide deposition simultaneously occurs. H_2SiF_6 acid, as a by-product of Si etching, shifts the Eq. 5 to right and the hydrogen production shifts the Eq. 6 to the left, both resulting in a higher oxide deposition rate.

7.5 Reflectance characteristics and external quantum efficiency of silicon spheres with hemispherical nanopit texturing

The schematic of silicon spheres with hemispherical nanopit texturing on the emitter is depicted in Fig. 7.15. As can be seen in this image, nanotexturing is performed on the emitter and the emitter is not yet removed. Development of a texturing method that can be applied as a post process to form a selective emitter structure has potential applications in optoelectronic and photovoltaic devices. This texturing method requires removal of less than 0.5um from the surface of the emitter, while creating an efficient texturing to suppress the reflectivity.

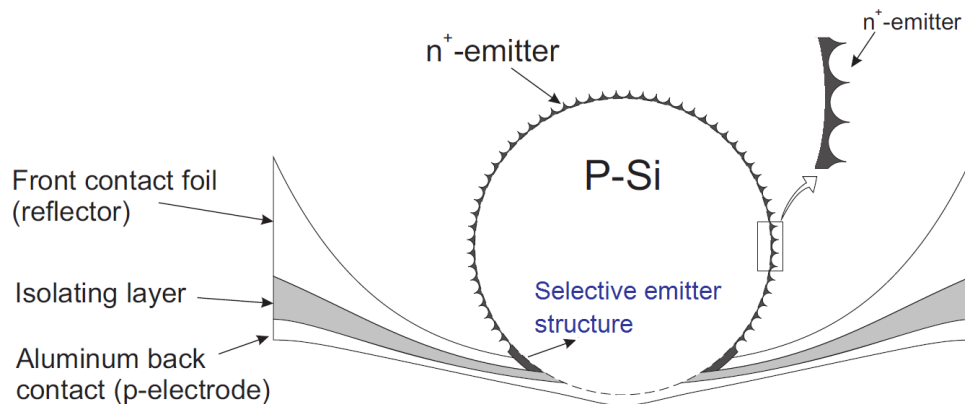


Figure 7.15: Schematic of silicon spheres with hemispherical nanopit texturing on the emitter. Nano-texturing of silicon spheres with a diffused emitter results in selective emitter solar cells.

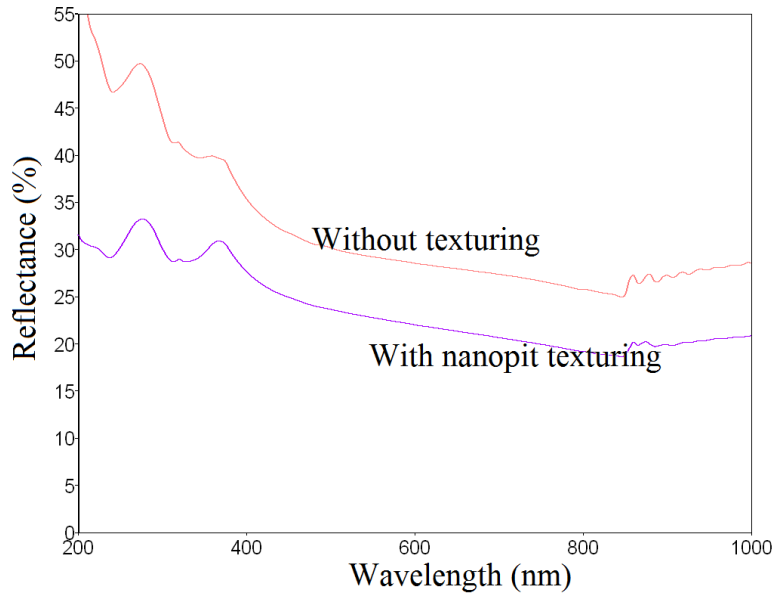


Figure 7.16: Reflectance characteristics of spherical silicon solar cells integrated with hemispherical nanopit texturing.

Fig. 7.16 shows the reflectance spectra of spherical silicon solar cells integrated with hemispherical nanopit texturing. The Spectral response measurements of spherical silicon solar cells with integrated hemispherical nanopit texturing are collected in Fig. 7.17. The EQE of spherical silicon solar cells integrated with nanopit texturing showed improvement in the whole range of spectral response. However, the less improvement observed in the UV region is attributed to the increase effect of surface recombination in shallow emitter structure.

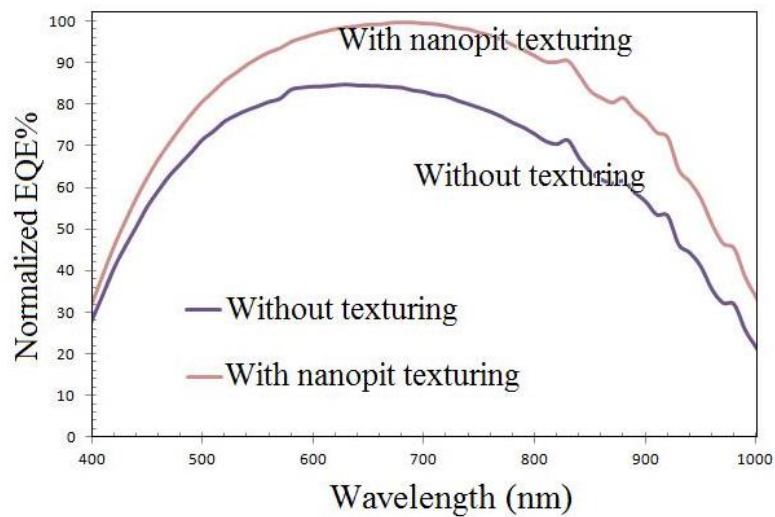


Figure 7.17: Spectral response measurements of spherical silicon solar cell with integrated hemispherical nanopit texturing.

7.6 Conclusion

We developed a novel technique of electrochemical etching for silicon surface texturing using a liquid-phase deposition of oxide mask. An aqueous solution of hydrofluorosilicic acid (34%) and ethanol was used as an electrochemical etching electrolyte. During the anodization process, two reaction mechanisms of the silicon etching and the deposition of SiO_x , simultaneously occur. The liquid phase deposited SiO_x acts as a mask on the surface of the silicon and hemispherical nanopits are formed by isotropic etching through the holes in this mask. The obtained nanotextured surface is considerably uniform and the etching rate can be successfully controlled. Using a focus ion-beam (FIB) technique, cross-sectional TEM samples were prepared to investigate the nature of texturing and the composition of the deposited mask. The hemispherical nanopit texturing was successfully integrated into spherical silicon solar cells and the etching mechanisms and the chemical reactions were discussed. The spectral response and reflectance characteristic of silicon spheres integrated with nanopit texturing were studied.

Chapter 8

Integration of colloidal quantum dots into spherical silicon solar cells

8.1 Introduction

When the dimensions of quantum dots(QDs) is reduced to less than several nanometers in the range of the Bohr radii, quantum dots exhibit discrete and tunable structure in their optical and electrical characteristics. Due to the quantum confinement effects, QDs exhibits remarkable size-dependent physical properties. The absorption spectrum of colloidal quantum dots integrated into functional oxides, dielectric matrix, etc. can be easily matched to the spectrum of the sun's energy reaching the earth. Colloidal quantum dots can be deposited by various methods, such as dip-coating, spin-coating, or inkjet printing on silicon, glass or flexible substrates. Next generation photovoltaic technology based on quantum dots and concepts such as down-conversion and down-shifting is promising significant increases in conversion efficiency. However, until now, there is no experimental evidence of fabricating solar cells with higher efficiencies than current generation photovoltaic solar cells. The concept of down-conversion is based on utilization of high energy photons to produce two or more low-energy photons (ideally

above the band gap silicon) and down-shifting improves the performance of the solar cells by shifting the short wavelength photons to lower energy photons for which the quantum efficiency is higher.

Therefore, investigation and development of methods for the integration of quantum dots (QDs) to silicon solar cells may lead to photovoltaic devices which can harvest the solar energy more efficiently. We have studied different methods of processing and embedment of colloidal QDs into metal oxide layers. Since a simple method of the deposition of quantum dots is spin-coating, in the first approach we try to arrange different QDs in a monolayer form using a spin-coating process. Subsequently, in order to encapsulate the QDs, a metal oxide layer is deposited on the monolayer of QDs using electron-beam technique. In another approach, CdSe colloidal quantum dots are processed into a graded-density nanoporous layer using an ultrasonic system. In this method by immersion of the nanoporous layer in the solution of quantum dots with proper size, the quantum dots are dispersed in the pores of the n-PS layer. This method was successfully applied to the spherical silicon solar cells. Since the first approach is based on spin-coating technique, due to the shape of silicon spheres and aluminum reflector, it is difficult to be applied to spherical silicon solar cells.

We successfully fabricated a QDs-embedded layer by processing colloidal QDs into a graded-density nanoporous silicon layer. This structure is implemented on top of the emitter of the spherical silicon solar cells and the spectral response with and without incorporation of QDs was studied. However, the promising efficiency improvement that the theory of quantum dots predicted was not observed but absorption of optically active quantum dots, along with the enhancement of high-energy photons conversion efficiency was observed.

8.2 Characterization of colloidal QDs and deposition of closed-packed QDs monolayer encapsulated by metal oxide layers

Commercial colloidal quantum dots including CdSe stabilized by octadecyl amine (ODA) ligands, CdSe/ZnS stabilized by ODA ligands and PbS stabilized by oleic acid ligands, were used in this research. The luminescence quantum efficiency of these quantum dots is about 20 to 30%. The CdSe quantum dots coated with ZnS shell are showing higher quantum efficiency as

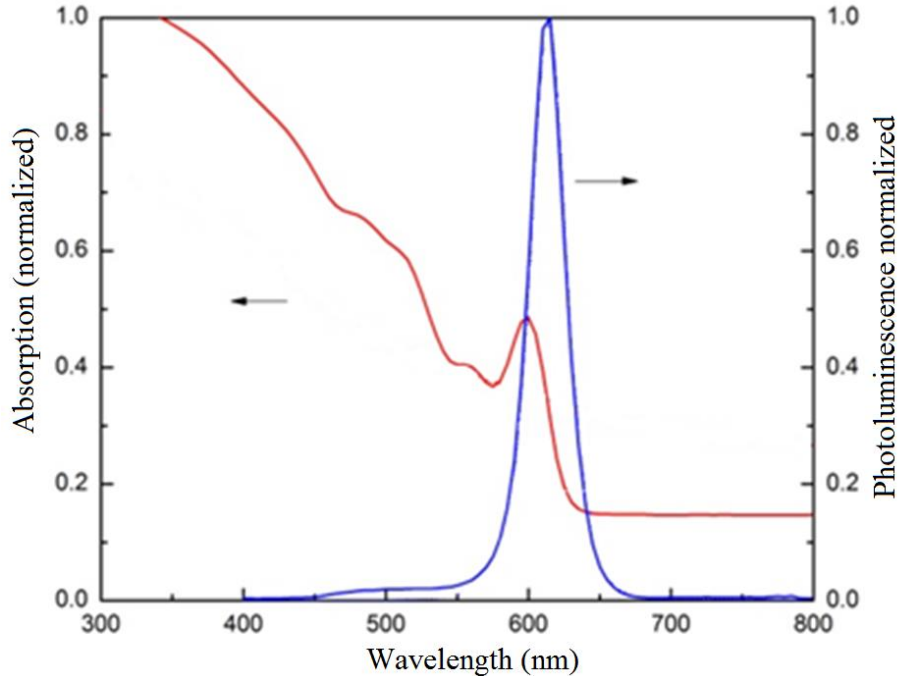
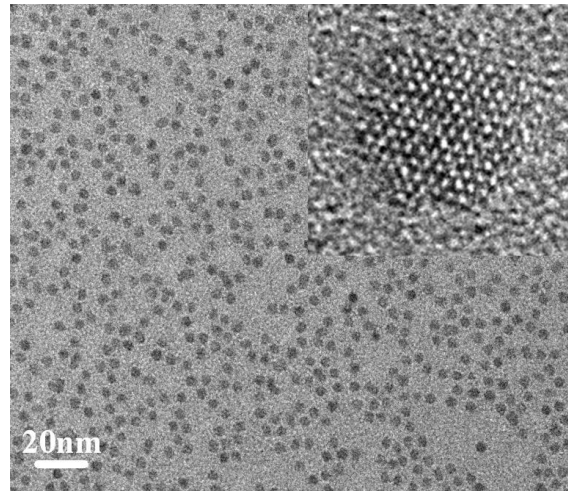


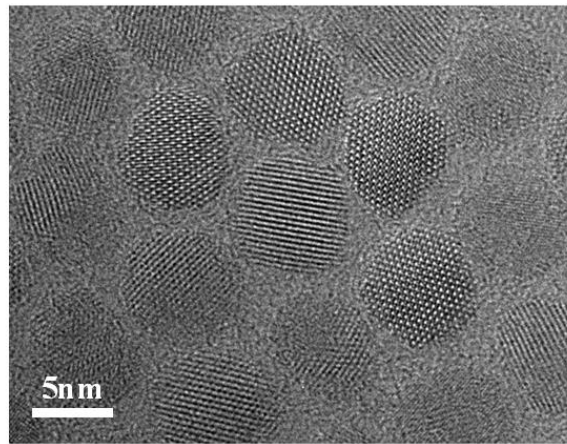
Figure 8.1: Emission and absorption peaks of CdSe quantum dots with size of about 5nm.

compared to CdSe stabilized by octadecyl. ZnS shell with the same crystalline structure as CdSe, provides an efficient passivation of defects on the surface of the quantum dot resulting in higher luminescence quantum efficiency. The bandgap of CdSe QDs and the emission peak can be tuned by adjusting the radius of the nanoparticles. The CdSe quantum dots with different sizes from 2nm to 6nm emit wavelengths from blue (480nm) to red (630nm), in the visible range of spectral response. Fig. 8.1 shows the emission and absorption spectra of CdSe quantum dots with size of about 5nm. As can be seen in this graph, the emission and absorption peaks are close to each other and CdSe QDs absorb wavelengths below the local maximum of the absorption peak. With excitation wavelengths in high-energy photon region and emissions in high-conversion EQE region, CdSe QDs are potential candidate for integration into crystalline silicon solar cells.

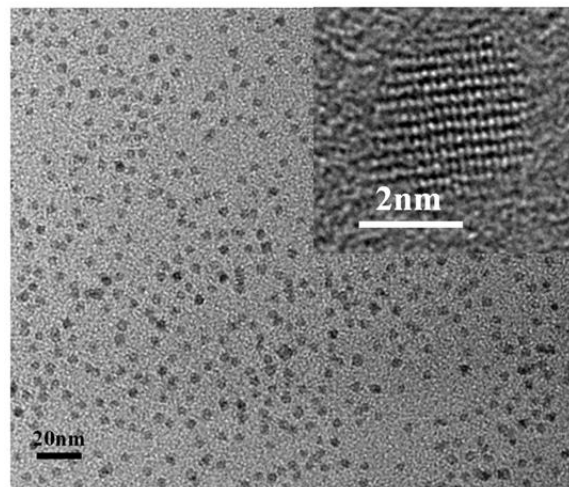
In order to investigate the crystalline structure, arrangement and size distribution of colloidal QDs, TEM studies were performed. Colloidal quantum dots were spin coated onto the thin film carbon TEM grids, using spin-coating technique. By control the concentration of quantum dots solution and spin-coating process, uniform monolayers were obtained. However, to obtain the optimum condition many experiments were performed, each involved TEM study. Fig. 8.2 shows the HR-TEM images of different colloidal QDs spin-coated on the thin-film carbon grids. Fig. 8.2(a) shows the TEM image of CdSe quantum dots with diameter of about 4.8nm. The inset



(a)



(b)



(c)

Figure 8.2: (a) HR-TEM image of CdSe quantum dots with diameter of 4.8nm. The inset shows an individual nanoparticle with wurtzite crystalline structure. (b) Transmission electron micrograph of CdSe/ZnS nanoparticles exhibiting different crystallographic orientations. The ZnS shell is about 1.6nm. (c) HR-TEM image of CdS quantum dots with diameter of about 3nm.

shows an individual nanoparticle with wurtzite crystalline structure. As seen in this image, QDs are separated and no agglomeration was observed. Fig. 8.2(b) illustrates the TEM micrograph of CdSe/ZnS nanoparticles with different crystallographic orientations. The ZnS shell is about 1.6nm. However, since the crystalline structure of the ZnS shell and CdSe are similar, no clear interface can be observed. This indicates that ZnS is an efficient coating to passivate the vacancies and defects on the surface of the CdSe nanocrystal. The HR-TEM image of CdS quantum dots with diameter of about 3nm is shown in Fig. 8.2(c).

However, monolayer of CdSe quantum dots were obtained but close-packed structure was not observed in large area. The close-pack monolayer structure was only obtained in PbS quantum dots stabilized by oleic acid ligands. Fig. 8.3(a) shows the bright-field TEM image of PbS quantum dots arranged in a close-packed monolayer using a spin-coating process. The closed-pack structure was observed on the large areas of about $1 \times 1 \text{mm}^2$. Transmission electron diffraction (TED) pattern of PbS QDs is shown in Fig. 8.3(b). Random distribution of PbS nanoparticles with no preferred orientation can be observed. Scanning TEM image of PbS quantum dots on a TEM grid is illustrated in Fig. 8.3(c). The inset shows an individual nanoparticle with $\langle 220 \rangle$ orientation. In order to encapsulate the PbS quantum dots, a thin layer of tantalum oxide were deposited on the monolayer of PbS QDs. The scanning TEM image of PbS quantum dots with a diameter of 5.4nm, capped in an ultra thin film of tantalum oxide is shown in Fig. 8.3(c). As seen in this image, quantum dots are still arranged in a close-packed monolayer form after the e-beam deposition. Fig. 8.4 shows EDX analysis of the closed-packed monolayer of PbS quantum dots covered with ultra thin layer of ($\sim 3\text{nm}$) Ta_2O_5 . Mo and C are from TEM grid. Through this method, multilayer of QDs/metal oxide can be obtained. However, this method consists of several deposition steps and cannot easily be applied to non-planar substrates.

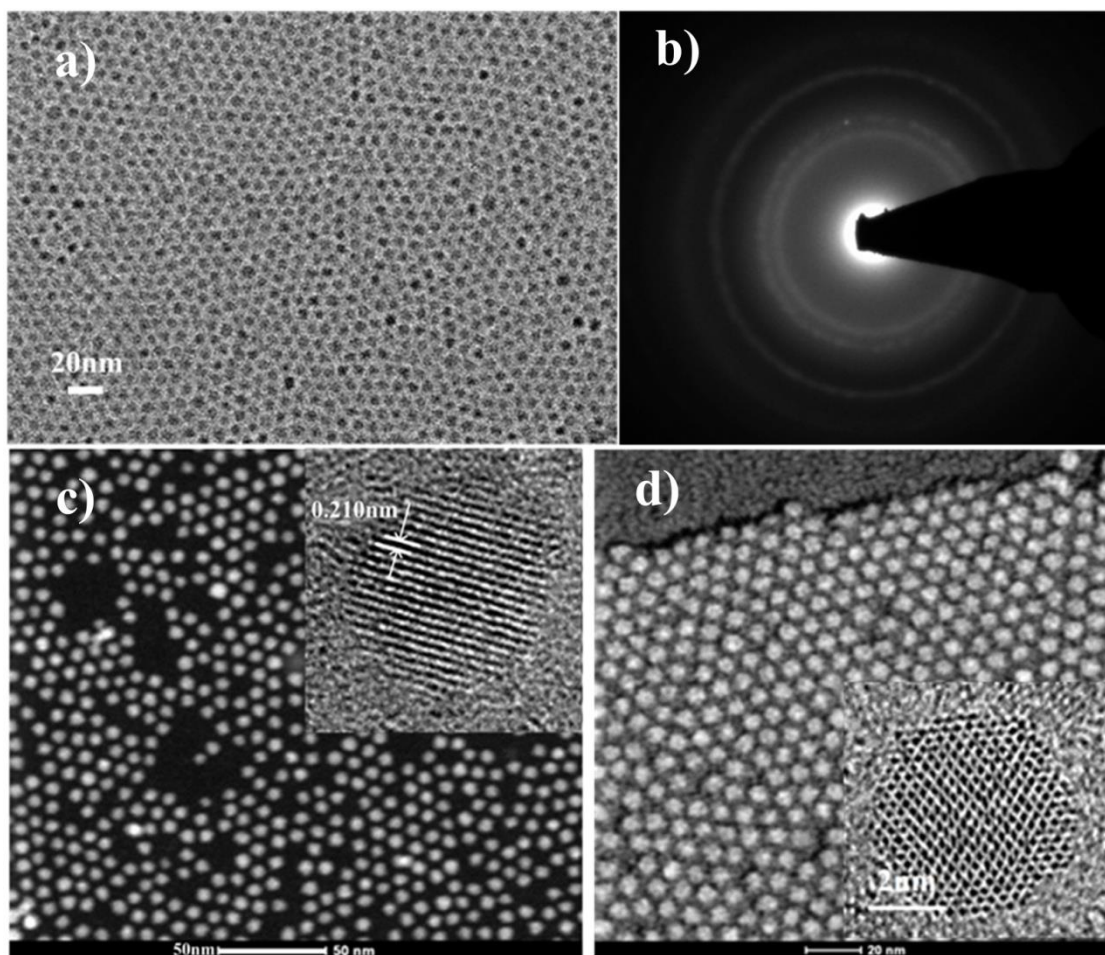


Figure 8.3: (a) Bright-field TEM image of PbS quantum dots arranged in a close-packed monolayer form using a spin-coating process. (b) Transmission electron diffraction (TED) pattern of PbS QDs. (c) Scanning TEM image of PbS quantum dots on a carbon TEM grid. The inset shows an individual nanoparticle with $\langle 220 \rangle$ orientation. (d) Scanning TEM image of PbS quantum dots with a diameter of 5.4 nm, capped in an ultra thin film of tantalum oxide.

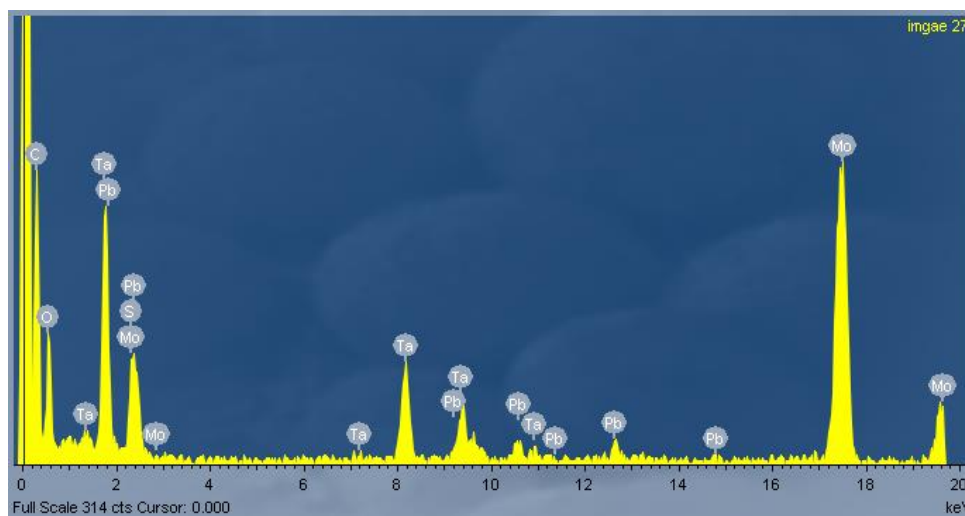


Figure 8.4: EDX analysis of closed-packed monolayer of PbS quantum dots covered with ultra thin layer of (~ 3 nm) Ta_2O_5 . Molybdenum is from TEM grid.

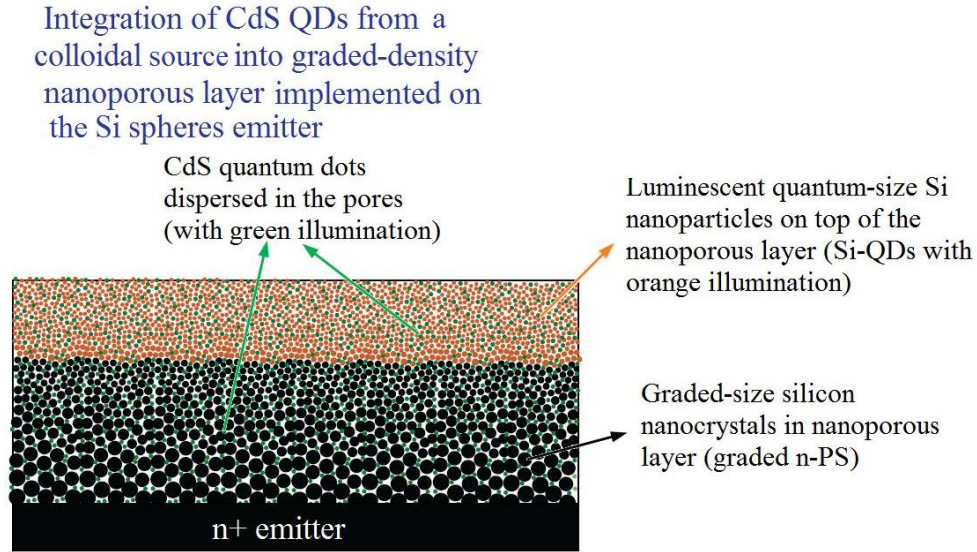


Figure 8.5: Incorporation of colloidal QDs into graded-density nanoporous layer.

8.3 External quantum efficiency of spherical silicon solar cells integrated with colloidal CdSe-QDs

We successfully fabricated a QDs-embedded layer by processing colloidal QDs into a graded-density nanoporous silicon layer (Fig. 8.5). Proper concentration of CdS quantum dots in toluene solution has been prepared and spherical silicon solar cells with nanoporous layer were immersed in the solution using an ultrasonic system. The CdS quantum dots are dispersed in the pores of nanoporous Si structure. Subsequently, the cell is washed in toluene solution to remove the CdS quantum dots participated on the surface of the nanoporous layer. As TEM studies in Chapter 6 revealed, the pore size of the graded-density n-PS is about 5 to 10nm. Therefore, CdSe quantum dots with a diameter of about 2.8nm are suitable candidate for dispersion in n-PS structure. The HR-TEM image of CdSe quantum dots used for dispersion into nanoporous silicon matrix is shown in Fig. 8.6. Different crystallographic orientations can be seen in this image and the size distribution is very uniform. The emission and absorption peaks of these QDs are at wavelengths of 545nm and 580nm, respectively. The emission peak (580nm) is positioned at high-conversion-efficiency region of the spectral response of spherical silicon solar cells. The spectral response of spherical silicon solar cells with and without incorporation of CdS-QDs is collected in Fig. 8.7.

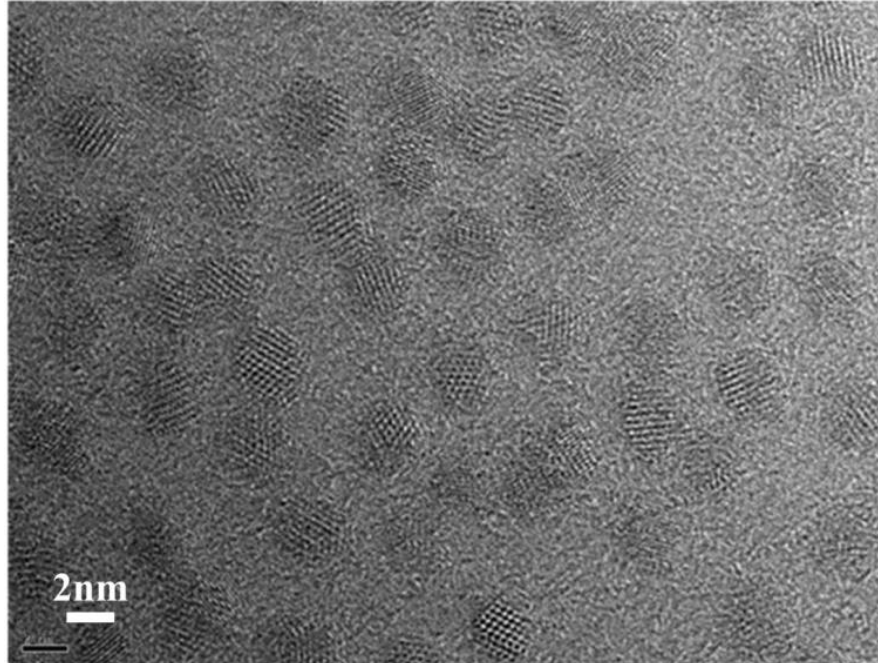


Figure 8.6: High resolution TEM image of CdSe quantum dots with diameter of about 2.8 nm.

The EQE spectrum of spherical silicon solar cells integrated with CdSe QDs exhibited a local minimum at the wavelength of about 540nm. The wavelength corresponds to the absorption peak of the CdSe quantum dots (545nm) indicating that these QDs are optically active in the matrix of n-PS. Although CdSe quantum dots absorb at all wavelengths below the absorption peak (Fig. 8.1), no change in the high energy region (wavelengths below the absorption peak) of the spectrum was observed. This is attributed to the down-shifting properties of CdSe QDs, red-

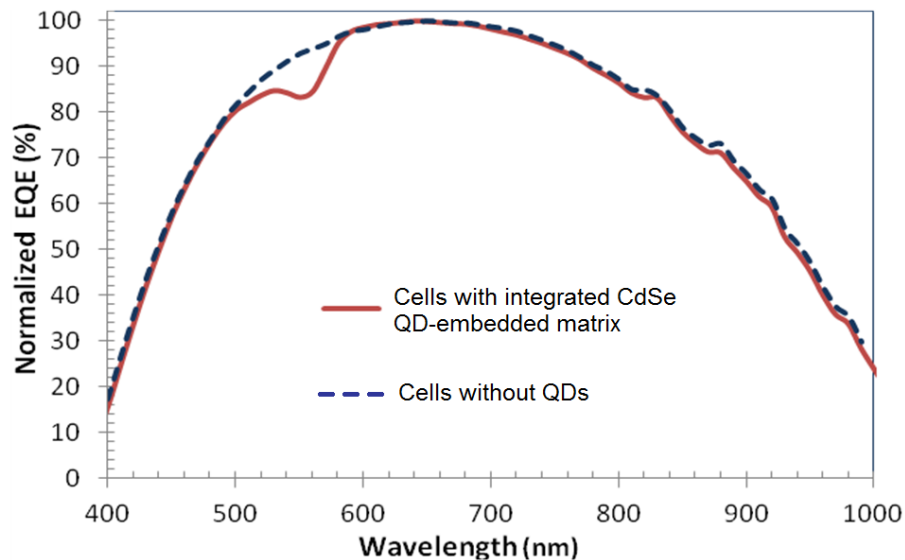


Fig. 8.7: External quantum efficiency spectra of spherical silicon cells integrated with CdSe QDs-embedded layer. The absorption and emission peaks of CdSe QDs are at wavelengths of 545nm and 580nm, respectively.

shifting the high energy photons to the wavelengths with higher quantum efficiency; and therefore, compensating the absorption. This can be the proof of the concept of down-shifting in CdSe QDs integrated into crystalline silicon solar cells. However, the luminescence quantum efficiency of the CdSe QDs used in this work was about 20%. Using QDs with higher efficiency and also employing efficient optical-capping layers to prevent the escape of re-emitted photons, would further improve the effect of down-shifting.

8.4 Conclusion

Colloidal quantum dots including CdSe stabilized by octadecyl amine (ODA) ligands, CdSe/ZnS stabilized by ODA ligands and PbS stabilized by oleic acid ligands, were characterized. Assembly and arrangement of these quantum dots in a close-packed monolayer form was studied. CdSe quantum dots with diameter of about 2.8 nm were successfully integrated into a graded-density nanoporous layer. This structure is implemented on the emitter of spherical silicon solar cells and the spectral response with and without incorporation of QDs was studied. The concept of down-shifting in CdSe QDs integrated into crystalline silicon spheres was discussed.

Chapter 9

Conclusion

The material properties of silicon spheres, which were studied, included surface morphology, crystallinity, lattice structure, microwave photoconductivity decay lifetime, and impurity elemental distributions. The crystallinity of silicon spheres was investigated by means of a single-crystal X-ray diffractometer and a x-ray powder diffraction (XRD) machine. Most of the x-ray spectra collected by the x-ray powder diffraction (XRD) method, revealed only one peak or no peaks were observed in the x-ray pattern. This indicates that silicon spheres do not contain polycrystalline silicon and the structure is single-crystal or multi-crystal. 2D diffraction patterns obtained by the Single-crystal XRD method illustrate twin-crystal reflections from silicon spheres. TEM studies on the crystallinity of silicon spheres verify the result from x-ray diffraction analyses. Elemental distribution was studied using the SIMS imaging technique. Photoconductivity decay technique was used to obtain the carrier recombination lifetime in silicon spheres. Based on microwave reflection photoconductivity decay measurements, the average minority carrier lifetime in the silicon spheres varies from 0.2 to 1 μ s.

Silicon nitride antireflection coating layers were developed and deposited onto spherical silicon solar cells, using a PECVD system. By control of the plasma condition (gas flow ratio, power and pressure) dark-blue SiN_x coated spheres were obtained. It was observed that silicon nitride layers deposited onto flat silicon wafers and silicon spheres, under the same plasma condition, exhibited different properties. This is attributed to the shape of the silicon spheres and aluminum foil, changing the plasma condition at the surface of silicon spheres and hence producing different SiN_x layers. A low temperature hydrogenation plasma technique was developed to improve the passivation quality of spherical silicon solar cells. The spectral response of silicon spheres with and without a silicon nitride antireflection coating has been studied.

We successfully developed and integrated a nanostructured antireflection coating layer into spherical silicon solar cells. The nanostructured porous layer consists of graded-size silicon nanocrystals and quantum-size Si nanoparticles embedded in an oxide matrix. This layer has been characterized by means of SEM, TEM, STEM, TED, EELS, EDX, Raman spectroscopy and photoluminescence spectroscopy (PL). Due to the quantum confinement effects, this ARC layer shows incredible properties such as enhanced luminescence, light trapping, photon-shifting and bandgap opening. Quantum-size silicon nanoparticles with dimensions less than 2nm showed significantly high luminescence in the visible range of spectral response. Band-gap opening in the emitter structure minimizes the absorption of photons in the dead layer and improves the spectral response. The external quantum efficiency of silicon spheres integrated with graded-density n-PS layers exhibited significant improvement in a wide range of the spectral response (Table 9.1). As compared to SiN_x single-ARC layers, the nanostructured PS layer suppresses the reflection in a wide range of spectral response. Furthermore, graded-density nanoporous silicon is selectively deposited onto the silicon spheres; however, the SiN_x layers are also deposited on aluminum foil degrading the performance of the Al reflector.

We developed a novel technique of electrochemical etching for silicon surface texturing using a liquid-phase deposition of oxide mask. During the anodization process, two reaction mechanism of silicon etching and deposition of SiO_x, simultaneously occur. The liquid phase deposited SiO_x acts as a mask on the surface of the silicon and hemispherical nanopits are formed by isotropic etching through the holes in this mask. Using a focus ion-beam (FIB) technique, cross-sectional TEM samples were prepared to investigate the nature of texturing and the composition of the deposited mask. The hemispherical nanopit texturing was successfully integrated into spherical silicon solar cells and the etching mechanisms and the chemical reactions were discussed.

Different methods of processing and embedment of colloidal QDs into metal oxide layers were studied. We successfully fabricated a QDs-embedded layer by processing colloidal QDs into a graded-density nanoporous silicon layer. The spectral response measurements with and without incorporation of QDs was studied. In the EQE spectrum, a local minium was observed at the same wavelength (545nm) as the absorption peak of the CdSe QDs, indicating optically active QDs. Photon-shifting properties of the CdSe QD-embedded layer were discussed.

Highlights in terms of device fabrications and improvement of the external quantum efficiencies are collected in table 9.1.

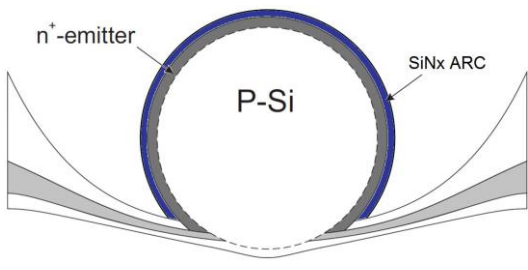
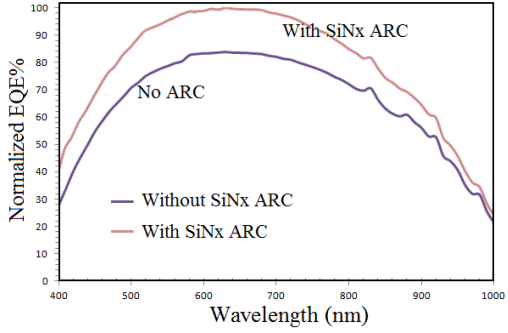
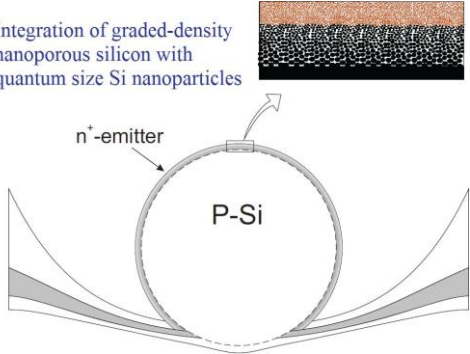
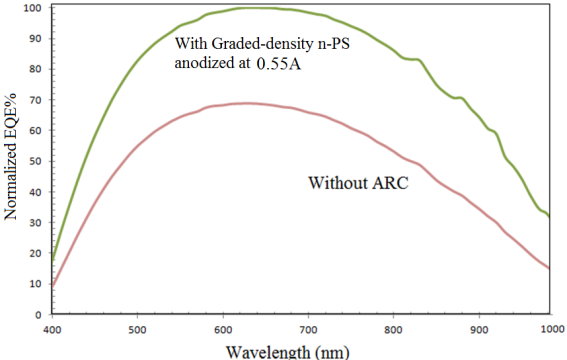
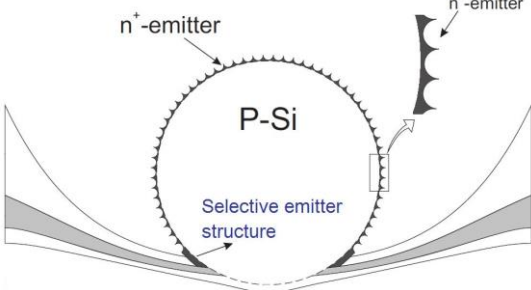
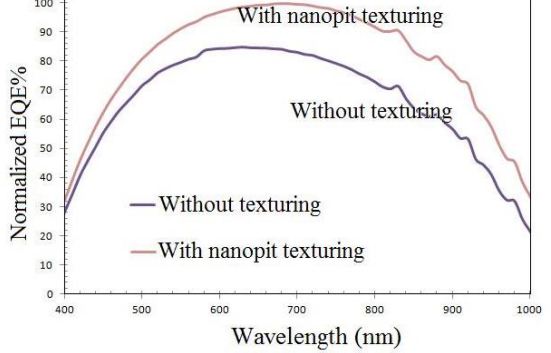
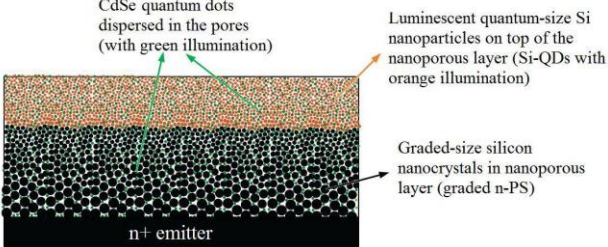
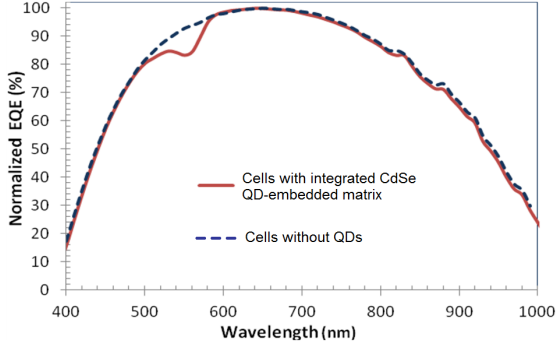
| Fabricated devices with integrated nanostructures and silicon spheres with SiN _x single-ARC layer | Improvement of external quantum efficiency (EQE) |
|--|--|
|  <p data-bbox="245 604 760 636">Silicon spheres with SiN_x single-ARC layer</p> |  |
| <p data-bbox="266 680 516 751">Integration of graded-density nanoporous silicon with quantum size Si nanoparticles</p>  <p data-bbox="196 1024 808 1056">Integration of graded-density n-PS with Si-QDs</p> |  |
|  <p data-bbox="233 1388 776 1419">Integration of hemispherical nanopit texturing</p> |  |
| <p data-bbox="217 1478 500 1570">Integration of CdSe QDs from a colloidal source into graded-density nanoporous layer implemented on the Si spheres emitter</p>  <p data-bbox="302 1829 711 1860">Integration of CdSe colloidal QDs</p> |  |

Table 9.1: Summary of the fabricated devices and the improvement of external quantum efficiency

References

1. M. Narayanan and T. Ciszek, Springer-Verlag, 1701 (2010).
2. H. J. Möller, C. Funke, M. Rinio, and S. Scholz, *Thin Solid Films* 487, 179 (2005).
3. A. Shah, P. Torres, R. Tscharnner, N. Wyrsh, and H. Keppner, *Science* 285, 692 (1999).
4. M. A. Green, *Prog. Photovoltaics* 9, 137 (2001).
5. J. Y. Kim, K. Lee, N. E. Coates, D. Moses, T. Q. Nguyen, M. Dante, and A. J. Heeger, *Science* 317, 222 (2007).
6. D. Wöhrle and D. Meissner, *Adv. Mater.* 3, 129 (1991).
7. L. Gur, N. A. Fromer, M. L. Geier, and A. P. Alivisatos, *Science* 310, 462 (2005).
8. B. Z. Tian, X. L. Zheng, T. J. Kempa, Y. Fang, N. F. Yu, G. H. Yu, J. L. Huang, and C. M. Lieber, *Nature* 449, 885 (2007).
9. L. E. Greene, M. Law, B. D. Yuhas, and P. D. Yang, *J. Phys. Chem. C* 111, 18451 (2007).
10. M. D. Kelzenberg, S. W. Boettcher, J. A. Petykiewicz, D. B. Turner-Evans, M. C. Putnam, E. L. Warren, J. M. Spurgeon, R. M. Briggs, N. S. Lewis, and H. A. Atwater, *Nat. Mater.* 9, 239 (2010).
11. Z. Liu, T. Nagai, A. Masuda, and M. Kondo, *J. Appl. Phys.* 101, 093505 (2007).
12. M. Gharghi, H. Bai, G. Stevens, and S. Sivoththaman, *IEEE Trans. Electron Devices* 53, 1355 (2006).
13. M. Biancardo, K. Taira, N. Kogo, H. Kikuchi, N. Kumagai, N. Kuratani, I. Inagawa, S. Imoto, and J. Nakata, *Sol. Energy* 81, 711 (2007).
14. J. D. Levine, G. B. Hotchkiss and M. D. Hammerbacher, 22nd *IEEE Photovoltaic Specialists Conf.* 2, 1045 (1991).
15. W. Keller and A. Muhlbauer, *Floating Zone Silicon*, Marcel Dekker Inc, ISBN 0-824-71167-x, (1981).
16. R. L. Lane, "The Czochralski Method for Photovoltaic Applications," in C. P. Khattak and K. V. Ravi, *Silicon Processing for Photovoltaics I, Materials Processing Theory and Practice*, vol. 5, pp.49-84, North-Holland, ISBN 0-444-86933-6, (1985).
17. S. Omae, T. Minemoto, M. Murozono et al, "Crystal Growth Mechanism of Spherical Silicon Fabricated by Dropping Method," *Japanese Journal of Applied Physics*, vol. 45, pp.3577-3580, (2006).

18. S. Omae, T. Minemoto, M. Murozono et al, "Crystal Characterization of Spherical Silicon Solar Cell by X-ray Diffraction," *Japanese Journal of Applied Physics*, vol. 45, pp.3933-3937, **(2006)**.
19. D. Hironiwa, T. Minemoto, C. Okamoto et al, "Phosphorous Gettering on Spherical Si Solar Cells Fabricated by Dropping Method," *Japanese Journal of Applied Physics*, vol. 45, pp.4939-4942, **(2006)**.
20. C. Okamoto, T. Minemoto, M. Murozono et al, "Defect Evaluation of Spherical Silicon Cells Fabricated by Dropping Method," *Japanese Journal of Applied Physics*, vol. 44, pp.7805-7808, **(2005)**.
21. C. Okamoto, K. Tsujiya, T. Minemoto et al, "Reduction in Dislocation Density of Spherical Silicon Solar Cells Fabricated by Decompression Dropping Method," *Japanese Journal of Applied Physics*, vol. 44, pp.8351-8355, **(2005)**.
22. S. Omae, T. Minemoto, M. Murozono et al, "Effects of Hydrogen Passivation for Spherical Silicon Solar Cells Fabricated by Dropping Method," *Japanese Journal of Applied Physics*, vol. 45, pp.1515-1519, **(2006)**.
23. Z. Liu, T. Nagai, A. Masuda et al, "Seeding Method with Silicon Powder for the Formation of Silicon Spheres in the Drop Method," *Journal of Applied Physics*, vol. 101, pp.0935051-0935052.
24. R. R. Schmit, "Highlights of Texas Instruments Spherical Solar Technology," *AIP Conference Proceedings*, vol. 303, pp.297-302, **(1994)**.
25. R. K. Ahrenkiel, D. Levi, J. Arch, "Recombination Lifetime Studies of Silicon Spheres", *Sol. En. Mat. Sol. Cells 41/42*, pp. 171-181, **(1996)**.
26. B. Esfandiarpour and S. Sivonthaman, "A Silicon Texturing Technique Based on Etching through a Liquid-Phase Deposited Oxide Mask", *Electrochemical and Solid-State Letters*, **13**, D97 **(2010)**.
27. R. R. Schmit, M. D. Hammerbacher et al, "A Review of Spherical Solar Technology," *Advances in Solar Energy*, vol.10, pp.347-379, **(1995)**.
28. M. Gharghi, and S. Sivonthaman, *Journal of Electronic Materials*, vol. 37, no.11, pp. 1657-1664, **(2008)**.
29. J. K. Arch, J. S. Reynolds, M. D. Hammerbacher et al, "Characterization of Silicon Spheres for Spherical Solar Cells," *24th IEEE Photovoltaic Specialists Conference*, pp.1364-1365, **(1994)**.

30. J. D. Levine, G. B. Hotchkiss and M. D. Hammerbacher, 22nd *IEEE Photovoltaic Specialists Conf.* 2, 1045 (1991).
31. L. T. Canham, *Appl. Phys. Lett.* 57, 1046 (1990).
32. O. Teschke, F. Alvarez, L. Tessler, and M. U. Kleinke, *Appl. Phys. Lett.* 63, 1927 (1993).
33. L. T. Canham, A. G. Cullis, C. Pickering, O. D. Dosser, T. I. Cox, and T. P. Lynch, *Nature* 368, 133 (1994).
34. K. Ito, S. Ohyama, Y. Uehara, and S. Ushioda, *Appl. Phys. Lett.* 67, 2536 (1995).
35. H. Yorikawa, S. Muramatsu, *J. Lumin.* 87, 423 (2000).
36. S. Shih, K. H. Jung, R.-Z. Qian, and D. L. Kwong, *Appl. Phys. Lett.* 62, 467 (1993).
37. A. G. Cullis and L. T. Canham, *Nature* 353, 335 (1991).
38. O. Bisi, S. Ossicini, and L. Pavesi, *Surf. Sci. Rep.* 38, 1 (2000).
39. J. Jakubowicz, *Superlattices Microstruct.* 41, 205(2007).
40. Y. V. Gorelkinskii, K. A. Abdullin, G. K. Kalykova, S. M. Kikarin, and B. N. Mukashev, *Mater. sci. eng. B* 147, 258 (2008).
41. V. Lysenko, V. Onyskevych, O. Marty, V. A. Skryshevsky, Y. Chevolut, and C. Bru-Chevallier, *Appl. Phys. Lett.* 92, 251910 (2008).
42. S. G. Lee, Y. Koh, S. Jang, J. Kim, H. G. Woo, S. Kim, and H. Sohn, *J. Nanosci. Nanotechnol.* 5, 3266 (2010).
43. S. Mor, V. Torres-Costa, R. J. Martín-Palma, and I. Abdulhalim, *Appl. Phys. Lett.* 97, 113106 (2010).
44. R. R. Bilyalov, R. Lüdemann, W. Wettling, L. Stalmans, J. Poortmans, J. Nijs, L. Schirone, G. Sotgiu, S. Strehlke and C. Lévy-Clément, *Sol. Energy Mater. Sol. Cells* 60, 391 (2000).
45. S. Lee and E. Lee, *J. Nanosci. Nanotechnol.* 7, 3713 (2007).
46. G.P. Wei, Y.M. Zheng, Z.J. Huang, Y. Li, J. Feng and Y.W. Mo., *Sol. Energy Mater. Sol. Cells* 35, 319 (1994).
47. L. L. Ma, Y. C. Zhou, N. Jiang, X. Lu, J. Shao, W. Lu, J. Ge, X. M. Ding, and X. Y. Hou, *Appl. Phys. Lett.* 88, 171907 (2006).
48. J. H. Selj, A. Thøgersen, S. E. Foss, and E. S. Marstein, *J. Appl. Phys.* 107, 074904 (2010).
49. S. Koynov, M. S. Brandt, and M. Stutzmann, *Appl. Phys. Lett.* 88, 203107 (2006).
50. H. C. Yuan, V. E. Yost, M. R. Page, P. Stradins, D. L. Meier, and H. M. Branz, *Appl. Phys. Lett.* 95, 123501 (2009).

51. H. M. Branz, V. E. Yost, S. Ward, K. M. Jones, B. To, and P. Stradins, *Appl. Phys. Lett.* **94**, 231121 (2009).
52. C. Wu, C. H. Crouch, L. Zhao, J. E. Carey, R. Younkin, J. A. Levinson, E. Mazur, R. M. Farrell, P. Gothoskar, and A. Karger, *Appl. Phys. Lett.* **78**, 1850 (2001).
53. K. Tsujino and M. Matsumura, *Adv. Mater. (Weinheim-Ger.)* **17**, 1045 (2005).
54. R.L. Smith, and S.D. Collins, *J. Appl. Phys.* **71**, R1 (1992).
55. V. Lehmann, and U. Gösele, *Appl. Phys. Lett.* **58**, 856 (1991).
56. M.I.J. Beale, J.D. Benjamin, M.J. Uren, N.G. Chew, and A.G. Cullis, *J. Crystal Growth* **73**, 622 (1985).
57. C. Pickering, M.I.J. Beale, D.J. Robbins, P.J. Pearson, and R. Greef, *J. Phys. C* **17**, 6535 (1984).
58. M.J. Eddowes, *J. Electroanal. Chem.* **280**, 297 (1990).
59. V. Lehmann, and H. Foll, *J. Electrochem. Soc.* **137**, 653 (1990).
60. A.G. Cullis, L.T. Canham, and P.D.J. Calcott, *J. Appl. Phys.* **82**, 909 (1997).
61. R.L. Smith, S.F. Chuang, and S.D. Collins, *J. Electron. Mater.* **138**, 533 (1988).
62. A. Nishida, K. Nakagawa, H. Kakibayashi, and T. Shimada, *Jpn. J. Appl. Phys.* **31**, L1219 (1992).
63. S. Rönnebeck, J. Carstensen, S. Ottow, and H. Föll, *Electrochem. Solid State Lett.* **2**, 126 (1999).
64. R. W. Fathauer, T. George, A. Ksendzov, and R. P. Vasquez, *Appl. Phys. Lett.* **60**, 995 (1992).
65. M. Schoisswohl, J. L. Cantin, H. J. von Bardeleben, and G. Amato, *Appl. Phys. Lett.* **66**, 3660 (1995).
66. A. J. Steckl, J. Xu, H. C. Mogul, and S. M. Prokes, *J. Electrochem. Soc.* **142**, L69 (1995).
67. S. Liu, C. Palsule, S. Yi, and S. Gangopadhyay, *Phys. Rev.* **49**, 10318 (1994).
68. M. T. Kelly, J. K. M. Chun, and A. B. Bocarsly, *Appl. Phys. Lett.* **64**, 1693 (1994).
69. M. J. Winton, S. D. Russell, J. A. Wolk, and R. Gronsky, *Appl. Phys. Lett.* **69**, 4026 (1996).
70. S. Shih, K.H. Jung, T.Y. Hsieh, J. Sarathy, J.C. Campbell, and D.L. Kwong, *Appl. Phys. Lett.* **60**, 1863 (1992).
71. Y. Kanemitsu, H. Uto, Y. Masumoto, T. Matsumoto, T. Futagi, and H. Mimura, *Phys. Rev. B* **48**, 2827 (1993).

72. P.M. Fauchet, J. von Behren, *Phys. Stat. Sol. (b)* 204, R7 (1997).
73. U. Gösele and V. Lehmann, *Mater. Chem. Phys.* 40, 253 (1995).
74. O. Nichiporuk, A. Kaminski, M. Lemiti, A. Fave, S. Litvinenko, V. Skryshevsky, *Thin Solid Films*, 511–512, 248 (2006).
75. K. Prabakar, S. Minkyu, S. Inyoung and K. Heeje, *J. Phys. D: Appl. Phys.* 43, 012002 (2010).
76. C. L. Choi and A. P. Alivisatos, *Annu. Rev. Phys. Chem.* 61, 369 (2010).
77. A. V. Malko, A. A. Mikhailovsky, M. A. Petruska, J. A. Hollingsworth, H. Htoon, M. G. Bawendi, and V. I. Klimov, *Appl. Phys. Lett.* 81, 1303 (2002).
78. J. S. Steckel, S. Coe-Sullivan, V. Bulovic, and M. Bawendi, *Adv. Mater. (Weinheim, Ger.)* 15, 1862 (2003).
79. S. A. McDonald, P. W. Cyr, L. Levina, and E. H. Sargent, *Appl. Phys. Lett.* 85, 2089 (2004).
80. W. U. Huynh, J. J. Dittmer, and A. P. Alivisatos, *Science* 295, 2425 (2002).
81. Q. Shen, T. Sato, M. Hashimoto, C. C. Chen, and T. Toyoda, *Thin Solid Films* 499, 299 (2006).
82. P. R. Yu, K. Zhu, A. G. Norman, S. Ferrere, A. J. Frank, and A. J. Nozik, *J. Phys. Chem. B* 110, 25451 (2006).
83. Brus, L. E. *J. Phys. Chem.* 90, 2555 (1986).
84. S. Coe, W. K. Woo, M. Bawendi, and V. Bulovic, *Nature* 420, 800 (2002).
85. G. Konstantatos, C. Huang, L. Levina, Z. Lu, and E. H. Sargent, *Adv. Funct. Mater.* 15, 1865 (2005).
86. S. A. McDonald, G. Konstantatos, S. Zhang, P. W. Cyr, E. J. D. Klem, L. Levina, and E. H. Sargent, *Nature Mater.* 4, 138 (2005).
87. G. Konstantatos and E. H. Sargent, *Proc. of IEEE* 97, 1666 (2009).
88. Y. Chiba, A. Islam, Y. Watanabe, R. Komiya, N. Koide, and L. Y. Han, *Jpn. J. Appl. Phys.* 45, L638 (2006).
89. M. Grätzel, *J. Photochem. Photobiol. C* 4, 145 (2003).
90. O. Niitsoo, S. K. Sarkar, C. Pejoux, S. Rühle, D. Cahen, and G. Hodes, *J. Photochem. Photobiol. A* 181, 306 (2006).
91. A. Hagfeldt and M. Grätzel, *Chem. Rev.* 95, 49 (1995).
92. N. Arthur, *Annu. Rev. Phys. Chem.* 52, 193 (2001).

93. M. Gharghi, "Spherical Silicon for Photovoltaic Applications: Material, Modeling and Devices," *doctoral dissertation*, Waterloo, Ontario, Canada (2007).
94. J. D. Levine, "Design Criteria of the Spherical Solar Cell," *AIP Conference Proceedings*, vol. **268**, pp.47-51, (1992).
95. H. J. Moller, L. Long, M. Werner, and D. Yang, *Phys. Status Solidi A*, **171**, pp. 175–189 (1999).
96. D. Bouhafs, A. Moussi, A. Chikouche, and J. M. Ruiz, *Sol. Energy Mater. Sol. Cells* **52**, 79 (1998).
97. H. C. Yuan, V. E. Yost, M. R. Page, P. Stradins, D. L. Meier, and H. M. Branz, *Appl. Phys. Lett.* **95**, 123501 (2009).
98. H. M. Branz, V. E. Yost, S. Ward, K. M. Jones, B. To, and P. Stradins, *Appl. Phys. Lett.* **94**, 231121 (2009).
99. J.L. Maurice, A. Rivière, A. Alapini, and C. LévyClément, *Appl. Phys. Lett.* **66**, p. 1665 (1995).
100. H. Richter, Z.P. Wang and L. Ley. *Solid State Commun.* **39**, 625 (1981).
101. P. Mishra and K. P. Jain, *Phys. Rev. B* **64**, 073304 (2001).
102. M. A. Ferrara, M. G. Donato, L. Sirleto, G. Messina, S. Santangelo and I. Rendina, *J. Raman Spectrosc.* **39**, 199 (2008).
103. I.H. Campbell and M.P. Fauchet. *Solid State Commu.* **58**, 739 (1986).
104. Mariotto, F. Ziglio and F.L. Freire Jr., *J. Non-Cryst. Solids* **192-193**, 253 (1995).
105. R. B. Stephens and G. D. Cody, *Thin Solid Films* **45**, 19 (1977).
106. H. Seidel, L. Csepregi, A. Heuberger, and H. Baumgärtel, *J. Electrochem. Soc.*, **141**, 965 (1994).
107. B. Vallejo, M. González- Díaz, R. Guerrero-Lemus, D. Borchert, and C. Hernández-Rodríguez, *Sol. Energy Mater. Sol. Cells*, **91**, 1943 (2007).
108. K. Sato, M. Shikida, T. Yamashiro, M. Tsunekawa, and S. Ito, *Sens. Actuators A*, **73**, 122 (1999).
109. M. Moreno, D. Daineka, and P. R. i Cabarrocas, *Sol. Energy Mater. Sol. Cells*, **94**, 733 (2010).
110. K. Kim, S.K. Dhungel, S. Jung, D. Mangalaraj, and J. Yi, *Sol. Energy Mater. Sol. Cells*, **92**, 960 (2008).

111. J. Zhao, A. Wang, P. Campbell, and M. A. Green, *IEEE Trans. Electron Devices*, **46**, 1978 (1999).
112. N. Marrero, R. Guerrero-Lemus, B. González-Díaz, and D. Borchert, *Thin Solid Films*, **517**, 2648 (2009).
113. K. Awazu, H. Kawazoe, and K. Seki, *J. Non-Cryst. Solids*, **151**, 102 (1992).
114. T. Homma, T. Katoh, Y. Yamada, and Y. Murao, *J. Electrochem. Soc.*, **140**, 2410 (1993).
115. C. F. Yeh, S. S. Lin, T. Z. Yang, C. L. Chen, and T. Y. Hong, *IEEE Trans. Electron Devices ED-41*, 173 (1994).
116. C. H. Chen, C. C. Hong, and J. G. Hwu, *J. Electrochem. Soc.*, **149** (6), G362-G366 (2002).
117. M. J. Jeng and J. G. Hwu, *J. Vac. Sci. Technol. A*, **15**, 369 (1997).
118. H. J. Lewerenz, *Electrochim. Acta*, **37**, 847 (1992).
119. M.J. Eddowes, *J. Electroanal. Chem.*, **280**, 297 (1990).
120. V. Lehmann and H. Foll, *J. Electrochem. Soc.*, **137**, 653 (1990).